

## The stability of dikes subjects to soil-vegetation-atmosphere interaction

Jamalinia, E.

**DOI**

[10.4233/uuid:30370243-2992-4f91-8d0f-19f60ae43e49](https://doi.org/10.4233/uuid:30370243-2992-4f91-8d0f-19f60ae43e49)

**Publication date**

2021

**Document Version**

Final published version

**Citation (APA)**

Jamalinia, E. (2021). *The stability of dikes subjects to soil-vegetation-atmosphere interaction*. [Dissertation (TU Delft), Delft University of Technology]. <https://doi.org/10.4233/uuid:30370243-2992-4f91-8d0f-19f60ae43e49>

**Important note**

To cite this publication, please use the final published version (if applicable).  
Please check the document version above.

**Copyright**

Other than for strictly personal use, it is not permitted to download, forward or distribute the text or part of it, without the consent of the author(s) and/or copyright holder(s), unless the work is under an open content license such as Creative Commons.

**Takedown policy**

Please contact us and provide details if you believe this document breaches copyrights.  
We will remove access to the work immediately and investigate your claim.

**THE STABILITY OF DIKES SUBJECT TO  
SOIL-VEGETATION-ATMOSPHERE INTERACTION**



# **THE STABILITY OF DIKES SUBJECT TO SOIL-VEGETATION-ATMOSPHERE INTERACTION**

## **Dissertation**

for the purpose of obtaining the degree of doctor  
at Delft University of Technology,  
by the authority of the Rector Magnificus prof. dr. ir. T.H.J.J. van der Hagen,  
chair of the Board for Doctorates,  
to be defended publicly on Wednesday 3 November 2021 at 17:30 o'clock

by

**Elahe JAMALINIA**

Master of Science in Civil-Environmental Engineering,  
University of Tehran, Tehran, Iran,  
born in Shiraz, Iran.

The dissertation has been approved by the promoters.

promotor: Dr. P.J. Vardon

promotor: Prof. dr. S.C. Steele-Dunne

Composition of the doctoral committee:

Rector Magnificus

Dr. P.J. Vardon

Prof. dr. S.C. Steele-Dunne

Chairperson

Delft University of Technology

Delft University of Technology

*Independent members:*

Dr. K. Tsiamposi

Ir. H. van Hemert

Prof. dr. M.A. Hicks

Prof. dr. S.N. Jonkman

Dr. J.P. Aguilar Lopez

Imperial College London

Rijkswaterstaat, STOWA

Delft University of Technology

Delft University of Technology

Delft University of Technology



*Keywords:* Soil-Vegetation-Atmosphere interaction, Slope stability, Numerical analysis, dike monitoring

*Printed by:* Ipskamp Printing

*Cover design:* Elham Tavakol @elhamtavakol.art

Copyright © 2021 by E. Jamalnia

ISBN 978-94-6366-464-6

An electronic version of this dissertation is available at

<http://repository.tudelft.nl/>.

*To my parents*

Zohreh & Ali



# CONTENTS

<b>Summary</b>	<b>xi</b>
<b>Samenvatting</b>	<b>xiii</b>
<b>List of Symbols</b>	<b>xv</b>
<b>1 Introduction</b>	<b>1</b>
1.1 Background and motivation . . . . .	2
1.2 Research Objectives . . . . .	5
1.3 The Reliable Dykes project . . . . .	6
1.4 Overview of the thesis . . . . .	7
References . . . . .	9
<b>2 Soil-Vegetation-Atmosphere Interaction in regional dikes</b>	<b>13</b>
2.1 Introduction . . . . .	14
2.2 Method . . . . .	14
2.2.1 Crop model . . . . .	16
2.2.2 Water balance equation . . . . .	16
2.2.3 Leaf growth equation . . . . .	17
2.2.4 Geotechnical Model . . . . .	17
2.2.5 Hydro-mechanical analysis . . . . .	17
2.2.6 Safety analysis . . . . .	18
2.2.7 Coupling crop and geotechnical models . . . . .	18
2.2.8 Case study . . . . .	19
2.2.9 Geometry . . . . .	19
2.2.10 Meteorological data . . . . .	19
2.2.11 Root zone: crop model . . . . .	19
2.2.12 Geotechnical model . . . . .	21
2.3 Results and Discussion . . . . .	21
2.3.1 Time series of the SVA interaction variables . . . . .	21
2.3.2 $WC_{rz}$ influence on FoS . . . . .	24
2.3.3 Correlation among selected SVA variables . . . . .	25
2.3.4 LAI effect . . . . .	27
2.4 The possibility of using vegetation as a safety indicator . . . . .	28
2.5 Conclusion . . . . .	29
References . . . . .	30



<b>3</b>	<b>The impact of evaporation induced cracks and precipitation on temporal slope stability</b>	<b>33</b>
3.1	Introduction	34
3.2	Method	35
3.2.1	Crop Model	35
3.2.2	Geotechnical model	40
3.2.3	Case study	40
3.3	Results and Discussion	42
3.4	Using vegetation as an indicator for dike health	45
3.5	Conclusion	49
	References	50
<b>4</b>	<b>A data-driven surrogate approach for the temporal stability forecasting of vegetation covered dikes</b>	<b>53</b>
4.1	Introduction	54
4.2	Method	56
4.2.1	Integrated Crop-Geotechnical Model	57
4.2.2	Machine Learning Method	57
4.2.3	Case Study	60
4.3	Results and Discussion	62
4.3.1	Integrated Crop-Geotechnical Model Simulations	62
4.3.2	Correlation between Potential Features and the Factor of Safety	64
4.3.3	RF Regression	67
4.4	Conclusion	76
	References	77
<b>5</b>	<b>Potential value of remote sensing for dike inspection</b>	<b>83</b>
5.1	Introduction	84
5.2	Vegetation monitoring	85
5.3	Deformation monitoring	89
5.3.1	Deformation monitoring using InSAR	89
5.3.2	InSAR time series	92
5.4	Case study	93
5.4.1	Vegetation condition	94
5.4.2	Deformation data from InSAR processing	98
5.5	Conclusion	99
	References	101
<b>6</b>	<b>Conclusion and Discussion</b>	<b>105</b>
6.1	Conclusion	106
6.2	Contributions	108
6.3	Recommendations For future studies	109
	References	111

---

<b>Acknowledgements</b>	<b>113</b>
<b>Curriculum Vitae</b>	<b>115</b>
<b>List of Publications</b>	<b>117</b>



# SUMMARY

Large areas of the Netherlands are below the sea level, and a network of primary and secondary (regional) dikes protect these areas from inundation. Regular assessments and monitoring are implemented with the intention of ensuring the safety of the protected areas. However these assessments usually ignore that these dikes are subject to various climatic driving forces. This thesis demonstrates the effect of Soil-Vegetation-Atmosphere (SVA) interaction via the use of an idealised example regional dike, and then introduces up-to-date techniques that can lead to automated early warning systems and almost real-time monitoring of the regional dikes.

The presence of vegetation cover on dikes influences the water balance in the root zone and consequently the dike body. The stability is then affected by variations of pore water pressure in soil body. Most geotechnical models simply ignore the effect of vegetation on the soil surface; however, this research offers an integrated numerical approach to simulate the dynamic effect of both vegetation and climate driving forces on the (in)stability of the example dike. The vegetation growth and the real climate data in the introduced integrated crop-geotechnical model are considered in order to enhance the safety analysis and close the gap between simulations and reality. As these numerical simulations are computationally expensive and rely on many input parameters, a data driven approach is introduced to avoid repeating numerical analysis for a dike. The approach is shown to be able to estimate the safety factor using easily observable parameters. Using supervised Machine Learning, showed that measurable parameters that can be observed remotely (including precipitation history, temperature, vegetation indices and displacement) can be used to estimate the safety condition of dikes in real-time and short-term prediction. From the investigated parameters, it is found that displacement has the highest feature importance to estimate safety.

The numerical studies showed that vegetation and stability are responsive to the climate driving forces, e.g. precipitation, radiation, temperature, wind speed. The interaction between the vegetation, climate and stability is coupled and complex. The vegetation and the state of the vegetation will affect the water balance, flow patterns, pore water pressure distribution of the dike and then the factor of safety. The climatic conditions will impact both the vegetation and dike stability on one hand, and on the other hand vegetation state will affect the water balance and in turn it is affected by the amount of water in the root zone. Cracks in the dike, caused by drought conditions, are both affected by the vegetation and also affect the vegetation growth and hydraulic behaviour. These cracks, which mostly affect the root zone, alter the water balance by increasing the evaporation and preferential flow within the dike that leads to higher pore water pressures in the dike body. This shows the importance of vegetation monitoring over the regional dikes. Currently, in the Netherlands, dike observers do visual inspections twice per year for the regional dikes by walking along dikes and undertaking a descriptive report. This research tries to improve this conventional method of vegetation monitoring by use of

remote sensing monitoring tools that can observe a larger area and can be significantly less expensive. Measurable indexes of vegetation can be measured by air-borne (e.g. drones) or space-borne (e.g. satellites) instruments, instead of classifying the vegetation condition qualitatively. In addition, it is suggested monitoring displacement regularly using InSAR method will provide high precision (mm level) data that together with the vegetation indices aids the estimation of the safety condition.

An integrated approach of real-time monitoring, using easily observable data and data driven models, can assist dike managers to investigate the effect of climate driving forces and vegetation on the temporal stability. This will improve the current visual inspection of regional dikes and provide early warning of dikes which require further attention.

# SAMENVATTING

Een groot oppervlak van Nederland ligt onder het zeeniveau en wordt beschermd tegen overstroming door een netwerk van primaire en regionale dijken. Regelmatige beoordelingen en monitoring worden uitgevoerd met de bedoeling de veiligheid van de beschermde gebieden te waarborgen. Deze beoordelingen gaan echter meestal voorbij aan het feit dat deze taluds onderhevig zijn aan verschillende klimatologische factoren. In dit proefschrift is het effect van bodemvegetatie op een voorbeeld van een regionale dijk uitgewerkt en zijn er moderne technieken toegelicht voor geautomatiseerde vroege waarschuwingen en het real-time monitoren van de regionale dijken.

De aanwezigheid van vegetatiebedekking op dijken beïnvloedt de waterbalans in de wortelzone en de dijk kern. De dijk stabiliteit wordt daarnaast ook beïnvloed door variaties van poriewaterdrukken in de grond. De meeste geotechnische modellen negeren simpelweg het effect van vegetatie op het dijkoppervlak. In dit onderzoek is echter een numerieke benadering toegelicht om het dynamische effect van zowel de vegetatie op het grondoppervlak als de invloed van het klimaat op de dijk stabiliteit van de voorbeelddijk te analyseren. Het groeien van de vegetatie en de klimaatdata in het geïntroduceerde geotechnische model zijn beschouwd om de veiligheidsanalyse te verbeteren en het gat tussen een simulatie en de realiteit te dichten. Doordat deze numerieke simulaties rekenkundig duur zijn en afhankelijk zijn van veel invoerparameters, is een benadering op basis van data geïntroduceerd om herhalende numerieke analyses van een dijk te vermijden. De geïntroduceerde rekenbenadering blijkt gemakkelijk de veiligheidsfactoren van dijken op basis van makkelijk observeerbare parameters te kunnen bepalen. Uit het gebruik van Machine Learning blijkt dat de meetparameters die op afstand afgelezen kunnen worden (waaronder neerslaghistorie, temperatuur, vegetatie indexen en de verplaatsing) gebruikt kunnen worden om de veiligheidssituatie van dijken in zowel real-time als op korte termijn te bepalen. Uit de onderzochte parameters blijkt dat de verplaatsing de hoogte invloed/prioriteit heeft om de veiligheid te bepalen.

Het numerieke onderzoek laat zien dat de vegetatie en stabiliteit verantwoordelijk zijn voor de klimaat gestuurde krachten, zoals: neerslag, temperatuur en straling. De interactie tussen de vegetatie, het klimaat en de stabiliteit is complex en aan elkaar gekoppeld. De vegetatie en de staat hiervan zullen invloed hebben op de hydraulische prestatie van de dijk en de veiligheidsfactor hiervan. De klimaatcondities zullen aan de ene kant invloed hebben op de vegetatie én de dijk stabiliteit en aan de andere kant zal de vegetatiestaat invloed hebben op de waterbalans. Dit is echter afhankelijk van de hoeveelheid water in de wortelzone. Scheuren in de dijken door droge periodes zijn ook beïnvloed door de vegetatie en de droogte heeft zelf ook invloed op de groei van de vegetatie en het hydraulische gedrag. Deze scheuren, die vooral de wortelzone aantasten, veranderen de waterhuishouding door de verdamping en preferentiële stroming binnen de dijk te vergroten, wat leidt tot hogere poriewaterdrukken in het dijklichaam. Dit laat zien hoe belangrijk vegetatiemonitoring is bij regionale dijken. Op dit moment worden de regionale

twee keer per jaar visueel geïnspecteerd door de dijkbeheerders door eroverheen te lopen en te rapporteren wat opvalt. Dit onderzoek probeert om dit proces te verbeteren door de monitoring van vegetatie op basis van meetgereedschappen op afstand te gebruiken die een groter oppervlak waarnemen en tegelijkertijd aanzienlijk goedkoper zijn om uit te voeren. Meetbare indexen van de vegetatie kunnen worden gemeten door lucht- of ruimteapparatuur zoals drones en/of satellieten in plaats van het kwalitatief classificeren van de staat van de vegetatie. Daar aan toegevoegd wordt aanbevolen om de verplaatsing regelmatig te monitoren aan de hand van de InSAR-methode. De methode levert accurate data (tot op de mm) die samen met de vegetatie-indexen de veiligheidsverwachting kunnen bepalen.

Het real-time monitoren aan de hand van gemakkelijk observeerbare data en data gestuurde modellen kan de dijkbeheerder assisteren om het effect van het klimaat en de vegetatie op de dijkstabiliteit te onderzoeken. Dit verbetert de huidige visuele dijkinspectie van de regionale dijken en dit zorgt voor vroeger waarschuwingen bij dijken die meer aandacht nodig hebben.

# LIST OF SYMBOLS

## ACRONYMS

1D	1 Dimensional
2D	2 Dimensional
DT	Decision Tree
EO	Earth observation
ESA	European Space Agency
FEM	Finite Element Method
FoS	Factor of Safety
GNSS	Global Navigation Satellite System
GWL	Ground Water Level
HP	Hyper-Parameter
InSAR	Interferometry Synthetic Aperture Radar
KNMI	Royal Netherlands Meteorological Institute
LiDAR	Light Detection and Ranging
LINGRA	LINTUL GRAssland
LINTUL	Light INTerception and Utilization simulator
LOS	Line-Of-Sight
ML	Machine Learning
MSE	Mean Squared Error
NAP	Normaal Amsterdams Peil (reference level)
NSO	Netherlands Space Office
PSI	Persistent Scatterer Interferometry
pwp	pore water pressure
RF	Random Forest
RMSD	Root Mean Square Difference
RMSE	Root Mean Square Error
RS	Remote Sensing
SAR	Synthetic Aperture Radar
SVA	Soil-Vegetation-Atmosphere
SWRC	Soil Water Retention Curve
VI <sub>s</sub>	Vegetation Indices

## LATIN SYMBOLS

$ accel.[LAI] $	magnitude of difference in $dif[LAI]$ between two timesteps
$A_{crack}$	crack area in the root zone
$A_{matrix}$	surface area of the soil



$c'$	effective cohesion
$c'_{input/reduced}$	input/reduced effective cohesion
$c'_{intact}$	intact effective cohesion
$c'_{min}$	minimum effective cohesion
$CLAI$	Remaining $LAI$ after cutting
$diff[LAI]$	difference in $LAI$ between two timesteps
$D_{crack}$	drainage calculated from LINGRA from crack
$D_L$	drainage calculated from LINGRA
$D_{matrix}$	drainage calculated from LINGRA from soil
$D_P$	drainage calculated from PLAXIS
$DRATE$	maximum drainage
$e$	void ratio
$e_0$	void ratio at $\mu = 0$
$e_{init}$	initial void ratio
$E$	evaporation
$E'$	effective Young's modulus
$ET$	evapotranspiration
$f(lv)$	fraction of dry vegetation matter to leaves
$FoS$	Factor of Safety
$\underline{g}$	vector of gravitational acceleration
$h$	hydraulic suction in soil
$I_{p,crack}$	precipitation amount infiltrates into the crack matrix
$I_{p,matrix}$	precipitation amount infiltrates into the soil matrix
$In$	leaf interception
$LAI$	Leaf Area Index
$LAI_d$	Leaf Area Index death
$LAICR$	Critical Leaf Area Index
$k_{rel}$	relative hydraulic conductivity
$\underline{k_{sat}}$	saturated hydraulic conductivity
$\underline{K}$	number of groups for k-fold clustering
$l$	target value in RF regressor
$L$	length of the cross-section
$m,n$	fitting parameters for soil water retention curve
$n$	tree number in RF regressor
$N$	number of trees in RF regressor
$NDVI$	Normalised Difference Vegetation Index
$NIR$	near-infrared light
$Q_{net}$	boundary net flux
$P$	precipitation
$\underline{q}$	vector of specific discharge
$r_s$	dimensionless geometry factor
$R$	correlation coefficient
$Rain-1d$	rainfall intensity on the same day that FoS is calculated
$Rain.cu-65$	cumulative rainfall during the last 65 days

<i>RED</i>	red (visible) light
<i>Rn</i>	runoff
<i>ROOTDM</i>	root zone depth
<i>Sat</i>	Saturation
<i>SLA</i>	Specific Leaf Area
<i>SM</i>	Soil Moisture
<i>SM<sub>rz</sub></i>	average Soil Moisture in the root zone
<i>Sr</i>	degree of soil saturation
<i>Sr<sub>fc</sub></i>	degree of soil saturation at field capacity
<i>Sr<sub>intact</sub></i>	degree of soil saturation at intact conditions
<i>Sr<sub>matrix</sub></i>	degree of soil saturation of the matrix
<i>TMP</i>	Temperature
$ U $	magnitude of displacement
<i>V<sub>crack</sub></i>	crack volume fraction in the root zone
<i>V<sub>matrix</sub></i>	matrix volume
<i>V<sub>pores</sub></i>	pores volume fraction in the soil matrix
<i>V<sub>solid</sub></i>	solid volume fraction
<i>V<sub>shrinkage</sub></i>	shrinkage volume fraction in the root zone
<i>V<sub>subsidence</sub></i>	subsidence volume fraction in the root zone
<i>V<sub>water</sub></i>	water volume fraction in the soil matrix
<i>W</i>	growth of crop dry matter
<i>WA</i>	Water Amount stored in the root zone
<i>WC<sub>body</sub></i>	average water content in the dike body
<i>WC<sub>rz</sub></i>	Water Content in the root zone
<i>x</i>	input vector of features in RF regressor

## GREEK SYMBOLS

$\alpha$	fitting parameter related to the air entry value
$\beta_K$	fitting parameters for equation 3.5
$\gamma_K$	fitting parameters for equation 3.5
$\gamma_{sat}$	saturated unit weight
$\Delta j$	index difference
$\theta$	water content
$\theta_{cr}$	critical water content
$\theta_{fc}$	water content at field capacity
$\theta_r$	residual water content
$\theta_{rz}$	water content in the root zone
$\theta_{sat}$	water content at saturation
$\theta_{wp}$	water content at wilting point
$\mu$	moisture ratio
$\nu'$	effective Poisson's ratio
$\rho_w$	water density
$\phi'$	effective friction angle
$\phi'_{input/reduced}$	input/reduced friction angle for non-cracked soil
$\phi'_{intact}$	intact friction angle

$\phi'_{min}$   
 $\psi$ minimum friction angle  
dilation angle

# 1

## INTRODUCTION

## 1.1. BACKGROUND AND MOTIVATION

**D**IKES are predominantly earth structures, which create a noticeable part of existing flood defence systems and their primary objective is to provide protection against flood events (CIRIA, 2013). Failures of dikes often lead to significant losses. Natural or human-induced driving mechanisms can cause dike failures due to either hydraulic or geotechnical problems. Failure of dikes is often a time-dependent process that can initiate from the deterioration or damage of dike components which ultimately results in a failure mechanism forming (Cundill, 2016). A dike failure can be classified as either hydraulic failure or structural failure. The former occurs when water reaches into the dike system, e.g. by overflow or over-topping, while a structural failure occurs causing a breach in a dike system. The two kinds of failure can induce each other (CIRIA, 2013). In Table 1.1, some of the common failure mechanisms are shown including typical performance parameters which impact that mechanism and visual indicators that the mechanism is occurring or at risk of occurring. Dike inspectors use these visual indicators to detect vulnerable sections of dike and to assess the condition of the slope. Overflow or over-topping occurs when water enters the area protected by the dike, which may cause a change in the crest height and cover quality over a dike. Rotational or horizontal sliding results from the poor performance of the geometry, for instance cracking and slope movements are indicators of shallow or deep soil movements. Internal erosion may be caused by piping or seepage within the dike body, when fine soils are washed out and presence of altered vegetation on the dike can be a sign of areas prone to failure.

The soil surface is the most dynamic part of a dike due to the interaction it has with both weather conditions and vegetation in vegetation covered dikes. Vegetation interacts with the atmosphere and the soil, and also reacts to those conditions. For example, the current state of the vegetation determines how much water can evaporate from a dike surface; however, the amount of precipitation and water in the soil strongly influences the rate of growth of the vegetation. So-called Soil-Vegetation-Atmosphere (SVA) interaction on a dike surface, leads to water balance variation within the top soil through evapotranspiration and infiltration, and further impacts the conditions of the whole dike (Vardon, 2015; Pedone *et al.*, 2016; Tsiampousi *et al.*, 2016). SVA interaction is mobilised by heat and water transfer between the soil surface and the atmosphere in the vicinity of the soil surface. Some of the involved mechanisms in these heat and water transfer processes are: radiation, conduction and advection of heat and infiltration, evaporation or evapotranspiration and root-water-uptake (Hemmati *et al.*, 2012). SVA interaction refers to the process in which atmospheric conditions influence both the vegetation and soil states. Water content variations within the root zone influence vegetation growth and soil subsidence through shrinkage/swelling behaviour of the soil. This can directly threaten dike structures by reducing lateral support, making the systems more vulnerable to instabilities. In addition, a water deficit on the surface layer of dikes is a key cause of crack development, which allow water infiltration during subsequent rainfall and can lead to the development of a failure mechanism. The soil surface and vegetation are the lower boundary of the atmosphere, and they are therefore actively affected by the climate system. In particular, changes in albedo and precipitation (atmospheric parameters) generate important changes in the soil and vegetation. Vegetation has impacts on soil-atmosphere water fluxes regulating evapotranspiration.

Evaporation from bare soil occurs from the top surface, whereas plant roots can transport water from deeper in the soil and therefore can affect the water flux between soil and atmosphere. It is therefore logical that the water availability for the vegetation increases with root length. It was been observed, that larger plants have generally longer roots, and they grow more as they can reach more water (Baudena *et al.*, 2013). The root zone thickness ranges from centimetres to several decimetres, depending on the characteristics of the vegetation (TAW (Technical Advisory Committee for Flood Defence), 1996). The tensile strength of vegetation roots also influences slope stability. This is affected by root type, geometry and spatial variation of the roots, which reinforce soil in the root zone (Greenwood *et al.*, 2007). Root length and density impact on the soil shear strength of the root zone (Osman & Barakbah, 2006). For instance, grasses with their dense network of shallow roots protects dikes from surface erosion (Stokes *et al.*, 2008).

The characterisation of SVA can enable a better understanding of the safety of dikes (Brooks *et al.*, 1995). Prediction or early detection of the occurrence of low levels of safety can assist dike managers in prioritising their inspection and upgrade/repair efforts. Items checked during a dike inspection include cracking, seepage, settlements, saturation and vegetation state. The investigation of vegetation patterns and utilising stressed grass as indicators of subsurface condition of the levee are methods which have been used successfully in Mississippi (Hasan *et al.*, 2013). Vahedifard *et al.* (2017) investigated the influence of rainfall on the shallow instability of several earthen levees (dikes). The results showed that 9 out of 23 shallow failures happened in the peak rainfall month, 7 shallow slides occurred one month after the peak rainfall month, and the remaining six slides occurred two months after the peak rainfall month. Increased rainfall intensity can surge the pore water pressure in soil causing significant reductions in the soil suction and soil strength (e.g. Wang *et al.*, 2018). On the other hand, drought conditions may lead to instability in dikes by weakening processes such as soil-strength reduction, soil desiccation cracking, soil subsidence and surface erosion, and microbial oxidation of organic soil (e.g. peat) (Robinson & Vahedifard, 2016). For example, the Wilnis dike in the Netherlands failed in summer 2003 due to dry condition that year, the warmest and driest summer in the 50 years up to that time, which caused the translation of about 60 m of dike almost 10 m (van Baars, 2005).

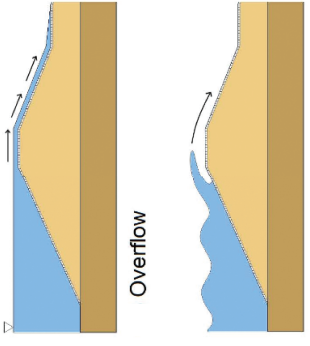
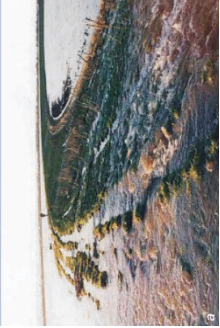
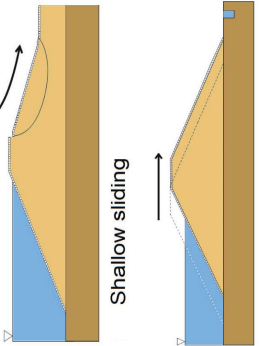

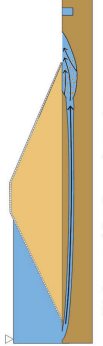

Failure Mode	Performance Parameters	Visual Indicators	Example
 <p>Overflow</p> <p>Overtopping</p>	<p>Crest height, Outer slope grass quality, Outer slope angle</p>	<p>Rutting of crest, Crest height below SoP, Vegetation on outer slope</p>	
 <p>Shallow sliding</p> <p>Transitional sliding</p>	<p>Crack width, Slip distance, Slope angle, Slip width, Slip height, Slip circle radius</p>	<p>Cracking, Slope movement, Animal burrowing, 3rd party damage to slope or toe</p>	
 <p>Piping and backward erosion</p>	<p>Embankment width, Soil coefficients, Seepage length, Water level difference, Creep ratio</p>	<p>Signs of seepage, Presence of washed out fines, Animal burrowing, Altered vegetation on bank</p>	

Table 1.1: Main failure mechanisms of dikes and their visual indicators (Cundill, 2016; Dunbar *et al.*, 2017; CIRIA, 2013).

## 1.2. RESEARCH OBJECTIVES

More than 50% of the Netherlands is below the river or sea level. To prevent these areas from flooding, dikes are built along river banks and the coast. Inland waterways are protected from flooding the land by so-called secondary dikes, of which in the Netherlands there are about 14 000 km. Though dike failures are seldom, their consequences can be substantial. For example, the peat dike in Wilnis failed in August 2003 when a weight reduction of the dike, due to drought, led to a horizontal shear failure. Around 300 houses were flooded as a result, and material damages amounted to around €10 million (Cundill, 2016). In the Netherlands, inspection and maintenance are essential for maintaining stringent flood protection standards and to ensure that flood defences meet their safety standards. Stability analysis of the dikes and regular monitoring are parts of the dikes authorities' regime to ensure safety. However, presently SVA interaction is not included in stability analysis and the vegetation state is only qualitatively assessed. Regarding these aspects, four research questions are defined and addressed in this thesis:

- **Research question 1: How does the climate and vegetation condition affect the temporal (in)stability of a regional dike?**

The soil surface is the interface that is influenced by external actions; in other words, the top surface of the soil receives the impact of weather conditions; characteristics of the soil surface often control functions deeper in the soil. Although clay itself is regarded as an appropriate material for the dike cover, it is usually reinforced by a grass cover. The grass roots play an important role in keeping the particles and small aggregates in the soil together. In the Netherlands, a top layer consisting of clay with a grass cover is a simple and in many situations effective construction, especially for river dikes (TAW (Technical Advisory Committee for Flood Defence), 1996). The vegetation reflects various characteristics of the soil on which it grows, e.g. the stressed vegetation is a sign of lack of water in the root zone, or growth of spontaneous vegetation can be a sign of outflow over a dike (CIRIA, 2013). Commonly-used geotechnical models (e.g. Plaxis BV, 2018) do not simulate the dynamic effects of vegetation on water fluxes (evaporation and influx) and therefore do not consider the influence that vegetation may have on soil-atmosphere interactions and slope stability. Crop models, however, have been used to simulate the interaction of vegetation and the upper soil layers (e.g. LINGRA (Bouman *et al.*, 1996)). In order to consider the dynamic effect of weather and vegetation condition, a crop model is integrated with a geotechnical model and numerical analysis for an example dike implemented to study the temporal dike stability.

- **Research question 2: What is the effect of soil shrinkage behaviour on the temporal (in)stability of a dike?**

Soil shrinkage due to extreme dry conditions may result in the occurrence of shrinkage cracks, which can provide favorable conditions for rain infiltration and reduce the strength of the dike, and consequently cause failure. Most of the current hydro-mechanical models for slope stability analysis are based on a continuum modeling approach, as explicitly simulating the cracking process and preferential flow is difficult at a structure scale. To address this question, the integrated crop-geotechnical model is adopted to tackle this limitation and by considering shrinkage behaviour



in the safety calculation that allows temporal analysis to calculate the impact of vegetation and climatic driving forces on the crack development and its effect on stability.

- **Research question 3: Can data-driven models emulate the expensive numerical simulations to estimate real-time or short-term prediction of (in)stability?**

Safety analysis of slopes can be computationally expensive, especially when considering transient behaviour, which makes real-time simulations almost impossible, especially for large-scale areas. To emulate this time consuming numerical simulation, it is investigated whether data driven models can provide a quick estimation of the slope condition and hence speed up the assessment process. The approach aims to provide a method to estimate the safety factor by only using observable data.

- **Research question 4: How can Earth observation be deployed as a monitoring tool for the assessment of dikes?**

Dike inspections usually involve visual examination of the dike, usually by walking along the dike. Various components of the dike are observed and details are recorded focusing on indicators of weakness and damage. For instance, in the Netherlands dike observers use Fig. 1.1 to assess cover quality of dikes. According to this guide, the cover quality is described in four classes: good, reasonable, mediocre and bad. The description of each category can be found in Fig. 1.1. This description is qualitative and not specific; however, by using more quantitative measures (i.e. Vegetation Indices (VIs)) this description can be improved or augmented. Additionally, VIs could be monitored remotely for dikes. The ability of remote sensing to aid dike inspection is investigated, based on what can be observed, the coverage and accuracy of available observations and the ability of these observations to indicate weakness. The investigation introduces remote sensing as a tool that could increase efficiency, coverage and objectivity of dike inspections. Dike related remote sensing inspection indicators include measurable parameters such as VIs, soil moisture and displacement.

### 1.3. THE RELIABLE DYKES PROJECT

This research is performed as a part of the Reliable Dykes project (Project No. 13864) funded by the Netherlands Organisation for Scientific Research (NWO) domain Applied and Engineering Sciences (TTW). The Reliable Dykes project aims to improve the understanding of analysing and quantifying the influence of uncertainties in the regional dikes assessment in the Netherlands. This project is structured within 4 PhD projects and 1 post-doctoral researcher; the first PhD project (de Gast, 2020), investigated how to measure heterogeneity within and under dikes, undertook a large scale dike failure experiment, and combined these two aspects to simulate the failure using the Random Finite Element Method (RFEM). The second PhD project (Muraro, 2019) focused on the behaviour of peat, a type of soil that can often be found in the regional dikes. The PhD resulted in recommendations on how to carry out and interpret laboratory testing on peat and on the selection of material parameters. The third PhD thesis (Varkey, 2020) considered several improvements to the analysis of spatially variable dikes, including

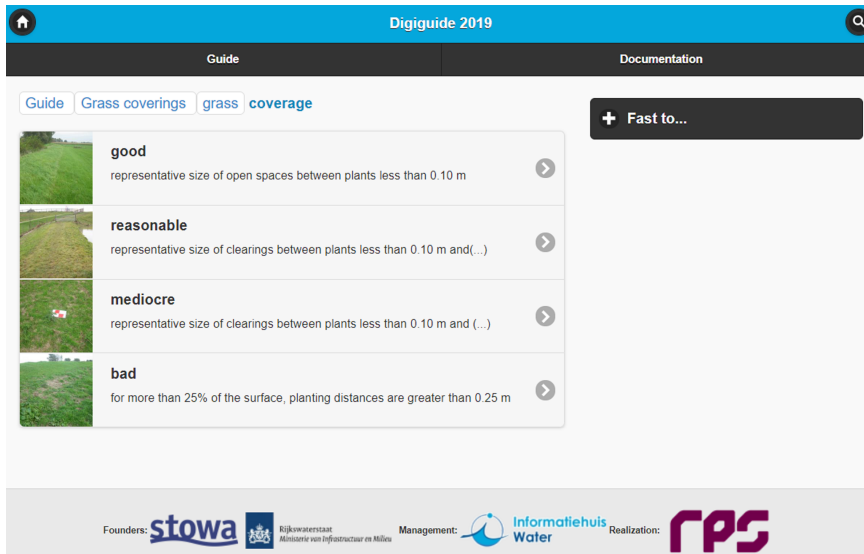


Figure 1.1: Grass cover quality in the Netherlands is assessed based on this table (Digiguide (2019) translated by Google Translate). Digiguide (2019) aids inspectors by providing a database of reference figures to assess the visually observed cover quality based on them.

improving an analytical method and the use of deterministic methods and investigating the 3D geometry variation of a dike. The fourth PhD project has resulted in this thesis. The post-doctoral researcher (van den Eijnden & Hicks, 2017) developed several assessment tools and developed the connection between these tools and industry for real applications.

## 1.4. OVERVIEW OF THE THESIS

The overview of thesis outline is illustrated in Fig. 1.2. The thesis is introduced and concluded at the beginning and end, respectively in Chapter 1 (Introduction) and Chapter 6 (Conclusion and discussion), shown by green boxes. In the other four chapters, the research questions are addressed. Chapters 2 and 3 utilise numerical simulation to investigate the impact of SVA interaction on the dike stability and the impact of evaporation induced cracking, respectively – indicated by a blue box – in Fig. 1.2. The first research question is treated in Chapter 2, which is based on a journal article published in *Environmental Geotechnics* (Jamalinia et al., 2019). Chapter 3 focuses on a shrinkage behaviour of a soil and drought conditions for an example dike. The adopted integrated crop-geotechnical model simulates the temporal (daily) dike stability for 10 years; this chapter is built based on an article published in *Computers and Geotechnics* (Jamalinia et al., 2020). Chapters 4 and 5 investigate the potential of monitoring tools to enhance stability assessments (shown by pink box in Fig. 1.2). In Chapter 4, the results of Chapter 3 are utilised to investigate the third research question; part of this chapter is written based on a journal article published in *Water* (Jamalinia et al., 2021). In Chapter 5, the

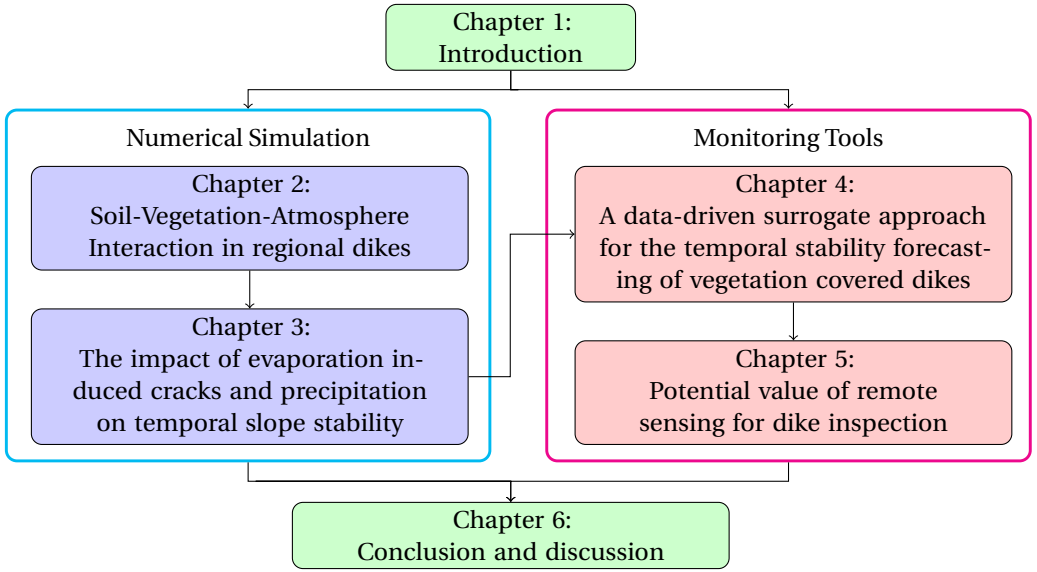


Figure 1.2: Schematic outline of the thesis.

outcome of the previous chapters is utilised to introduce the possibility of using Remote Sensing for dike monitoring to facilitate frequent monitoring over larger areas. Chapter 6 concludes the thesis by summarising the main contributions of this research, suggesting possible future research and also providing recommendations.

## REFERENCES

- Baudena, M., von Hardenberg, J. & Provenzale, A. (2013). Vegetation patterns and soil-atmosphere water fluxes in drylands. *Advances in Water Resources* **53**, 131–138, doi: 10.1016/j.advwatres.2012.10.013.
- Bouman, B. A. M., Schapendonk, A. H. C. M., Stol, W. & Van Kraalingen, D. W. G. (1996). Description of LINGRA, a model approach to evaluate potential productivities of grasslands in different European climate regions. *Quantitative Approaches in System Analysis* **7**, 11–58.
- Brooks, S. M., Anderson, M. G. & Collison, A. J. C. (1995). Modelling the role of climate, vegetation and pedogenesis in shallow translational hillslope failure. *Earth Surface Processes and Landforms* **20**, No. 3, 231–242, doi:10.1002/esp.3290200305.
- CIRIA (2013). *The International Levee Handbook*. London, UK: CIRIA (Construction Industry Research and Information Association), MEDE (Ministère de l'Ecologie du Développement durable et de l'Energie) and USACE (US Army Corps of Engineers).
- Cundill, S. (2016). *Investigation of remote sensing for dike inspection*. Ph.D. thesis, University of Twente, doi:10.3990/1.9789036540360.
- de Gast, T. (2020). *Dykes and embankments: A geostatistical analysis of soft terrain*. Ph.D. thesis, Delft University of Technology, the Netherlands, doi:10.4233/uuid:4ce3b4ec-0a6a-4886-9a82-5945a1f9ea50.
- Digigids (2019). Grasbekleding. URL <http://digigids.hetwaterschapshuis.nl/index.php?album=Grasbekleding-2019-/gras/bedekkingsgraad>.
- Dunbar, J. B., Galan-Comas, G., Walshire, L. A., Wahl, R. E., Yule, D. E., Corcoran, M. K., Bufkin, A. L. & Llopis, J. M. L. (2017). Remote sensing and monitoring of earthen flood-control structures. *Technical report*, United States Army Corps of Engineers Engineer Research and Development Center (U.S.) Geotechnical and Structures Laboratory (U.S.), doi:10.21079/11681/22804.
- Greenwood, J. R., Norris, J. E. & Wint, J. (2007). Discussion: Assessing the contribution of vegetation to slope stability. *Proceedings of the Institution of Civil Engineers - Geotechnical Engineering* **160**, No. 1, 51–53, doi:10.1680/geng.2007.160.1.51.
- Hasan, K., Aanstoos, J. V. & Mahrooghy, M. (2013). Stressed vegetation identification by SAR time series as an indicator of slope instability in Mississippi river levee segments. In *Applied Imagery Pattern Recognition Workshop (AIPR): Sensing for Control and Augmentation*, IEEE, pp. 1–4, doi:10.1109/AIPR.2013.6749307.
- Hemmati, S., Gatmiri, B., Cui, Y. J. & Vincent, M. (2012). Thermo-hydro-mechanical modelling of soil settlements induced by soil-vegetation-atmosphere interactions. *Engineering Geology* **139-140**, 1–16, doi:10.1016/j.enggeo.2012.04.003.
- Jamalinia, E., Tehrani, F. S., Steele-Dunne, S. C. & Vardon, P. J. (2021). A data-driven surrogate approach for the temporal stability forecasting of vegetation covered dikes. *Water* **13**, No. 1, 107, doi:10.3390/w13010107.

- Jamalinia, E., Vardon, P. J. & Steele-Dunne, S. C. (2019). The effect of soil-vegetation-atmosphere interaction on slope stability: a numerical study. *Environmental Geotechnics*, **Ahead of print**, doi:10.1680/jenge.18.00201.
- Jamalinia, E., Vardon, P. J. & Steele-Dunne, S. C. (2020). The impact of evaporation induced cracks and precipitation on temporal slope stability. *Computers and Geotechnics* **122**, 103506, doi:10.1016/j.compgeo.2020.103506.
- Muraro, S. (2019). *The deviatoric behaviour of peat: A route between past empiricism and future perspectives*. Ph.D. thesis, Delft University of Technology, The Netherlands, doi:10.4233/uuid:ffbea4e0-2e97-4d41-819d-beec42120b29.
- Osman, N. & Barakbah, S. (2006). Parameters to predict slope stability—soil water and root profiles. *Ecological Engineering* **28**, No. 1, 90–95, doi:https://doi.org/10.1016/j.ecoleng.2006.04.004.
- Pedone, G., Tsiampousi, A., Cotecchia, F. & Zdravkovic, L. (2016). Effects of soil-vegetation-atmosphere interaction on the stability of a clay slope: A case study. *E3S Web of Conferences* **9**, 15002, doi:10.1051/e3sconf/20160915002.
- Plaxis BV (2018). PLAXIS Reference Manual 2018. *Technical report*, Delft, the Netherlands.
- Robinson, J. D. & Vahedifard, F. (2016). Weakening mechanisms imposed on California's levees under multiyear extreme drought. *Climatic change* **137**, No. 1, 1–14, doi:10.1007/s10584-016-1649-6.
- Stokes, A., Norris, J. E., van Beek, L. P. H., Bogaard, T., Cammeraat, E., Mickovski, S. B., Jenner, A., Di Iorio, A. & Fourcaud, T. (2008). How vegetation reinforces soil on slopes. In *Slope Stability and Erosion Control: Ecotechnological Solutions* (Norris, J. E., Stokes, A., Mickovski, S. B., Cammeraat, E., van Beek, R., Nicoll, B. C. & Achim, A., eds.), Dordrecht: Springer Netherlands, pp. 65–118, doi:10.1007/978-1-4020-6676-4\_4.
- TAW (Technical Advisory Committee for Flood Defence) (1996). Clay for Dikes. *Technical report*, The Road and Hydraulic Engineering Institute, Delft, the Netherlands.
- Tsiampousi, A., Zdravkovic, L. & Potts, D. M. (2016). Numerical study of the effect of soil-atmosphere interaction on the stability and serviceability of cut slopes in London clay. *Canadian Geotechnical Journal* **54**, No. 3, 405–418, doi:10.1139/cgj-2016-0319.
- Vahedifard, F., Sehat, S. & Aanstoos, J. V. (2017). Effects of rainfall, geomorphological and geometrical variables on vulnerability of the lower Mississippi River levee system to slump slides. *Georisk: Assessment and Management of Risk for Engineered Systems and Geohazards* **11**, No. 3, 257–271, doi:10.1080/17499518.2017.1293272.
- van Baars, S. (2005). The horizontal failure mechanism of the Wilnis peat dyke. *Géotechnique* **55**, No. 4, 319–323, doi:10.1680/geot.2005.55.4.319.
- van den Eijnden, A. P. & Hicks, M. A. (2017). Efficient subset simulation for evaluating the modes of improbable slope failure. *Computers and Geotechnics* **88**, 267–280, doi:10.1016/j.compgeo.2017.03.010.

- Vardon, P. J. (2015). Climatic influence on geotechnical infrastructure: a review. *Environmental Geotechnics* **2**, No. 3, 166–174, doi:10.1680/envgeo.13.00055.
- Varkey, D. (2020). *Geotechnical uncertainties and reliability-based assessments of dykes*. Ph.D. thesis, Delft University of Technology, The Netherlands, doi:10.4233/uuid:48460103-30a0-4338-8c4a-ebc80c73c2d3.
- Wang, B., Vardon, P. J. & Hicks, M. A. (2018). Rainfall-induced slope collapse with coupled material point method. *Engineering Geology* **239**, 1–12, doi:10.1016/j.enggeo.2018.02.007.



# 2

## SOIL-VEGETATION-ATMOSPHERE INTERACTION IN REGIONAL DIKES

*The stability of a dike is influenced strongly by its water content, via changes in effective stress and weight. While flow through porous media is relatively well understood, water flux in and out of a dike through a vegetated surface is not as well understood. This chapter presents a numerical study of the Soil-Vegetation-Atmosphere (SVA) interaction and discusses how it influences the stability of dikes covered with grass. A crop model is used to simulate vegetation growth, and infiltration in response to meteorological forcing. The PLAXIS Finite Element Method (FEM) model is used to simulate the impact of this infiltration on hydro-mechanical behavior and dike stability. Results from a four-year analysis indicate a strong correlation between root zone water content ( $WC_{rz}$ ) and Factor of Safety (FoS), although not a unique relationship; other parameters also have impacts on FoS. For instance, Leaf Area Index (LAI) was also found to have a strong, lagged correlation with the water flux into the dike; therefore, it has an indirect influence on safety. This suggests that monitoring LAI could be a useful tool to identify vulnerable locations along dikes. It is therefore proposed that vegetation and root zone water content could be used as an indication to detect vulnerable dikes in early stage.*



## 2.1. INTRODUCTION

**D**IKES in the Netherlands are typically covered by clay and reinforced by grass. This provides an effective covering to the construction, protecting from soil erosion, especially for river dikes (TAW (Technical Advisory Committee for Flood Defence), 1996). Vegetation growth and health are influenced by the ground: soil texture, nutrient availability, hydraulic properties and moisture availability. They also depend on climatic conditions: precipitation, radiation and temperature. A recent study from Vardon (2015) identified the major climatic variations expected to influence geotechnical infrastructure: increasing temperature (leading to soil drying), increasing average rainfall (leading to lower soil suction), increasing drought events (causing drying and soil desiccation) and increasing intense precipitation (leading to soil erosion, flooding and hydro-mechanical failure).

Dike inspectors conduct visual inspections of the dike surface, including vegetation, in order to identify deterioration or damage. Recent studies have highlighted the value of using the vegetation condition as an indicator of subsurface conditions. For instance, Hasan *et al.* (2013) concluded that grass growing over areas with cracks and fractures was stressed due to a lack of moisture compared to grass over other areas, during winter and early spring.

According to the Dutch guidelines (Digigids, 2019), vegetation is one of the factors that dike inspectors should evaluate in their observation, by which the vegetation quality for each location is assessed and classified as good, medium, poor or bad (Cundill, 2016). However, these definitions are neither well defined nor specific. Using vegetation indices would provide a more objective and quantitative indicator. Furthermore, using Earth observation data, i.e. remote sensing, to map vegetation indices facilitates large-scale monitoring and can be used to identify areas of interest for further investigation.

Few studies have investigated the impact of vegetation on the water fluxes into dikes and its consequential effect on stability, for example, Hemmati *et al.* (2012), Tsiampousi *et al.* (2016), Rahardjo *et al.* (2013) and Elia *et al.* (2017). This study aims to bridge this gap by investigating the effect of vegetation in dike analysis assuming a typical regional dike covered with grass. Here it is hypothesised that vegetation and the surface layer of the soil act as a hydraulic buffer to the rest of the dike. Furthermore, vegetation responds to water content variations in the root zone leading to the possibility of using it as a dike health indicator. In the current chapter, a crop growth model is coupled to a geotechnical model to enable the investigation of Soil-Vegetation-Atmosphere (SVA) interaction due to the climatic conditions. The changes in the stability of a conceptual dike, based on the geometry and materials of a regional dike in the Netherlands, is investigated. In this initial study, cracking and desiccation of soil is not included, but proposed approach offers the opportunity to do so in a further study.

## 2.2. METHOD

The system of interest is an idealised regional dike. The cross-section is illustrated in Fig. 2.1. The dike is 2 m high and 41 m wide and the water levels on the left and right sides are 3 m and 2 m respectively. The dike's surface is vegetated, with a permanent root zone depth (*ROOTDM*) of 40 cm extended over the surface layer (red area in Fig. 2.1).

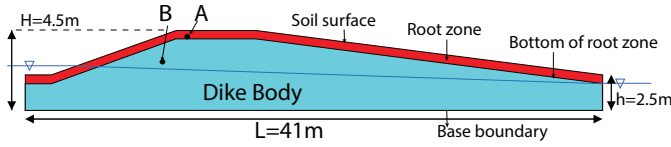


Figure 2.1: Geometry representing boundary, root zone layers with the 40 cm depth, canal water levels, and points in which following results are plotted.

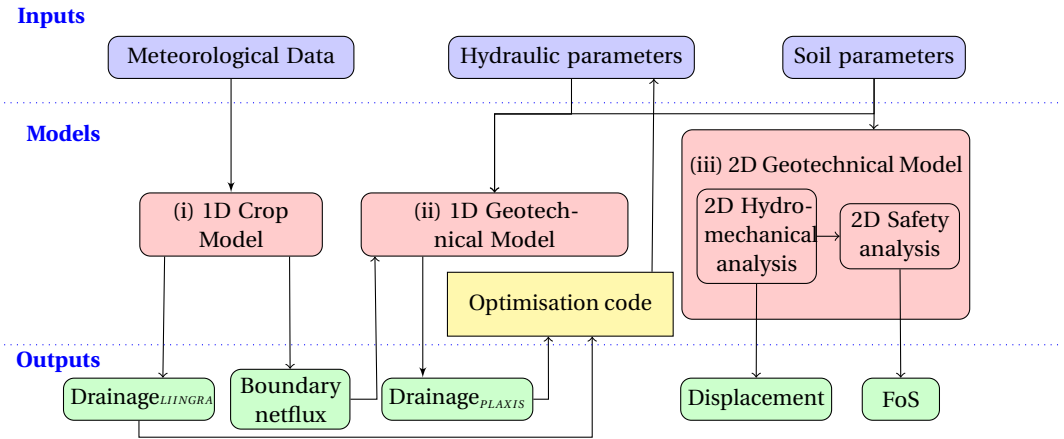


Figure 2.2: Flow chart for numerical solution procedure.

The modelling strategy is as follows: (i) A 1D crop model is used to simulate the infiltration of water into and out of the root zone. This model uses weather data as input, calculates the evaporation, transpiration, water interception by the vegetation, drainage from the root zone layer and vegetation growth. (ii) A 1D geotechnical model is used to simulate the hydraulic behaviour of the root zone, where only the calculated water in step (i) entering the root zone is applied as a top boundary condition. The hydraulic material properties of the root zone are optimised so that the drainage from the bottom of the root zone matches in both models. (iii) A 2D geotechnical model is used to simulate the hydro-mechanical behaviour in time, including both the displacement and the Factor of Safety (FoS). An overview of this process is given in the flowchart in Fig. 2.2.

There are then three boundaries of interest in Fig. 2.1: (1) the soil surface; (2) the bottom of the root zone (top of the dike body) which represent the coupling interface between the crop model and the geotechnical model; and (3) the base boundary of the dike that is assumed to be impermeable (due to underlying clay layers, a reasonable alternative could be a fixed pore pressure where groundwater pressures are constant or known and the underlying soil is permeable). Results are plotted at points A and B during the analyses, which are representative locations in the root zone and the dike body. The phreatic surface is calculated in the geotechnical model. The vadose zone is of limited

thickness and consists mainly of the root zone.

### 2.2.1. CROP MODEL

The LINGRA (LINTUL GRAssland) (Schapendonk *et al.*, 1998) model is used for simulating the processes governing infiltration from the surface layer in response to climatic conditions and the consequential vegetation growth. LINGRA was designed for applications such as yield forecasting, quantitative land use evaluation, and investigating the effects of climate change on grass yields (Schapendonk *et al.*, 1998). This model is based on the LINTUL (Light INTerception and Utilization simulator) concept (Spitters, 1987), which was designed to simulate crop growth under atmospheric conditions. LINGRA is specifically for grass growth, and the model can account for growth in water-limited condition which is the case for the grass on dikes. The main components of interest are the water balance and leaf growth. A more complete description of the model is provided by Shibu *et al.* (2010) and Bouman *et al.* (1996) and is summarised below.

### 2.2.2. WATER BALANCE EQUATION

LINGRA solves a 1D mass balance equation in the root zone using a tipping bucket approach (Bouman *et al.*, 1996). The soil water balance is calculated for the root zone layer (Fig. 3.3), whose thickness is defined by the length of the root and has a predefined water storage capacity (Shibu *et al.*, 2010).

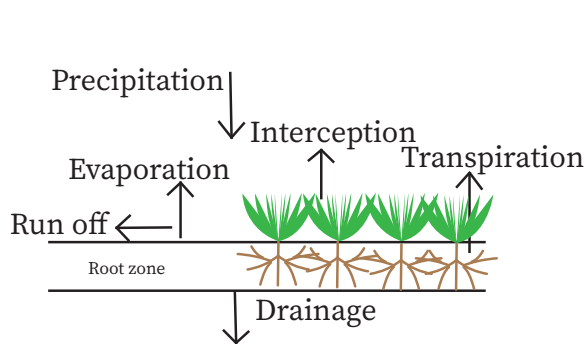


Figure 2.3: Root zone water balance in LINGRA.

The daily changes in the amount of water stored in the root zone,  $\Delta WA$ , is calculated from the "effective precipitation" (precipitation ( $P$ ) minus interception ( $In$ )), minus bare soil evaporation ( $E$ ) and transpiration ( $T$ ) (collectively referred to as evapo-transpiration,  $ET$ ), minus drainage ( $D_L$ ) and run-off ( $Rn$ ):

$$\Delta WA = P - In - ET - D_L - Rn \quad (2.1)$$

All quantities are in  $m\ day^{-1}$ . The interception and evapo-transpiration are dependent on the amount of vegetation, quantified as the Leaf Area Index ( $LAI$ ,  $m^2\ leaf\ m^{-2}\ ground$ ). When the amount of water in the root zone reaches the field capacity, the excess water

drains from the lower boundary of the root zone. This drainage flux ( $D_L$ ) is limited by the maximum drainage rate ( $DRATE$ ) of the subsoil. Additional water leaves as run off ( $Rn$ ). In this crop model upward water flow (capillary rise) is disregarded and lateral influx or outflux of water is not considered (Bouman *et al.*, 1996). However, in the geotechnical model these fluxes are included. This means that the impact of the water distribution on safety is included, but the lateral distribution of vegetation cover is not. The impact of the capillary rise not being considered in the crop model is considered to be minor as permeability strongly reduces due to desaturation when capillary rise would occur. Lateral flow being included in the geotechnical will create variations around the average considered in a 1D model and allow the impact on safety to be included. An optimisation routine (see below) ensures that there is mass balance between the two models. Both of these impacts should be investigated further to quantify the impact.

### 2.2.3. LEAF GROWTH EQUATION

Leaf growth is calculated from the amount of assimilates (sugars and amino acids) available for growth due to photosynthesis (Bouman *et al.*, 1996). Leaf death rate by senescence is calculated by means of a relative death rate, which is computed from the leaf area index and the ratio of the actual transpiration over the potential transpiration. A high leaf area index (LAI) leads to internal shading of the lower leaves which results in leaf senescence. Leaf area development is also affected by grassland management, e.g. mowing. In LIN-GRASS, two standard management options are implemented (to be selected by the user): periodic mowing and mowing at a constant biomass level (Bouman *et al.*, 1996).

$LAI$  influences the water balance equation via both transpiration and interception. Water demand for transpiration varies throughout the calendar year; peaking during summer, when  $LAI$  increases, and reducing during winter, when it decreases. Vegetation growth rate, here defined by leaves growth, calculates as Eq. 2.2:

$$\Delta LAI = SLA \times f(lv) \times \Delta W - \Delta LAI_d \quad (2.2)$$

where  $\Delta LAI$  is Leaf Area Index increase,  $SLA$  is Specific Leaf Area ( $m^2 g^{-1}$ ),  $f(lv)$  is the fraction of dry vegetation matter to leaves (-),  $\Delta W$  is the growth rate of crop dry (solid) matter ( $g m^{-2} day^{-1}$ ),  $\Delta LAI_d$  is death rate of leaf area ( $m^2 leaf m^{-2} ground day^{-1}$ ).

### 2.2.4. GEOTECHNICAL MODEL

The commercial finite element code, Plaxis 2D (Plaxis BV, 2018), was used in this study. This geotechnical model is discretised with 15-noded plane-strain triangular elements. The workflow is controlled via the Plaxis Python interface.

### 2.2.5. HYDRO-MECHANICAL ANALYSIS

A fully coupled flow-deformation analysis is used to simultaneously simulate pore water pressure (pwp) and displacements of the dike under transient (saturated and unsaturated) flow conditions. The formulation is based on Biot's theory (Biot, 1941), ensuring equilibrium and continuity of the soil-water mixture is satisfied. Stress equilibrium and the Richard's equation (Richards, 1931) are used to govern the mechanical and hydraulic behaviour, respectively, with an extended effective stress used in the mechanical equation.

The Richards' equation can be used to describe unsaturated flow in a porous medium and utilises an unsaturated form of Darcy's law to calculate the fluid flux as:

$$\underline{q} = \frac{k_{rel}}{\rho_w g} \underline{k}_{sat} (\nabla pwp + \rho_w \underline{g}) \quad (2.3)$$

where  $\underline{q}$  is the vector of specific discharge;  $\underline{k}_{sat}$  is the saturated hydraulic conductivity matrix;  $\rho_w$  is water density;  $\nabla pwp$  is gradient of the pore water pressure that causes the water to flow;  $\underline{g}$  is vector of gravitational acceleration; and  $k_{rel}$  is relative permeability, defined as the ratio of the hydraulic conductivity at a given saturation to  $\underline{k}_{sat}$  (Galavi, 2010). The Mohr-Coulomb constitutive model is used to govern the mechanical behaviour and the van Genuchten-Mualem model (van Genuchten, 1980) is used to govern the suctions developed from the changes in water content. The van Genuchten-Mualem model is defined as:

$$\theta = \theta_r + (\theta_{sat} - \theta_r) [1 + |\alpha h|^n]^{-m} \quad (2.4)$$

where  $\theta$  is water content at a given suction  $h$ ;  $\theta_r$  is residual water content;  $\theta_{sat}$  is water content at saturated conditions;  $n$  and  $m$  are soil water retention curve (SWRC) fitting parameters; and  $\alpha$  is a parameter related to the air entry value.

### 2.2.6. SAFETY ANALYSIS

To obtain the Factor of Safety (FoS) variation with time, a safety analysis was performed at various (user defined) time steps after the coupled analysis. The strength reduction technique was employed to calculate the FoS against macro-instability, where the shear strength parameters  $\tan\phi$  and  $c$  of the soil are successively reduced until structure failure occurs (Plaxis BV, 2018); the ratio of the parameters at failure to the defined parameters gives the FoS:

$$FoS = \frac{\tan\phi_{input}}{\max(\tan\phi_{reduced})} = \frac{c_{input}}{\max(c_{reduced})} \quad (2.5)$$

where  $\phi_{input}$  and  $\phi_{reduced}$  ( $c_{input}$  and  $c_{reduced}$ ) are input and reduced friction angle (cohesion), respectively. Bishop's stress is utilised, where suction is included into effective stress, and therefore suction increases shear strength. A single FoS is calculated for the entire dike. Other failure mechanisms, such as piping or uplift, are not included in this assessment, nor is the possibility of cracking of the dike surface and consequential changes in strength and permeability.

### 2.2.7. COUPLING CROP AND GEOTECHNICAL MODELS

The coupling between the crop model and the geotechnical model is illustrated in Fig. 2.2. The geotechnical model does not include effect of vegetation, so the crop model is used to simulate the growth and decay of vegetation in response to meteorological forcing, and the available water amount in the root zone. The flux ( $Q_{net}$ ) that is applied to the surface boundary in the geotechnical model is defined as:

$$Q_{net} = P - In - ET \quad (2.6)$$

and a zero pore pressure boundary condition is applied on the base, to (a) be consistent with the crop model which is free draining from the base and (b) with the recognition that the phreatic surface will be close to the base of the root zone in this application.

To ensure that the root zone moisture dynamics are consistent between the two models, the hydraulic parameters in the root zone of the geotechnical model are optimised to ensure that the drainage from the root zone in the crop model ( $D_L$ ) is equal to that from 1D geotechnical model ( $D_p$ ). At each time step, the hydraulic parameters are optimised to minimise the Root Mean Square Difference (RMSD) between ( $D_L$ ) and ( $D_p$ ) - this is done automatically using a Python script.

$$F(k_{sat}, \alpha, n, m) = \min(\text{RMSD}(D_L, D_p)) \quad (2.7)$$

A 2D hydro-mechanical model is then used to calculate pore water pressure (pwp) and displacement over time. Finally the safety calculation is done as described in the previous section to produce the FoS against macro-instability as a function of time.

### 2.2.8. CASE STUDY

Two experiments were performed. In the first, four years of climatic data were used to obtain the FoS time series from 2009 to 2012 to understand the influence of meteorological conditions on the dike safety. Second, to understand the effect of vegetation alone, additional analyses of a single year was simulated for different (fixed) values of  $LAI$ .

### 2.2.9. GEOMETRY

The dike geometry used is representative of a regional dike in Amsterdam, the Netherlands, studied in the Veenderij project (de Vries, 2012) and is shown in Fig. 2.1. The vegetation is employed in this study is grass cover with a permanent root depth of 40 cm, equals to the maximum root depth for the considered vegetation (Table 2.1).

### 2.2.10. METEOROLOGICAL DATA

Meteorological data, such as precipitation, solar radiation, average air temperature, wind speed and vapour pressure taken in the early morning at Schiphol Airport (Amsterdam) station (52° 19' 04° 47' OL) has been obtained from the The Royal Netherlands Meteorological Institute (KNMI) for 2009 to 2012 (Fig. 2.4). These data are used as inputs for the crop model.

### 2.2.11. ROOT ZONE: CROP MODEL

The key parameters required by the crop model for both soil and vegetation are listed in Table 2.1. The values are typical for Dutch soil conditions and typical grass cover, based on reported values by Bouman *et al.* (1996). The listed parameters are divided into two groups, soil and vegetation parameters. In soil parameters, water content at field capacity ( $\theta_{fc}$ ) is the maximum water storage capacity of the root zone, which is defined as the volumetric water content at a soil moisture suction of 10 kPa or pF 2.0. The water content at field capacity is therefore lower than water content at saturation (van Laar *et al.*, 1997). The water content at the wilting point ( $\theta_{wp}$ ) is the limit of water content, below which plant water uptake ceases and plants start to wilt. Below the critical water content ( $\theta_{cr}$ ),

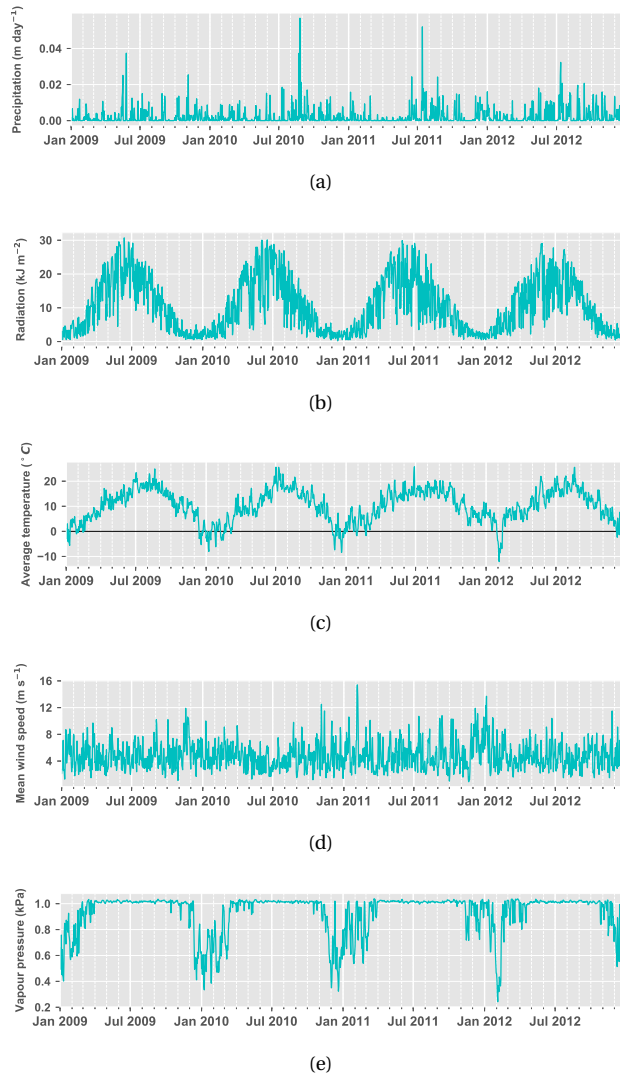


Figure 2.4: Daily values of inputs for the crop model from 2009 to 2012 (a) Precipitation; (b) Radiation; (c) Average temperature; (d) Mean wind speed; (e) Vapour pressure in the early morning.

transpiration is reduced by water stress. Drainage is limited by the maximum drainage rate ( $DRATE$ ) of the subsoil. Perennial ryegrass is considered as the vegetation cover and has the majority (85%) of its root system in the shallow soil layer of 0-40 cm below soil surface (Bouman *et al.*, 1996), therefore the root depth for this permanent grassland is considered fixed at 40 cm. The Specific Leaf Area ( $SLA$ ; leaf area/ leaf mass) determines how much new leaf area to deploy for each unit of biomass produced. Critical leaf area beyond which death due to self shading occurs is defined as  $LAI_{CR}$  (Wolf, 2006).

Table 2.1: Input parameters used for the crop model.

LINGRA	Parameters	Value
Soil	Water content at field capacity ( $\theta_{fc}$ )	0.29 (cm <sup>3</sup> water cm <sup>-3</sup> soil)
	Water content at wilting point ( $\theta_{wp}$ )	0.12 (cm <sup>3</sup> water cm <sup>-3</sup> soil)
	Critical water content ( $\theta_{cr}$ )	0.005 (cm <sup>3</sup> water cm <sup>-3</sup> soil)
	Maximum drainage ( $DRATE$ )	50 (mm day <sup>-1</sup> )
Vegetation	Maximum root depth ( $ROOTDM$ )	40 (cm)
	Specific Leaf Area ( $SLA$ )	0.025 (m <sup>2</sup> g <sup>-1</sup> )
	Remaining $LAI$ after cutting ( $CLAI$ )	0.8 (m <sup>2</sup> leaf m <sup>-2</sup> ground)
	$LAI$ beyond that shading occurs ( $LAI_{CR}$ )	4 (m <sup>2</sup> leaf m <sup>-2</sup> ground)

### 2.2.12. GEOTECHNICAL MODEL

The sample dike includes two types of soils: the root zone in which properties should be consistent with the crop model, and the soil of the dike body. Constitutive and hydraulic parameters for the two mentioned parts of the dike are listed in Table 2.2. The values are based on the default soil properties from the Plaxis library for the root zone (silt clay) and for the dike body (organic clay), except for the hydraulic values of the root zone which are obtained from the optimisation code.

## 2.3. RESULTS AND DISCUSSION

### 2.3.1. TIME SERIES OF THE SVA INTERACTION VARIABLES

Figs. 2.5(a)-(d) show the temporal pattern of crop model outputs: Leaf Area Index ( $LAI$ ), boundary net flux ( $Q_{net}$ ), root zone water content ( $WC_{rz}$ ) and drainage ( $D_L$ ); and in Figs. 2.5(e)-(g) the geotechnical model outputs are illustrated: pore water pressure (pwp), magnitude of displacement and Factor of Safety (FoS) in the example dike from 2009 to 2012.

The  $LAI$  values in Fig. 2.5(a) reflect seasonal dynamics. The  $LAI$  is highest in spring and summer, since vegetation growth is energy-limited rather than water-limited. Reduced solar radiation limits growth in the autumn and winter. Higher  $LAI$  values in the summer lead to higher evapo-transpiration, and hence a reduction in the amount of water flux into the dike. The sudden decreases in  $LAI$  on 15 June and 15 August are due to grass mowing. These mowing events were imposed based on the mowing schedule for regional dikes in the Netherlands (T. Reuzenaar, 2017, Private Communication).



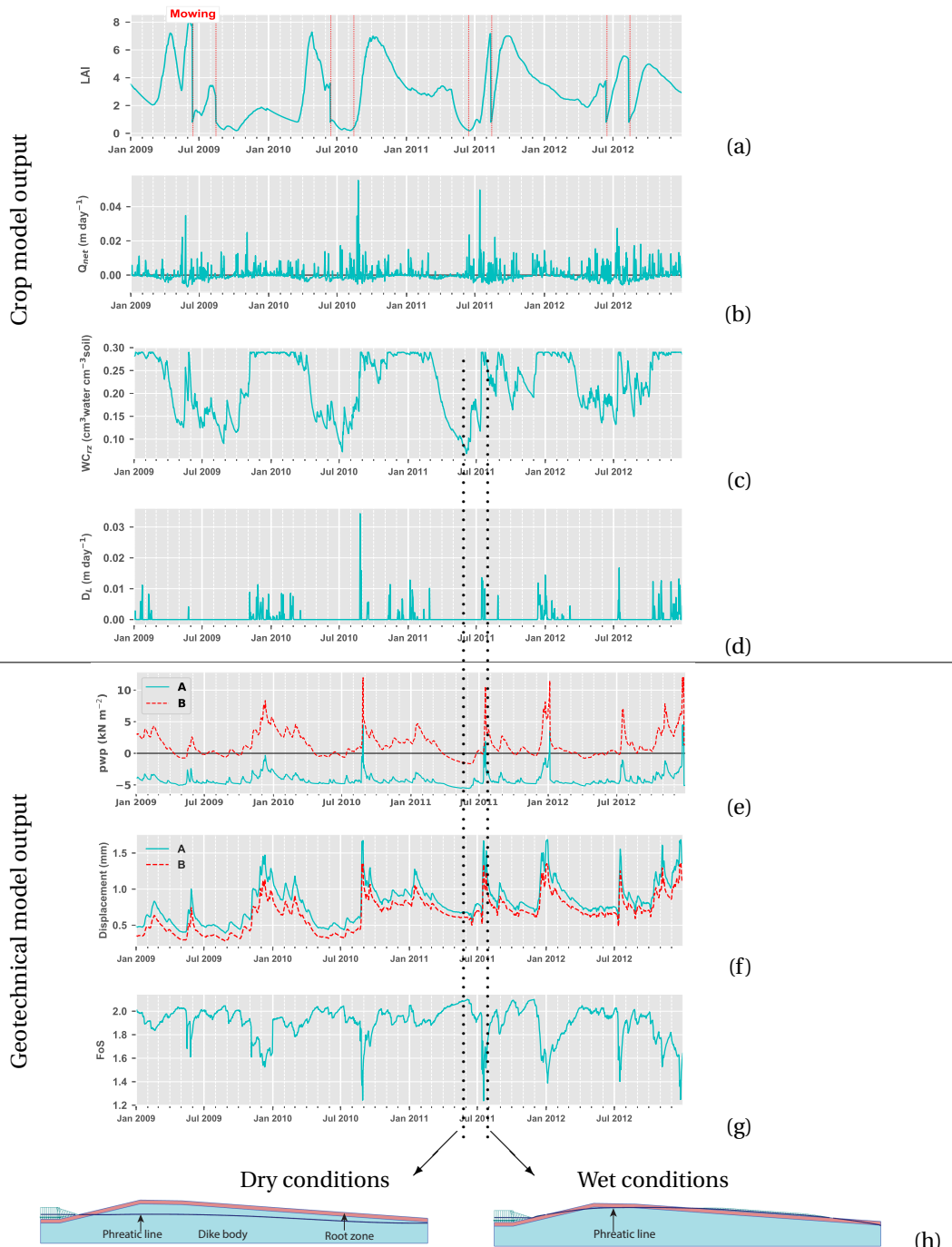


Figure 2.5: Daily values of (a) Leaf Area Index ( $LAI$ ); (b) Boundary net flux ( $Q_{net}$ ); (c) Root zone water content ( $W_{Crz}$ ); (d) Drainage from root zone to lower layers ( $D_L$ ); (e) Pore water pressure (pwp) at points A and B (compression is positive); (f) Magnitude of displacement at points A and B; and (g) Factor of Safety (FoS), over four years; (h) Phreatic line in a dry and wet condition.

Table 2.2: Input parameters used for the geotechnical model.

PLAXIS	Root zone	Dike body
<b>Constitutive model (Mohr-Coulomb)</b>		
Saturated unit weight ( $\gamma_{sat}$ )	20 (kN m <sup>-3</sup> )	12 (kN m <sup>-3</sup> )
Friction angle ( $\phi'$ )	23°	23°
Cohesion ( $c'$ )	2 (kPa)	2 (kPa)
Dilation angle ( $\psi$ )	0°	0°
Young's modulus ( $E'$ )	10 (MPa)	20 (MPa)
Initial void ratio ( $e_{int}$ )	0.67	1.2
<b>Hydraulic model (van Genuchten)</b>		
Hydraulic conductivity ( $k_{sat}$ )	0.14 (m day <sup>-1</sup> )	0.03 (m day <sup>-1</sup> )
Scale parameter $\alpha$	1.47 (m <sup>-1</sup> )	1.38 (m <sup>-1</sup> )
Fitting parameter $n$	1.97	1.32
Fitting parameter $m$	0.87	1.24

In Fig. 2.5(b), positive  $Q_{net}$  values occur in response to precipitation events. On days with near-zero precipitation and high  $LAI$ ,  $Q_{net}$  is negative as evaporative demand exceeds precipitation and then moisture in the root zone decreases, for example in April and May 2011.

In Fig. 2.5(c), the water content in the root zone is seen to decrease during the summer due to high levels of evapo-transpiration. It follows that during periods with a consistently high  $Q_{net}$ , the root zone reaches the field capacity. At this moment drainage is able to occur.

Drainage to the dike body ( $D_L$ ) is plotted in Fig. 2.5(d). As also seen in Figs. 2.5(b) and (c), drainage occurs when there is a positive (downward)  $Q_{net}$  and  $WC_{rz}$  reaches the field capacity. This can generally be seen in the winter months. A spike is also apparent in August 2010 when a large precipitation event occurred while the  $LAI$  was low.

In Fig. 2.5(b), the maximum  $Q_{net}$  during these four years is in August 2010 (0.055  $m\ day^{-1}$ ) which leads to the maximum  $D_L$  (0.034  $m\ day^{-1}$ ). However the second largest  $Q_{net}$ , 0.049  $m\ day^{-1}$ , is in Jul 2011 and it does not cause any drainage on the same day (Fig. 2.5(d)). This comes from the fact that there is more available storage in the root zone in the latter day ( $WC_{rz}=0.16\ (cm^3\ water\ cm^{-3}\ soil)$ ) relative to the former one ( $WC_{rz}=0.23\ (cm^3\ water\ cm^{-3}\ soil)$ ) as shown in Fig. 2.5(c). More limited drainage does occur in the days after the large rainfall in July 2011 due to additional rainfall and the saturated root zone.

In Fig. 2.5(e), the pore water pressure (pwp) at points A and B is shown. Positive and negative indicate pressure and suction, respectively. Comparing Figs. 2.5(d) and (e), it is clear that drainage from the root zone increases pwp. High drainage (August 2010), or long periods of cumulative drainage (winter 2009-2010), leads to higher pwp (soil is saturated) at points A and B. As expected, when the  $WC_{rz}$  decreases (e.g. during the spring), the pwp decreases. The highest suction (negative pwp) is observed at points A and B during the very dry spring 2011.

Comparing Figs. 2.5(d), (e) and (f), it is clear that drainage into the dike body increases pwp, which in turn increase (upwards) magnitude of displacement at points A and B. The

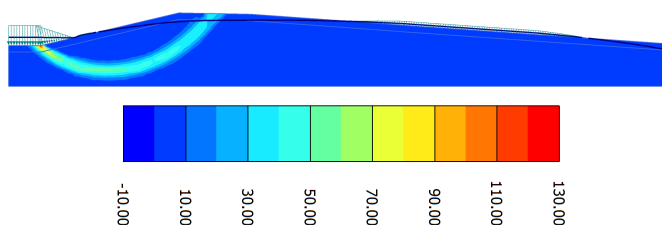


Figure 2.6: Deviatoric strain predicted during the failure calculation on the wet day, representing the failure mode.

displacement peaks following large precipitation events and recovers between events, showing a mainly elastic response. A slight accumulation of displacement over time is observed, due to plastic displacement.

In Fig. 2.5(g), the temporal variation of FoS is shown, which derived from the combined effect of precipitation and  $LAI$  that influence  $Q_{net}$ . A similar temporal pattern can be seen as exhibited in Figs. 2.5(f) and (g). The largest decrease in FoS corresponds to the maximum drainage, in August 2010. While, during dry periods when suction increases, the FoS tends to increase as well, for example in March-May 2011. However the relation is not fully proportional and further investigation is needed. It is noted that in extremely dry conditions, cracking in the surface of the dike could occur. This is not taken into account in the model.

Fig. 2.5(h) shows the phreatic line of the dike on two selected days. The sub-figure on the left represents a day where the dike is in a dry condition (in June 2011) with the very low  $WC_{rz}$ , thereby also a low pwp and high FoS. In comparison, on the right, is a sub-figure representing the dike in a wet condition (in July 2011) in which the saturation increased and the phreatic line rose in the soil body and reaches the surface on the downstream side.

In Fig. 2.6, the predicted failure mode is shown for the wet day mentioned earlier. The failure is circular and it fails into the water retaining side due to the asymmetric geometry of the dike.

### 2.3.2. $WC_{rz}$ INFLUENCE ON FOS

In order to study how the soil water content in the root zone influences the dike safety, FoS values are plotted against  $WC_{rz}$  in Fig. 2.7. During the simulated period, results suggest that a drier root zone (lower  $WC_{rz}$ ) leads to higher safety in the dike. This was expected, since the drier root zone leads to higher suction and then higher strength. However, it is also clear that it is not a unique relationship. To understand  $LAI$  effect on the SVA interaction the results in Fig. 2.7 are shaded by the  $LAI$ , with values increasing from white (low  $LAI$ ) to black (high  $LAI$ ). It can be seen that, generally, a dry root zone leads to low  $LAI$  values; however, low  $LAI$  does not correspond to low values of  $WC_{rz}$  in mowing and winter times. The minimum FoS values seem to occur at a mid-range value of  $LAI$  and high  $WC_{rz}$ , probably caused due to high antecedent water content, which leads to increased grass growth, but with a limited evapo-transpiration rate (caused at high  $LAI$  values). Neither  $WC_{rz}$  nor  $LAI$  have a unique relation with FoS, despite the strong

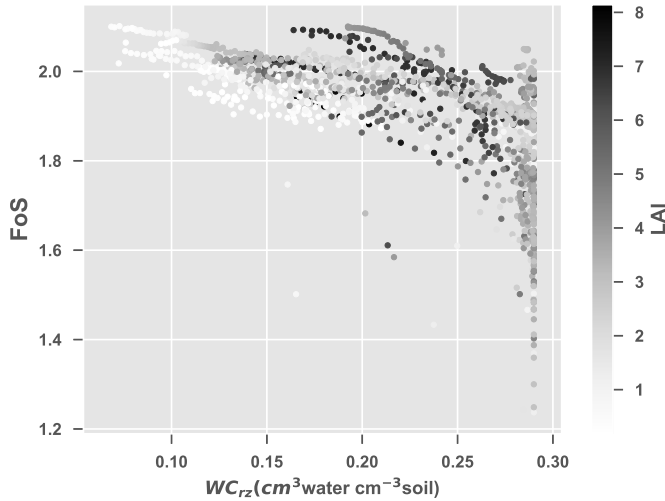


Figure 2.7: The FoS against the water content in the root zone ( $WC_{rz}$ ) during a simulation of four years. Points are shaded by the  $LAI$ .

trend. While the root zone is saturated, the FoS varies with the range of 2.1 to 1.2, and the difference between the situations can be understood by considering both  $LAI$  and drainage to the dike body in Fig. 2.5(d). When there is a noticeable drainage from root zone to the dike body, the FoS drops rapidly, as the overall pore-pressure distribution is dependance on the (history of) precipitation and vegetation/drainage conditions.

### 2.3.3. CORRELATION AMONG SELECTED SVA VARIABLES

Correlation coefficients between pairs of key variables have been calculated considering time, and are presented in Fig. 2.8. If the maximum absolute value of correlation occurs with a positive lag it means that the second term leads the first. If the peak correlation value occurs at a negative lag then the first term leads the second one.

The peak correlation coefficient between  $LAI$  and  $WC_{rz}$  ( $R = 0.31$ ), Fig. 2.8(a), is obtained with a 15 day lag, which means  $WC_{rz}$  affects the  $LAI$  the most after 15 days. This reflects that the vegetation grows in response to water content availability. The weak, though positive, correlation increases from a lag of -30 days, reaching a maximum at 15 days, and is still positive after 30 days. It is due to the fact that  $LAI$  is a result of  $WC_{rz}$  over a relatively long time. The amount of water in the root zone is not the only factor which influences the  $LAI$ , mowing and radiation have key roles in vegetation growth.

The correlation between  $WC_{rz}$  and FoS, Fig. 2.8(b), is negative, with no time lag. This agrees with the previous physical argument, that more available water in the root zone increases the mass of the dike (and the overturning moment) and decreases the strength.

In contrast to  $WC_{rz}$  there is a generally positive correlation between  $LAI$  and FoS, with 15 days lag, which is shown in Fig. 2.8(c). A high  $LAI$  results increased transpiration, leaf interception and reduced drainage into the dike (see next section).

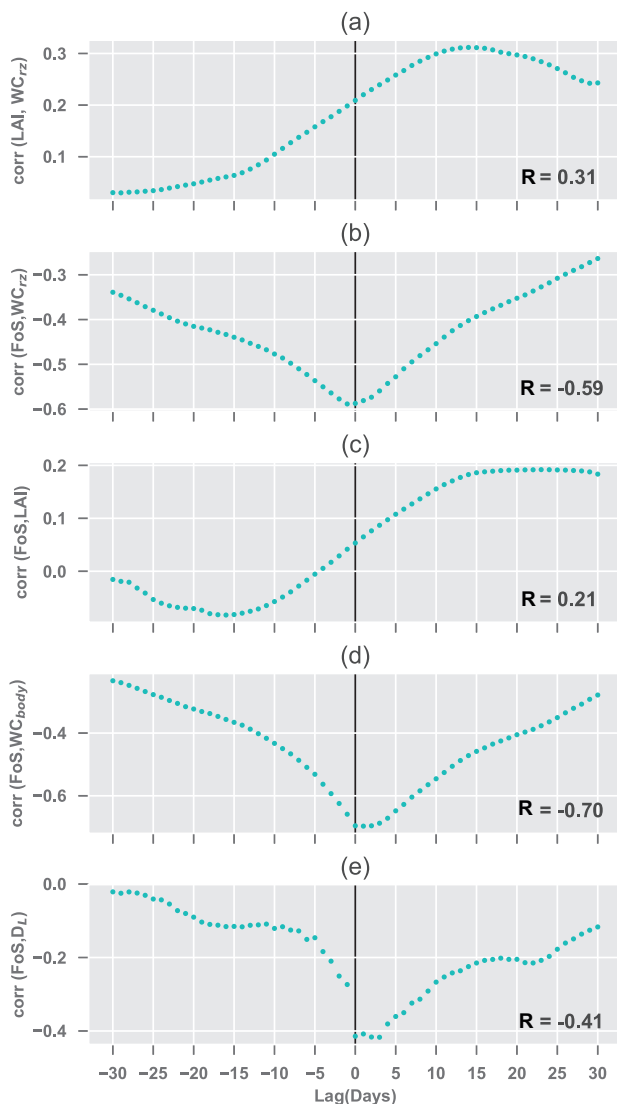


Figure 2.8: Correlation coefficient ( $R$ ) between two parameters with time lags up to 30 day during four years. A positive lag means that the second variable leads the first.

In Fig. 2.8(d) the correlation coefficient between the average water content in the dike body ( $WC_{body}$ ) and FoS is plotted which has the strongest correlation of all of the considered parameters. The water content in the dike body is calculated as a spatial

average of the whole body. It is shown that a higher  $WC_{body}$  leads to a lower FoS with no time lag, in other words they are negatively correlated. As with the water content in the root zone, the increased weight and reduced strength with an increase in water content is the cause of the negative correlation.

Water moves downwards through the dike, reducing effective stress thereby also reducing the strength; after water has passed through the dike, if there is no further rain the strength can recover. In the conditions when the ratio of shear strength to shear stress is the lowest the dike may fail.

Drainage from the root zone into the dike body, causes decreasing in FoS at the same day (Fig. 2.8(e)).  $D_L$  is the key driver for  $WC_{body}$ , drainage variations makes  $WC_{body}$  changes and then negatively affects FoS (Fig. 2.8(d)).

### 2.3.4. LAI EFFECT

As discussed in the previous section, the  $LAI$  varies due to multiple reasons including radiation, precipitation, root zone water content and mowing. Hence, it is difficult to explore the impact of solely the vegetation. To study the impact of the  $LAI$ , different constant values have been selected and the simulation re-run for a single year, i.e. 2010.

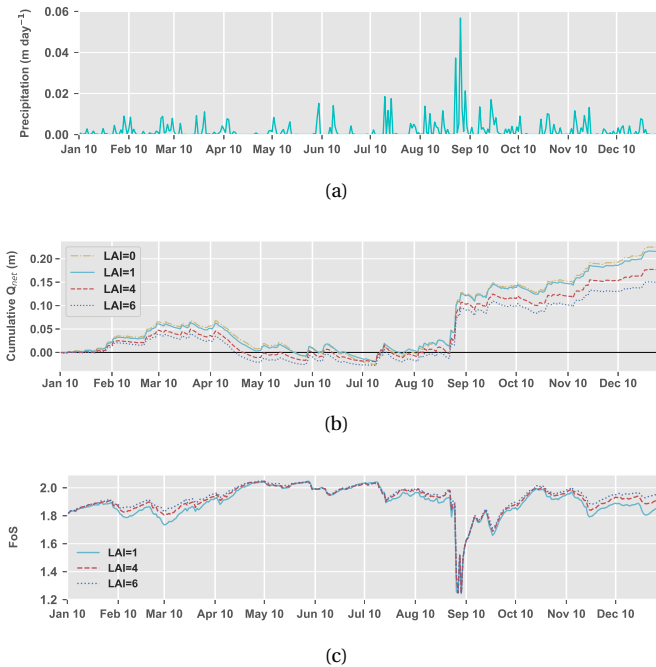


Figure 2.9: For different constant  $LAI$ s over 2010 (a) Precipitation (m day<sup>-1</sup>); (b) Cumulative boundary net flux (m); (c) Fos.

Fig. 2.9(a) shows the precipitation over the year and in Fig. 2.9(b) the cumulative boundary net flux (see Eq. 2.6) is plotted to describe how the  $LAI$  affects the  $Q_{net}$ . The differences between the values of  $Q_{net}$  stem solely from the differences in  $LAI$ , i.e.

changes in evapo-transpiration and leaf interception. Higher values of  $LAI$  lead to higher plant transpiration and leaf interception rate, but lower evaporation. As presented in Fig. 2.9(b), the case with no vegetation yields the highest  $Q_{net}$  throughout the whole year. The impact on FoS for 2010 is shown in Fig. 2.9(c). Since,  $Q_{net}$  for  $LAI=0$  and  $LAI=1$  is very similar, the safety calculation has been done only for the latter case. As expected, the wetter the dike (higher  $Q_{net}$ ), the lower the FoS. This occurs with a lower  $LAI$ , and so less vegetation, causes lower FoS; whereas, the case with the highest  $LAI$  generally leads to higher FoS over the year. This argument proves the positive correlation between  $LAI$  and FoS that has been shown in Fig. 2.8(c).

In a nutshell, presence of vegetation improves dike's safety since it decreases the water that reaches the root zone and consequently dike body. If  $LAI$  is 1, it represents very patchy vegetation, almost bare soil, and it is seen that in this case the FoS generally is less than the other two cases. This demonstrates the importance of including vegetation in regional dikes analysis.

## 2.4. THE POSSIBILITY OF USING VEGETATION AS A SAFETY INDICATOR

Vegetation is strongly coupled to the moisture available in a dike, and particularly in the root zone. Other meteorological aspects also govern this value, therefore a seasonal change is also seen. The vegetation responds to moisture in the root zone, which means that the vegetation follows the precipitation (most strongly after 15 days); therefore, it is likely that it could be used as an indicator of safety. Additionally, the lagged correlation between  $LAI$  and FoS meaning that it may be possible to utilise the  $LAI$  as a predictive tool. A reduced  $LAI$  will increase the boundary net flux ( $Q_{net}$ ) and reduce the FoS.

What is attractive is that the vegetation could quite easily be monitored remotely, i.e., via satellites or drones, rather than having to install physical sensors, which are extremely expensive with a limited coverage. A complicating factor is dike maintenance, i.e. mowing, which dramatically alters the  $LAI$  over a very short period of time, as well as the complex history dependent factors that affect the  $LAI$  and FoS. With a knowledge of the meteorological conditions, maintenance and the evolution of the vegetation, it may be possible to carry out history matching modelling on identified vulnerable areas to give a better insight into the conditions of the dike. It may be possible to have a staged process, where (i) vulnerable dikes are identified, using vegetation and root zone water content monitoring; (ii) numerical history matching is carried out to identify at-risk dikes; and (iii) the at-risk dikes are physically inspected. In each stage a more limited length of dike is considered.

One limitation of this work is the lack of consideration of surface cracking of the soil, which occurs in very dry conditions. Vegetation has been observed to reduce around cracks (i.e. Hasan *et al.*, 2013), probably due to enhanced drainage and evaporation. A lower  $LAI$  in this case will also indicate a weaker dike but for different reasons that previously discussed. The history matching will be complicated by this aspect.

To the author's knowledge, neither comprehensive field nor laboratory data are available to validate this numerical research and it is suggested for the future studies. The individual components which has been used in this study, LINGRA and PLAXIS, are

validated by Schapendonk *et al.* (1998) and Plaxis BV (2018).

## 2.5. CONCLUSION

In this chapter, the Soil-Vegetation-Atmosphere (SVA) interaction of an example dike covered with grass is investigated along with how this interaction governs a dike's hygroscopic condition and macro-stability. Two numerical models, a crop model and a geotechnical model were coupled to simulate SVA interaction over a period of four years. In the current chapter, the impact of surface cracking of the soil is not considered and the approach is yet to be validated with experimental data. It is shown that the amount of vegetation strongly affects the water flux into the dike and consequently impacts the factor of safety (FoS). The FoS is mostly dependent on the water content in both the root zone and the dike body, but that is affected by the vegetation. Moreover, the history of the precipitation and water content have an impact on both the FoS and the vegetation. It is therefore proposed that vegetation and root zone water content could be used as indicators to detect vulnerable dikes at an early stage.



## REFERENCES

- Biot, M. A. (1941). General theory of three-dimensional consolidation. *Journal of Applied Physics* **12**, No. 2, 155–164, doi:10.1063/1.1712886.
- Bouman, B. A. M., Schapendonk, A. H. C. M., Stol, W. & Van Kraalingen, D. W. G. (1996). Description of LINGRA, a model approach to evaluate potential productivities of grasslands in different European climate regions. *Quantitative Approaches in System Analysis* **7**, 11–58.
- Cundill, S. (2016). *Investigation of remote sensing for dike inspection*. Ph.D. thesis, University of Twente, doi:10.3990/1.9789036540360.
- de Vries, G. (2012). Monitoring droogteonderzoek veenkaden. *Technical report*, Deltares, Delft, the Netherlands (in Dutch).
- Digigids (2019). Grasbekledingen. URL <http://digigids.hetwaterschapshuis.nl/index.php?album=Grasbekledingen-2019-/gras/bedekkingsgraad>.
- Elia, G., Cotecchia, F., Pedone, G., Vaunat, J., Vardon, P. J., Pereira, C., Springman, S. M., Rouainia, M., Van Esch, J., Koda, E., Josifovski, J., Nocilla, A., Askarinejad, A., Stirling, R., Helm, P., Lollino, P. & Osinski, P. (2017). Numerical modelling of slope–vegetation–atmosphere interaction: an overview. *Quarterly Journal of Engineering Geology and Hydrogeology* **50**, No. 3, 249–270, doi:10.1144/qjgeh2016-079.
- Galavi, V. (2010). Groundwater Flow, Fully Coupled Flow Deformation and Undrained Analyses in PLAXIS 2D and 3D. *Technical report*, doi:10.13140/RG.2.1.1940.7763.
- Hasan, K., Aanstoos, J. V. & Mahrooghy, M. (2013). Stressed vegetation identification by SAR time series as an indicator of slope instability in Mississippi river levee segments. In *Applied Imagery Pattern Recognition Workshop (AIPR): Sensing for Control and Augmentation*, IEEE, pp. 1–4, doi:10.1109/AIPR.2013.6749307.
- Hemmati, S., Gatmiri, B., Cui, Y. J. & Vincent, M. (2012). Thermo-hydro-mechanical modelling of soil settlements induced by soil-vegetation-atmosphere interactions. *Engineering Geology* **139-140**, 1–16, doi:10.1016/j.enggeo.2012.04.003.
- Jamalinia, E., Vardon, P. J. & Steele-Dunne, S. C. (2019). The effect of soil-vegetation-atmosphere interaction on slope stability: a numerical study. *Environmental Geotechnics*, **Ahead of print**, doi:10.1680/jenge.18.00201.
- Plaxis BV (2018). PLAXIS Reference Manual 2018. *Technical report*, Delft, the Netherlands.
- Rahardjo, H., Satyanaga, A. & Leong, E. C. (2013). Effects of flux boundary conditions on pore-water pressure distribution in slope. *Engineering Geology* **165**, 133–142, doi:10.1016/j.enggeo.2012.03.017.
- Richards, L. A. (1931). Capillary conduction of liquids through porous mediums. *Journal of Applied Physics* **1**, No. 5, 318–333, doi:10.1063/1.1745010.

- Schapendonk, A. H. C. M., Stol, W., van Kraalingen, D. W. G. & Bouman, B. A. M. (1998). LINGRA, a sink/source model to simulate grassland productivity in Europe. *European Journal of Agronomy* **9**, No. 2-3, 87–100, doi:10.1016/s1161-0301(98)00027-6.
- Shibu, M. E., Leffelaar, P. A., van Keulen, H. & Aggarwal, P. K. (2010). LINTUL3, a simulation model for nitrogen-limited situations: Application to rice. *European Journal of Agronomy* **32**, No. 4, 255–271, doi:10.1016/j.eja.2010.01.003.
- Spitters, C. J. T. (1987). An analysis of variation in yield among potato cultivars in terms of light absorption, light utilization and dry matter partitioning. *Agrometeorology of the Potato Crop* **214**, doi:10.1016/j.eja.2010.01.003.
- TAW (Technical Advisory Committee for Flood Defence) (1996). Clay for Dikes. *Technical report*, The Road and Hydraulic Engineering Institute, Delft, the Netherlands.
- Tsiampousi, A., Zdravkovic, L. & Potts, D. M. (2016). Numerical study of the effect of soil–atmosphere interaction on the stability and serviceability of cut slopes in London clay. *Canadian Geotechnical Journal* **54**, No. 3, 405–418, doi:10.1139/cgj-2016-0319.
- van Genuchten, M. T. (1980). A Closed-form Equation for Predicting the Hydraulic Conductivity of Unsaturated Soils. *Soil Science Society of America Journal* **44**, No. 5, 892–898, doi:10.2136/sssaj1980.03615995004400050002x.
- van Laar, H. H., van Goudriaan, J. & van Keulen, H. (1997). SUCROS97: Simulation of crop growth for potential and water-limited production situations. as applied to spring wheat. *Quantitative Approaches in Systems Analysis* **14**, 892–898.
- Vardon, P. J. (2015). Climatic influence on geotechnical infrastructure: a review. *Environmental Geotechnics* **2**, No. 3, 166–174, doi:10.1680/envgeo.13.00055.
- Wolf, J. (2006). Grassland Data from PASK Study and Testing of LINGRA in CGMS. *Technical Report 2*, Asemares Project report No.2.



# 3

## THE IMPACT OF EVAPORATION INDUCED CRACKS AND PRECIPITATION ON TEMPORAL SLOPE STABILITY

*This chapter presents a numerical study of stability of dikes covered with grass, including both weather and drying driven cracking, building on the approach of Chapter 2. As before, an existing crop model is used to simulate vegetation growth and infiltration/evaporation in response to meteorological forcing. The model is modified to consider preferential flow due to cracking. An existing Finite Element Method (FEM) model is used to simulate the dike stability and hydro-mechanical behaviour, with the material properties modified to simulate the impact of cracks. The models are coupled together using an optimisation method to ensure mass balance and consistency. Results simulating a ten-year period indicate a strong impact of cracking on the factor of safety. The vegetation was found to be responsive to both crack presence and an increase in the amount of cracks. This suggests that monitoring vegetation could be a useful tool to identify cracked (dry) locations along dikes.*

### 3.1. INTRODUCTION

THE majority of secondary dikes have a vegetated surface which significantly affects the water infiltration and evaporation into and out of the dike (Vardon, 2015; Elia *et al.*, 2017). During extended periods of drought, significant water loss can occur which can significantly impact the mechanical stability of the dike. For example, peat levees that become dehydrated can shrink and lose a significant portion of their self-weight, a situation that can predispose them to instability (due to uplift or low shear strength due to low confining pressure) or overtopping and ultimately lead to a breach (CIRIA, 2013). Dikes which have other swelling and shrinking soils (soils which change in volume in response to a change in water content) will not lose as high a proportion of mass, but may suffer from cracking. The amount of volume change depends on the amount and type of clay minerals and water content change. In addition, as with all soils, the stress history affects the volume change behaviour. In dikes, shrinkage due to extreme drying may result in the occurrence of shrinkage cracks, which can weaken the soil structure and provide favorable conditions for rain infiltration. As a result, the overall shear strength of the soil and the factor of safety (FoS) of the slope can drop significantly (Zhang *et al.*, 2014). Additionally, rainfall infiltration into a dike body through surface fractures will occur faster and will increase the weight (and overturning forces) of the dike and reduce shear strength derived from soil suction. Assessing the impact of cracks on the infiltration at the soil surface and subsequent redistribution of water within the soil is important to characterise hydro-mechanical behaviour. Both processes are different compared to non-shrinking soil, for example, due to changes in surface runoff and preferential flow in the cracks (Cornelis *et al.*, 2006).

Most of the current hydro-mechanical models for slope stability analysis are based on the continuum modeling approach, as explicitly simulating the cracking process and preferential flow is difficult at a structure scale. However, some numerical analyses have been undertaken on a smaller scale to study details of the cracking process in soil, for example using the finite element method (FEM) (e.g., Shen, 2006; Trabelsi *et al.*, 2012; Sánchez *et al.*, 2014), the discrete element method (e.g., Péron *et al.*, 2009; Sima *et al.*, 2013) and the universal distinct element (e.g., Gui *et al.*, 2016). These studies focused on various aspects of the cracking, including the initiation, development and pattern of cracks, and the mechanical properties of the cracked soil (Li *et al.*, 2017).

In the previous chapter (Chapter 2), a crop growth model was used to simulate the growth of grass cover on a dike surface, and this was integrated with a FEM model to quantify the influence of vegetation on the FoS. It was shown in Chapter 2 that vegetation is strongly coupled to the moisture available in a dike, and particularly in the root zone. Meteorological aspects also govern this value, therefore a seasonal change is also seen. Some studies have highlighted the value of using the condition of the vegetation as an indicator of subsurface conditions. For instance, Hasan *et al.* (2013) concluded that grass growing in areas with cracks and fractures was stressed during winter and early spring due to a lack of moisture compared to grass in adjacent areas.

The FEM model used in this study is a fully coupled hydro-mechanical model. The crop model, utilises meteorological data (e.g. precipitation and radiation) to simulate the root zone water balance and vegetation growth. The two models are one way coupled together, i.e. the output of the crop model is used as an input into the FEM model. Other

models, e.g., [Sedighi et al. \(2018\)](#), include tightly coupled Thermo-Hydraulic surface boundary conditions and model in a tightly coupled manner, although they do not consider the effect of vegetation on the boundary fluxes. This current work follows the one-direction coupled approach.

One of the limitations of the simulation in the previous chapter was that it did not account for cracks. The objective of this chapter is to further develop the approach of Chapter 2 to account for both the development of cracks and their impact, i.e., preferential flow and the reduction in strength of the soil. As in the previous chapter, a crop model and a geotechnical model have been integrated together, resulting in a quantification of the Soil-Vegetation-Atmosphere (SVA) interaction and the temporal FoS. Both the crop model and geotechnical model have been modified to allow for consideration of cracks and cracking. A case study is then provided, with real atmospheric data and an idealised dike, to demonstrate the performance of the model.

## 3.2. METHOD

The idealised regional dike is used in this study is shown in Fig. 2.1. The description of the model and general workflow are described in detail in the previous chapter.

The modelling strategy and sub-models have been updated from Chapter 2, so that the crop model predicts when the root zone cracks, tracks the amount of cracks and calculates the drainage through both the cracks and the soil; the 1D geotechnical model is optimised based on total drainage from the crop model at different stages for each cracking event; and the soil shear strength is dependent on the amount of fractures in the root zone. It is assumed that cracking only occurs in the root zone with a constant thickness over the full depth of the root zone. The overview of this process is given in the flowchart in Fig 3.1.

The outputs from the model (shown in the flow chart) are: drainage from the root zone (from the crop model ( $D_L$ ) and 1D geotechnical model ( $D_P$ )); the leaf area index ( $LAI$ ): a measure of the amount of vegetation; crack area in the root zone ( $A_{crack}$ ), shown in a different color in Fig. 3.1 since it is a new output of the workflow rather than the one used in Chapter 2; boundary net flux ( $Q_{net}$ ) which is 'effective precipitation' minus evapotranspiration (explained in Chapter 2); displacement and FoS which are outputs from the 2D geotechnical model. The workflow of integrating these two models is controlled via Python. In the following sections the updates for simulating cracks in both the crop model and the geotechnical model are described.

### 3.2.1. CROP MODEL

The crop model LINGRA ([Schapendonk et al., 1998](#)) is used to solve the water balance in the root zone of a grass cover. In this chapter, LINGRA has been adapted to incorporate the development of cracks and the impact of cracks in the water balance in the root zone, and consequentially the leaf growth.

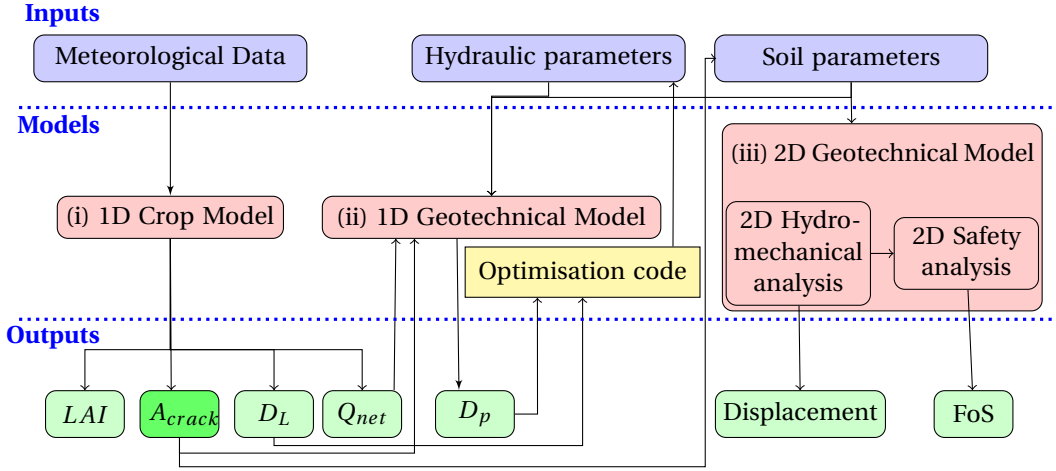


Figure 3.1: Flow chart of the numerical modelling procedure, modified from Chapter 2 to include the effect of shrinkage behaviour. The only added output parameter compared to the workflow shown in Fig. 2.2 is crack area ( $A_{crack}$ ), shown in a different color.

### SIMULATING CRACK DEVELOPMENT IN THE CROP MODEL

It is assumed that the cracking occurs in the upper layers of the soil, and therefore the soil is under very low confining pressure and any potential volume loss results in either cracking or subsidence, rather than volume expansion of the soil matrix, which would cause tension. This assumption is not valid at greater soil depths and therefore is limited to the root zone. Also, it is assumed here that there are no initial cracks or macropores due to worm and root holes.

The intact soil is considered to be composed of solid material and pores (see Fig. 3.2). As a soil shrinks, the solid particles stay the same size, move and rearrange so that the void space is reduced and the soil shrinks (Fig. 3.2(a)). Soil shrinkage can occur in both the vertical and horizontal direction. Vertical shrinkage generally causes soil surface subsidence and horizontal shrinkage results in cracks, as shown in the right hand side image of Fig. 3.2(a).

The volume fractions are shown in Fig. 3.2(b). In an intact soil, the total volume is made up of pores and solids. When a soil shrinks due to moisture loss (see Fig. 3.2(b) right hand side), the solid volume fraction ( $V_{solid}$ ) remains the same in reference to the original volume and a portion of the pores reduces in volume, i.e. shrinks. Note, that it would also be possible to consider volume fractions in respect to the soil matrix, or the original volume soil matrix including the fractures and subsidence. The crack volume fraction with respect to the original volume is calculated from overall and vertical shrinkage as:

$$V_{crack} = V_{shrinkage} - V_{subsidence} \tag{3.1}$$

where  $V_{shrinkage}$ ,  $V_{crack}$  and  $V_{subsidence}$  (all in  $m^3 m^{-3}$ ) are the volume fraction of overall matrix shrinkage, the crack volume fraction and the subsidence volume fraction respectively, as shown in Fig. 3.2(b).

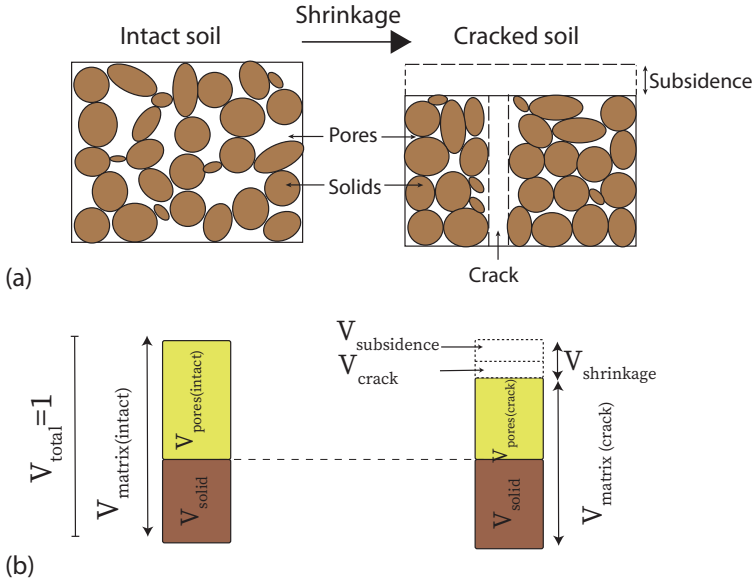


Figure 3.2: Soil matrix components before (intact soil) and after (cracked soil) shrinkage.  $V_{shrinkage}$  includes both  $V_{subsidence}$  and  $V_{crack}$ .

It is also useful to calculate the volume fraction of the cracks in reference to the soil matrix and cracks volume, as this is also equal to the area fraction of fractures on the surface of the dike and therefore can be used to calculate flow through the fractures. This can be calculated as:

$$V_{crack,new} = A_{crack} = \frac{V_{shrinkage} - V_{subsidence}}{1 - V_{subsidence}} \quad (3.2)$$

The relation between the proportion of soil shrinkage that results in cracking and subsidence can be governed via:

$$V_{subsidence} = 1 - (1 - V_{shrinkage})^{(1/r_s)} \quad (3.3)$$

where  $r_s$  is a dimensionless geometry factor which determines the partition of total volume change over change in layer thickness and change in crack volume (Bronswijk, 1988). For isotropic three-dimensional shrinkage,  $r_s = 3$ ; and in the case of subsidence only,  $r_s = 1$ . If cracking dominates subsidence, then  $r_s > 3$ , and if subsidence dominates cracking  $1 < r_s < 3$ .

The shrinkage volume fraction,  $V_{shrinkage}$ , is equal to the fraction loss of the pore volume, which can also be calculated from the void ratio ( $e = V_{pores}/V_{solid}$ ) and the volumetric water content at saturation:

$$V_{shrinkage} = \Delta V_{pores} = \Delta e V_{solid} \quad (3.4)$$



### SHRINKAGE CURVE

The matrix shrinkage is a function of volumetric moisture content and material shrinkage behaviour. A shrinkage curve or shrinkage characteristic curve describes the relationship between soil volume and soil moisture content (Cornelis *et al.*, 2006). Initially, a very loose saturated soil may shrink and remain almost fully saturated. As the amount of water in the soil reduces, the soil will typically shrink less in proportion to the amount of water reduction, resulting in de-saturation.

Starting from a completely saturated shrinking soil and following a drying path, Bronswijk (1991) distinguished these four stages: (1) structural shrinkage; (2) normal shrinkage; (3) residual shrinkage, and (4) zero shrinkage. According to Bronswijk (1991), the first stage only happens in well-structured soils, when the macropores empty without noticeable change in aggregate volume, and air enters the macropores.

Many forms of shrinkage curve exist. A convenient one relates the void ratio to the moisture ratio ( $\mu = V_{water}/V_{solid}$ ), i.e. both the amount of water and voids are related to the solid soil volume as a reference. The moisture ratio can also be calculated from the more well recognised volumetric moisture content ( $\theta = V_{water}/V_{soil}$ ), by dividing by  $(1 + e)$ .

In this work, the approach for the shrinkage curve of Kim *et al.* (1992) and Kroes *et al.* (2017) is followed:

$$e = e_0 \times \exp(-\beta_K \mu) + \gamma_K \mu, \quad \text{for } 0 < \mu < \mu_{sat} \quad (3.5)$$

where  $e_0$  is the void ratio at  $\mu = 0$ ,  $\beta_K$  and  $\gamma_K$  are dimensionless fitting parameters and  $\mu_{sat}$  is the moisture ratio at saturation.

It is assumed that cracking occurs when the soil shrinks and it does not recover or seal. Therefore, the shrinkage curve is only used for drying, and the void ratio is only updated when the moisture ratio is lower than that which the soil has previously experienced.

### WATER BALANCE IN CRACKED MATRIX

LINGRA uses a tipping bucket approach to solve water balance in the root zone (Schapendonk *et al.*, 1998). Hence, ponding in the cracks is disregarded. A fraction of precipitation infiltrates into the crack matrix ( $I_{P,crack}$ ) and goes directly to the lower layers, and the rest infiltrates into the soil matrix ( $I_{P,matrix}$ ) or runs off, if the flow capacity is exceeded. The daily changes in the amount of water stored in the soil (matrix) is therefore:

$$\Delta W A_{matrix} = I_{P,matrix} - In - ET_{matrix} - D_{matrix} - Rn_{matrix} \quad (3.6)$$

where  $In$  is leaf interception,  $ET_{matrix}$  is the evapotranspiration,  $D_{matrix}$  is the drainage rate and  $Rn_{matrix}$  is the runoff, all from the soil matrix. All quantities are in  $m \text{ day}^{-1}$  (due to the model being 1D). These are quantified using the approach of LINGRA (Schapendonk *et al.*, 1998).

The proportion flowing into the cracks is assumed to be equal to the surface area of the cracks, which in turn is equal to the volume fracture, as the cracks are assumed to be only vertical. Horizontal flow and evaporation from the macropores are disregarded and only infiltration and drainage are considered. The crack infiltration,  $I_{P,crack}$  ( $m \text{ day}^{-1}$ ), and the soil matrix infiltration,  $I_{P,matrix}$  ( $m \text{ day}^{-1}$ ) are:

$$I_{P,crack} = A_{crack} \times P \quad , \quad I_{P,matrix} = A_{matrix} \times P \quad (3.7)$$

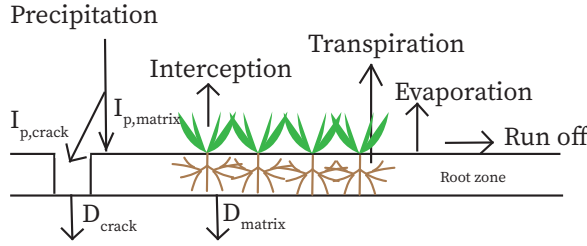


Figure 3.3: Updated root zone water balance modified from [Jamalinia et al. \(2019\)](#) for cracked soil matrix to include water flux in cracks.

where  $A_{matrix}$  is the surface area of the soil which is equal to  $1 - A_{crack}$ .

When the amount of water in the soil matrix reaches the field capacity ( $\theta_{fc}$ ), the excess water drains from the lower boundary of the root zone. The total amount of drainage ( $D_L$ ) to the layer below the root zone, as shown in Fig. 3.3, includes drainage from both the soil matrix ( $D_{matrix}$ ) and cracks ( $D_{crack}$ ), calculated as:

$$D_L = D_{crack} + D_{matrix} = (A_{crack} \times P) + D_{matrix} \quad (3.8)$$

Due to cracking, the field capacity changes. Here, as the computational domain remains the same size, the field capacity relates to the total (original) volume. The field capacity for the cracked soil matrix ( $\theta_{fc(matrix)}$ ) is calculated assuming that the degree of saturation ( $Sr = V_{water} / V_{pores}$ ) at field capacity for the soil matrix (Fig.3.2) remains constant in the intact and cracked soil:

$$Sr_{intact} = Sr_{matrix} \quad (3.9)$$

where  $Sr_{intact}$  and  $Sr_{matrix}$  are the degree of saturation in the intact and cracked soil, respectively. The field capacity is related to the degree of saturation by:

$$\theta_{fc} = \frac{Sr_{fc} \times V_{pores}}{V_{total}} \quad (3.10)$$

and therefore,

$$\begin{aligned} \theta_{fc(cracked)} &= \theta_{fc(intact)} \frac{V_{pores(cracked)}}{V_{pores(intact)}} \\ &= \theta_{fc(intact)} \frac{V_{pores(intact)} - V_{shrinkage}}{V_{pores(intact)}} \\ &= \theta_{fc(intact)} \frac{\theta_{sat(intact)} - V_{shrinkage}}{\theta_{sat(intact)}} \end{aligned} \quad (3.11)$$

where the subscripts (*intact*) and (*cracked*) related to the intact and cracked soil, respectively.

### 3.2.2. GEOTECHNICAL MODEL

The commercial finite element code, PLAXIS 2D, was used in this study. The workflow is controlled via the PLAXIS Python interface. Further information on hydro-mechanical and safety analysis of this model can be found in Chapter 2 and [Plaxis BV \(2018\)](#).

Cracks, in addition to providing preferential flow channels which increase the soil permeability, also decrease the soil strength ([Wang et al., 2011](#)). Furthermore, cracks can form a part of the critical surface and therefore can ultimately influence the stability. In this chapter, the impact of cracks is considered on the boundary net flux, hydraulic parameters and as a bulk effect via a change in the shear strength parameters. This allows for a relatively simple method of quantifying the impact of cracks, without predicting complex crack patterns, orientations or very local changes in the critical failure surface. Moreover, cracks are considered to only extend over the root zone. The calculated crack volume from the crop model is used in this geotechnical model to update the mechanical strength of the cracked root zone. The shear strength parameters, cohesion ( $c'$ ) and friction angle ( $\phi'$ ) have been reduced according to the crack volume, using as a first approximation, a linear relationship. The values of  $c'$  and  $\phi'$  for an intact soil and the minimum value of  $c'$  and  $\phi'$  for a maximum  $V_{crack}$  are input by the user.

### 3.2.3. CASE STUDY

The example dike, shown in Fig. 2.1, has been investigated. The numerical experiment was performed for ten years with climatic data, from 2009 to 2019, used to obtain a time series of FoS to investigate the influence of meteorological conditions on the soil shrinkage and cracking behaviour and, consequently, the dike safety. Furthermore, the impact of cracking on vegetation growth was investigated.

#### INPUT DATA

The meteorological data were obtained from the The Royal Netherlands Meteorological Institute (KNMI) station at Schiphol Airport (Amsterdam) (52° 19' 04" 47' OL), the same location used in Chapter 2. In Figs. 3.4(a)-(d) precipitation, average air temperature, wind speed and solar radiation for the 10 years simulation period is shown. These data are used as inputs for the crop model.

The key material parameters used by the crop model for both the soil and vegetation are listed in Table 2.1. The soil and vegetation parameters are equal to those chosen in Chapter 2. Additionally, parameters for the shrinkage curve (Eq. 3.5) are needed and were obtained from literature ([van Dam, 2000](#); [Kroes et al., 2017](#)):  $\beta_K = -1.11$ ,  $\gamma_K = -0.91$  and  $e_0 = 0.4$ . In Fig. 3.5 the calculated shrinkage curve for this study is shown by the solid blue line; the two dashed lines are selected measured shrinkage characteristics of clay and peaty soils in the Netherlands, as described by [Bronswijk & Evers-Vermeer \(1990\)](#) and [Hendriks \(2004\)](#), respectively; and the dotted green line is the saturated line. In this study, the isotropic shrinkage has been considered, so  $r_s = 3$ .

As shown in Fig. 2.1 the example dike consists of the root zone and the soil of the dike body. Constitutive and hydraulic input parameters for those parts of the dike are listed in Table 3.1 for the intact soil matrix. The values are based on the default soil properties from the PLAXIS library for the root zone (silt clay) and for the dike body (organic clay), except for the hydraulic values of the root zone which are obtained from the optimisation

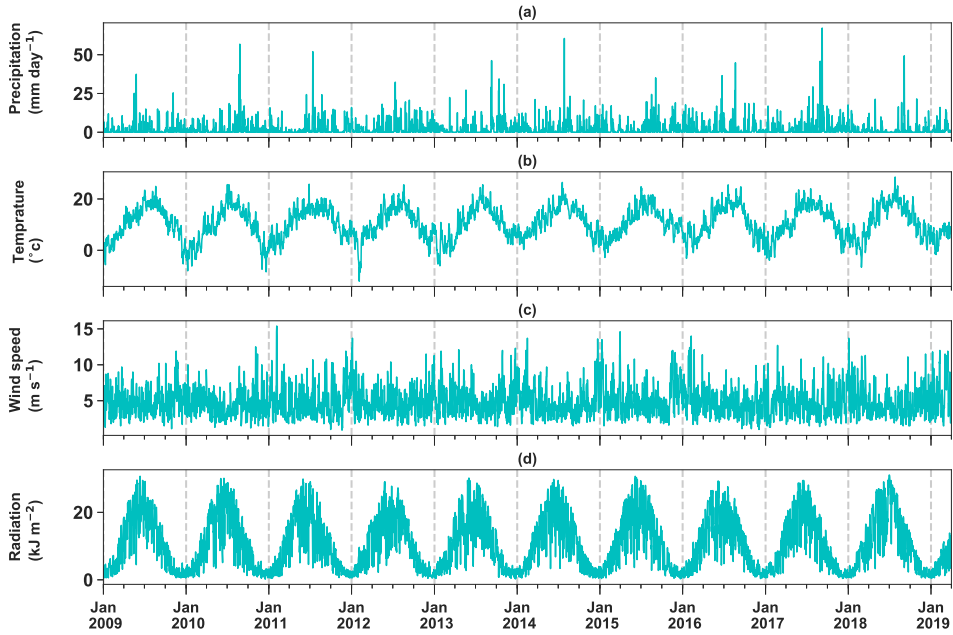


Figure 3.4: Daily values of inputs for the crop model from 2009 to 2019 (a) Precipitation; (b) Average temperature; (c) Average wind speed; (d) Radiation.

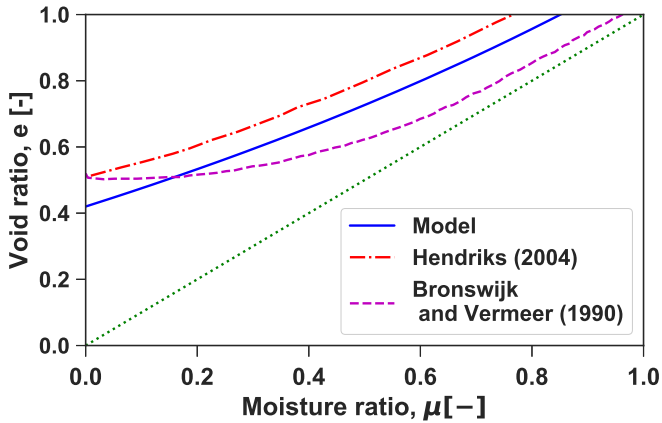


Figure 3.5: Shrinkage curve used for this study for the root zone compared with the measured shrinkage characteristics for dutch clay (Bronswijk & Evers-Vermeer, 1990) and peaty clay (Hendriks, 2004) soil.

Table 3.1: Input parameters used for intact soil in the geotechnical model.

Parameter	Root zone	Dike body
<b>Constitutive model (Mohr-Coulomb)</b>		
Saturated unit weight ( $\gamma_{sat}$ )	20 (kN m <sup>-3</sup> )	12 (kN m <sup>-3</sup> )
Intact friction angle ( $\phi'_{intact}$ )	23°	23°
Minimum friction angle ( $\phi'_{min}$ )	4.5°	-
Intact cohesion ( $c'_{intact}$ )	2 (kPa)	2 (kPa)
Minimum cohesion ( $c'_{min}$ )	0.6 (kPa)	-
Dilatancy angle ( $\psi$ )	0°	0°
Young's modulus ( $E'$ )	10 (MPa)	20 (MPa)
Poisson's ratio ( $\nu'$ )	0.3	0.2
Initial void ratio ( $e_{intact}$ )	0.67	1.2
<b>Hydraulic model (van Genuchten) for intact soil</b>		
Hydraulic conductivity ( $k_{sat}$ )	0.14 (m day <sup>-1</sup> )	0.03 (m day <sup>-1</sup> )
Scale parameter $\alpha$	1.47 (m <sup>-1</sup> )	1.38 (m <sup>-1</sup> )
Fitting parameter $n$	1.97	1.32
Fitting parameter $m$	0.87	1.24

code. The initial parameters optimised for intact soil are shown here. Since the cracking occurs only in the root zone, the dike body parameters do not change as  $A_{crack}$  increases. The shear strength parameters ( $c$  and  $\phi$ ) and the hydraulic parameters change for the root zone as cracks grow. To decide on a minimum value for shear strength parameters, the crop model was first run without the geotechnical model, and the maximum crack area ( $A_{crack,max}$ ) was extracted (10%). Then shear strength values were picked to ensure that the model had a FoS > 1, so that it would continue to run. The value of shear strength parameters were selected for demonstration purposes and for more realistic analyses they should be calibrated for real cases.

### 3.3. RESULTS AND DISCUSSION

In Fig. 3.6, temporal results from the crop model for soil which is able to crack are compared with soil which cannot crack, i.e. the model presented in Chapter 2. As shown in Fig. 3.6(a), the cracks cannot seal during wet periods, but only increase in conditions drier than previously encountered. This assumption ensures that the worst-case scenario has been considered. In Fig. 3.6(a) the crack area increases from spring 2009 and gradually increases from 0 to 6% by May. Wet days from May - August 2009 ensure that the crack amount remains constant until the next dry period in June - July 2010 during which cracks increase to 7.5%. During summer 2011, cracks grow again (9.3%) and the soil experiences the next drier condition in the summer 2018, when cracks again grow (10%). As the crack expands only in drier conditions than have been previously encountered, the time between cracking events gets longer as the analysis progresses.

In Fig. 3.6(b), temporal variations in  $LAI$  are shown. The  $LAI$  is highest in spring and summer, since reduced solar radiation limits growth in the autumn and winter. Higher  $LAI$  values in the summer lead to higher evapotranspiration, and hence a reduction in

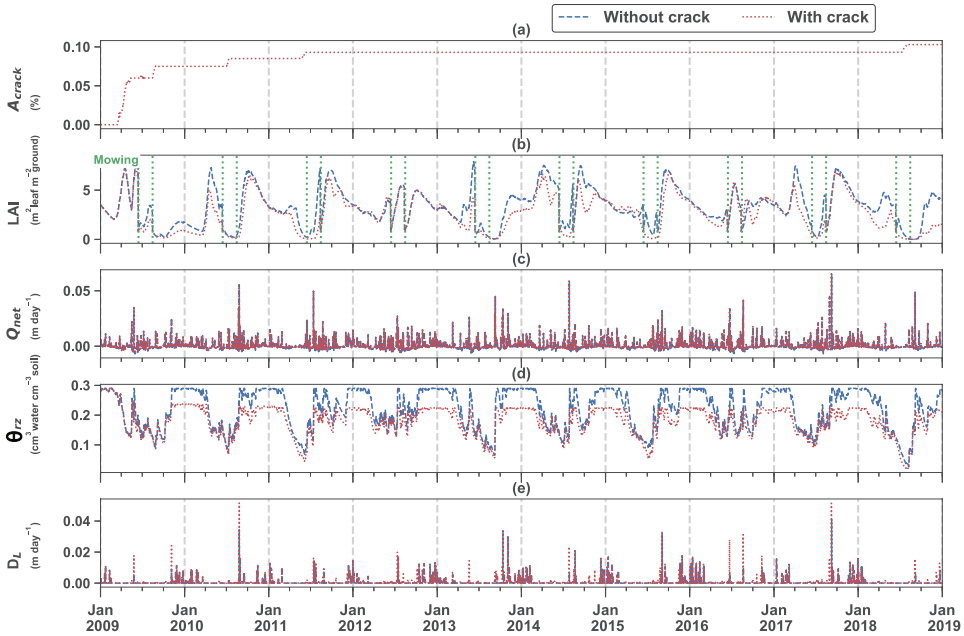


Figure 3.6: Daily values of crop model outputs from 2009 to 2019 for the case without cracks and with cracks in the root zone area (a) Crack area; (b) Leaf Area Index ( $LAI$ ); (c) Boundary net flux ( $Q_{net}$ ); (d) Root zone water content ( $\theta_{rz}$ ); (e) Drainage from root zone to lower layers ( $D_L$ ).

the amount of water flux into the dike (Fig. 3.6(c)). The mowing events on 15 June and 15 August were imposed in the crop model based on the mowing schedule for regional dikes in the Netherlands (see Chapter 2), which can be seen by the sudden decrease in  $LAI$ . The vegetation growth can be seen to be influenced by the presence of cracks, due to a portion of the precipitation draining directly to the lower soil layer and a reduction in the maximum stored water (seen in Fig. 3.6(d)). In the case of a cracked soil, the  $LAI$  is lower or equal at almost all times than the case without cracks.

Positive  $Q_{net}$  values occur in wet periods when precipitation exceeds evapotranspiration demand. When there are cracks, the boundary net flux ( $Q_{net}$ ) is seen to be higher than for the non-cracked soil (Fig. 3.6(c)). In the cracked soil, the combined effect of drier root zone and lower  $LAI$  cause lower evapotranspiration and leaf interception.

In Fig. 3.6(d) it is shown that the water content in the root zone ( $\theta_{rz}$ ) decreases during the summer due to high levels of evapotranspiration. On the other hand, during wet periods with a consistently high  $Q_{net}$ , the root zone reaches the field capacity, and extra water drains to the lower layer. In the cracked matrix,  $\theta_{rz}$  is lower as some rainfall passes directly through the cracks and does not enter the soil root zone. Additionally, the field capacity is reduced, therefore the maximum amount of water stored is reduced. In summer 2010, the crack area increases due to the dry period which influences the vegetation growth, i.e. after first mowing in June 2010, due to the very low water content in the root zone (Fig. 3.6(d)), vegetation cannot recover in the growing season. The same

Table 3.2: Evolution of the hydraulic parameters with crack area used in the geotechnical model.

$A_{crack}$ (%)	Hydraulic parameters (van Genuchten model)			
	$k_{sat}$ (m day <sup>-1</sup> )	$a$ (m <sup>-1</sup> )	$n$ (-)	$m$ (-)
10	0.316	3.55	2.49	0.96
9.3	0.31	3.47	2.48	0.95
8.5	0.30	2.15	1.92	0.90
7.5	0.26	2.08	2.01	0.86
6	0.18	2.05	1.82	0.84
< 6	0.15	1.47	1.97	0.87

situation happens in May - June 2011 and June - August 2018, when the average  $LAI$  is very low over almost 3 months in both cracked and non-cracked cases.

Drainage ( $D_L$ ) occurs when there is a positive (downward)  $Q_{net}$  and  $\theta_{rz}$  reaches the field capacity (Fig. 3.6(e)). This can generally be seen in the winter months. For example, spikes in  $D_L$  in August 2010 and 2017 correspond to the heavy rainfall and therefore high  $Q_{net}$ . Infiltration of precipitation through cracks and the reduction in the field capacity in cracked soil, which both increase with  $A_{crack}$  rising, causes  $D_L$  to increase.

The results of the optimisation procedure for the hydraulic parameters of the geotechnical model are shown in Table 3.2. For each new crack area, the optimisation procedure repeated. It is seen that, in general, as the crack area increases, the hydraulic conductivity increases. In addition, different soil water retention curves (SWRC) for each crack area have been plotted based on the hydraulic model values. These are shown in Fig. 3.7, in which  $S_r$  is the degree of saturation, and  $h$  is the suction height above the phreatic level. In general, more cracks are associated with a drier root zone.

In Fig. 3.8 the geotechnical model outputs are illustrated. Fig. 3.8(a) shows the crack percentage (from the crop model) for convenience. Fig. 3.8(b) and (c) show the pore water pressure (pwp) at points A (in the root zone) and B (in the dike body), shown in Fig. 2.1, respectively. Positive values are for compressive pressures and negative values indicate suction. As expected, high levels of drainage (August 2010 and 2017), or long periods of cumulative drainage (winter 2009 - 2010), lead to higher pwp in the root zone and dike body. In both locations (A and B) pwp is higher in case of cracked soil as more water reaches the soil system via the higher  $Q_{net}$  and more  $D_L$  in the cracked soil. As  $A_{crack}$  increases, pwp rises and decreases more slowly.

In Figs. 3.8(d) and (e) the magnitude of total displacement of points A and B is shown. The displacement rises following large  $Q_{net}$  and recovers between precipitation events. A slight accumulation of displacement over time is observed, due to plastic displacement. The displacement of the points increase as crack grows during time, which depicts the effect of shrinkage behaviour in the root zone (where cracks exist) and more drainage into the dike body. By increasing the crack area the difference in displacement between the crack and non-crack condition gets more noticeable.

The temporal variation of FoS is shown in Fig. 3.8(f) from 2009 to 2019. Safety in the

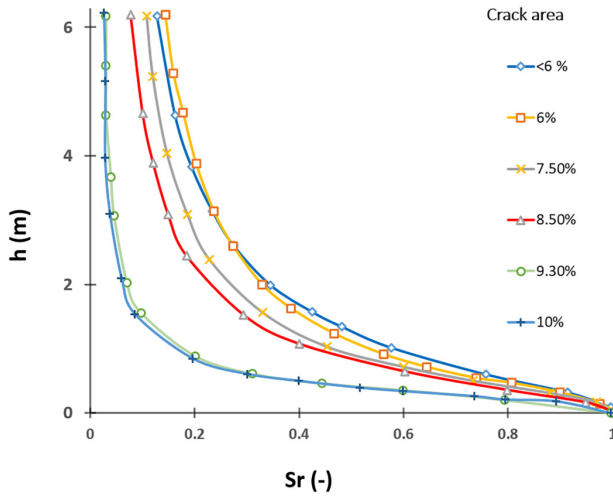


Figure 3.7: Variation of soil water retention curve for the root zone for different crack area.

dike is responsive to the climate and vegetation condition. The safety of the dike in the cracked condition is significantly lower than the case without cracks under the combined effect of more infiltration into the dike (Fig. 3.6(e)) and lower shear strength induced by modified cohesion and friction angle. The maximum crack area leads to the minimum shear strength parameters (Table. 3.2), thereby generally lower FoS. During the simulated period, results from Figs. 3.6 and 3.8 suggest that more cracks lead to a lower amount of vegetation ( $LAI$  decreases) and a lower amount of stored water in the root zone. In general, this leads to lower safety in the dike. As seen in the results, heavy rainfall events cause a dramatic decrease in the safety. Therefore, it is the combination of cracking, due to drought, which reduces the strength and general level of safety, and heavy rainfall events, which significantly lower the safety temporarily.

### 3.4. USING VEGETATION AS AN INDICATOR FOR DIKE HEALTH

In the current chapter, it is shown that vegetation responds to the presence of cracks, which influences the available water in the root zone and therefore makes more cracking likely.

Consistent with visual observations from dike inspectors in the Netherlands, in summer 2018 the water content in the root zone was extremely low and the  $LAI$  was low for an extended period of time (Figs. 3.6(b) and (d)). Visually it was seen that a substantial amount of the grass cover died and took several months to recover, this is shown in the simulation (Fig. 3.6(b)). In the analysis, it was also shown that  $A_{crack}$  increased in August 2018, Fig. 3.6(a), after about 7 years of no increase. This summer was the warmest summer during the simulation period. After the mowing events in 2018, the vegetation is seen to be able to partially recover in the simulations without cracks, whereas it cannot in the



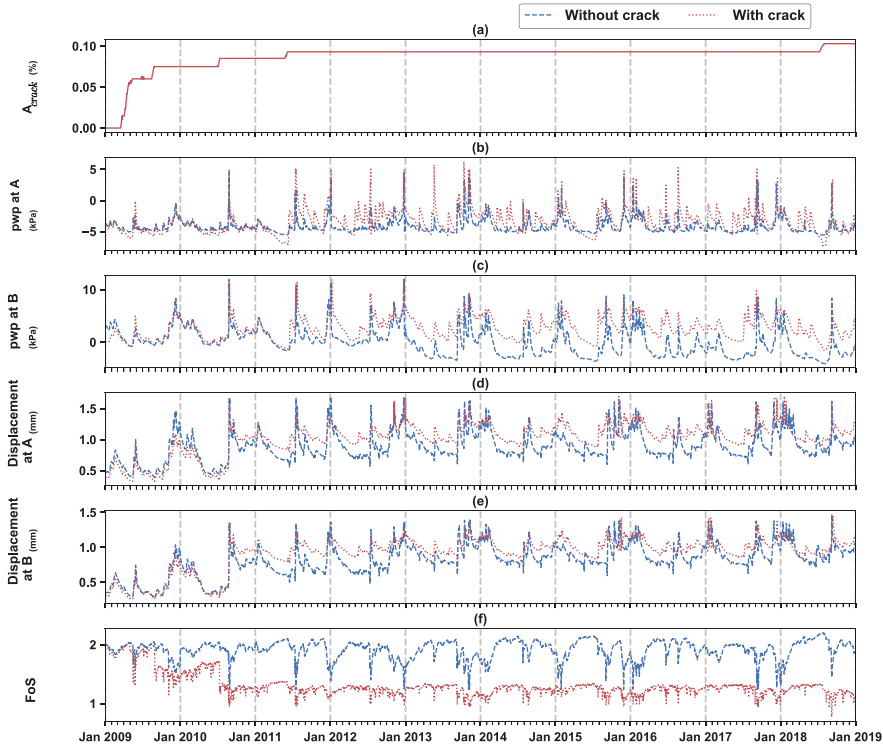


Figure 3.8: Daily values of outputs from 2009 to 2019 for the case without cracks and with cracks in the root zone area (a) Crack area; (b) and (c) Pore water pressure (pwp) in points A (in the root zone) and B (in the dike body); (d) and (e) Absolute value of displacement in points A and B; (f) Factor of Safety.

cracked root zone (Fig. 3.6(b)). Therefore, it is proposed that vegetation indices (e.g. *LAI*) could be used as an indicator of crack presence, also indicated by Hasan *et al.* (2013).

The cumulative precipitation, root zone saturation and *LAI* for 2017 and 2018 for the cracked soil are plotted in Figs. 3.9(a)-(c), respectively. The former year considered as a ‘wet’ year and the latter one is the driest year in the 10-year simulation. Before the first mowing, the amount of precipitation and consequentially the available water in the root zone was similar. However, in the summer, growing season, the precipitation in 2018 was less than 2017 which led to a dry condition and consequently the crack volume grew in July 2018 (red line in Fig. 3.9). The difference in vegetation growth is significant and seen by the difference between *LAI* in the following months. In first days of September, the rainfall event for both years is almost the same and in both case the water content reaches the field capacity in the root zone (Fig. 3.9(b)), but due to the larger crack area in 2018, the vegetation cannot recover as much as in September 2017. This indicates that the *LAI* could also be used directly to identify cracked dikes which need maintenance. However, this does not seem to occur consistently throughout all years (see Fig. 3.6).

To further investigate the use of vegetation as an indicator in more detail, two differential *LAI* values are shown in Fig. 3.10. The first differential, i.e. the velocity or growth rate,

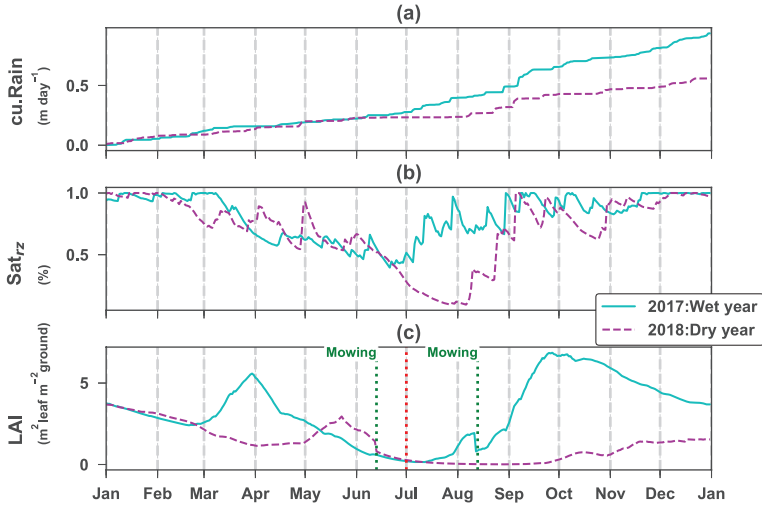


Figure 3.9: Comparison between a wet year (2017) and a dry year (2018): (a) cumulative precipitation, (b) root zone saturation, (c) leaf area index. Mowing times in both years and crack propagation in summer 2018 is shown by dotted green line and red line, respectively.

is  $diff[LAI] = LAI_t - LAI_{t-x}$  (the value is not divided by the time window), where  $t$  is the current day and  $x$  is the time window (Fig. 3.10(a)). The absolute of the second differential, i.e. the absolute value of vegetation growth acceleration or rate of change of growth rate (again, note that the value is not divided by the time window), with a time window of 15 days, is shown in Fig. 3.10(b). Initially, when there is no or very limited crack area, the first and second differential  $LAI$  values ( $diff[LAI]$  and  $accel.[LAI]$ ) are identical for the cracked and non-cracked cases. As the crack area increases over time, the differential  $LAI$  time series (Fig. 3.10) can be categorized into periods where: (1) the two lines are virtually indistinguishable; (2) the cracked simulation exhibits a lower acceleration; or (3) the cracked simulation exhibits more variability in both cases of velocity and acceleration growth. These categories occur at different times of year and under different degrees of water stress, as highlighted in Fig. 3.10, for example:

1. Time series of  $LAI$ ,  $diff[LAI]$  and  $accel.[LAI]$  are virtually indistinguishable (highlighted in blue in Fig. 3.10) in the following periods: January - August 2009, January - April 2010, January 2012 - January 2013, January - August 2016. This is observed to be when either the crack area is starting to grow (January - August 2009) or there is a moderate amount of  $LAI$  and the root zone water content is reasonably high. In particular, in the whole year 2012 and the June - July 2016, the water content of the root zone remained higher than other years, and it is high enough for the vegetation to grow even over cracked areas.
2. Lower variability in the  $diff[LAI]$  (lower  $accel.[LAI]$ ) from the cracked simulation results (highlighted in green in Fig. 3.10) occurs within the following periods: April - August 2011, June - October 2013, July - September 2015, June - September 2017,

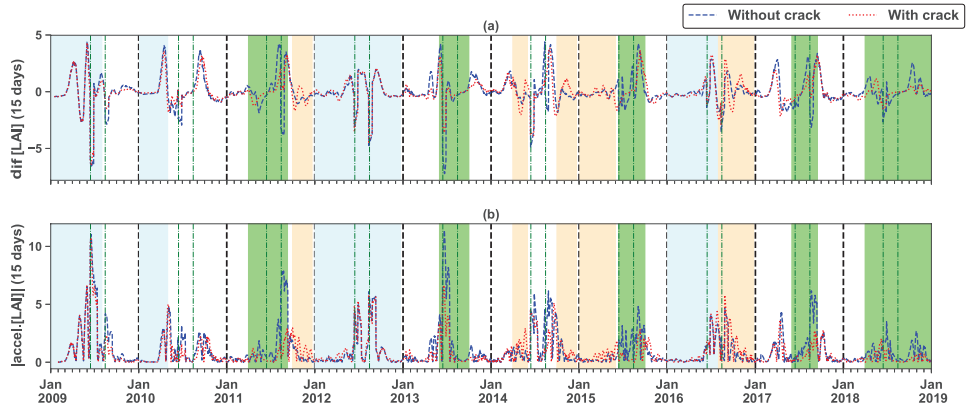


Figure 3.10: LAI (a) growth rate ( $diff[LAI]$ ) and (b) acceleration growth, with a time window of 15 days from 2009-2019.

April 2018 - January 2019. These are seen to be in situations with a low water content in the root zone, and low values of LAI, which implies dry periods. In particular, between mowing times, there seems to be significant differences between cracked and non-cracked simulation results in dry years (2011, 2014, 2015, 2018). In dry periods, less water is available in the root zone in the cracked area than in the non-cracked area (Fig. 3.6(d)). Therefore, vegetation cannot regrow after mowing over the cracked area as much as it regrows over the healthy areas. This low variability mainly occurs in the summer, and depending on the extent of the drought extends through the following year. However, this does not happen in the wet years (2012, 2013, 2016) as explained in the previous paragraph.

- Higher variability in the  $diff[LAI]$  (higher  $|accel.[LAI]|$ ) from the cracked simulation results (highlighted in orange in Fig. 3.10) usually happens in the following periods: September - December 2011, April - June 2014, October 2014 - June 2015, August 2016 - January 2017. At the times there is generally a moderate amount of LAI and the root zone water content is relatively quickly increasing or decreasing due to heavy rainfall after a dry period and couple of days in a row with the negative  $Q_{net}$ , respectively (Fig. 3.6(c)). This is generally observed in the spring and autumn periods, when the energy for vegetation growth is limited and LAI variation is mainly responsive to the  $SM_{rz}$  variation.

This suggests that monitoring to investigate the dike should be timed accordingly. In periods of moderate LAI and precipitation (generally winter), almost no differences are likely to be observed. In the summer periods there are more significant differences in dry years and in the spring and autumn much more variability is seen in the cracked soils in almost all years. Therefore, monitoring prior to the summer (when more cracks may occur) or prior to the winter (when the lowest safety is seen) is advisable.

Results in Figs. 3.9-3.10, support the argument that vegetation could be used as an indicator to distinguish whether a dike is significantly cracked. By observing anomalies

in vegetation, further more targeted investigation can be planned. In addition, results suggest that displacement can be used as an indicator for both saturation (short term changes) and for accumulation of cracks (long term changes), although long term changes may also indicate subsidence or other processes. Displacement and vegetation indices can be obtained from Earth observation data. Interferometric Synthetic Aperture Radar (InSAR) (Hanssen, 2001; Ferretti *et al.*, 2001) is a technique that maps millimeter-scale deformations of the Earth's surface from satellite images. Vegetation indices can be measured from both optical and radar images with fine resolution provided by satellites (Colombo *et al.*, 2003; Hasan *et al.*, 2013, e.g.), this will be discussed in detail in Chapter 5. While no absolute value of vegetation indices can be predictive of cracking, anomaly detection identify vulnerable areas that warrant further investigation.

### 3.5. CONCLUSION

The integrated model framework composed of a crop model and a geotechnical model including the impact of cracking was used to illustrate the sensitivity of the factor of safety to root zone soil moisture and vegetation cover in an idealised dike. The simulation in this chapter extended a method in the previous chapter to include the effects of cracking. In this chapter, simple modifications or parameterisation was included in both sub-models to account for the formation of cracks. This provides a means to account for the preferential flow into the dike that is associated with cracks in the cover layer and a reduction in shear strength. This represents a step forward to understand soil-vegetation-atmosphere interactions in grass-covered dikes. Simulations with the new integrated model were used to compare vegetation growth and safety under intact and cracked soil conditions. In this chapter the impact of the presence of cracks on the water flux into the dike and the shear strength is investigated, and both of them affect the Factor of Safety (FoS). The history of the precipitation, root zone water content and *LAI* have an impact on crack propagation. Therefore, vegetation condition (Leaf area index or comparable indicator) and root zone water content could be useful as indicators to detect cracked areas along a dike and also of increasing crack volume at an early stage. Results suggest that monitoring in the spring or autumn may provide the most reliable and useful results, since in these months much more variability in rate of vegetation growth over the cracked soils is predicted.

## REFERENCES

- Bronswijk, J. (1988). Modeling of water balance, cracking and subsidence of clay soils. *Journal of Hydrology* **97**, No. 3, 199–212, doi:10.1016/0022-1694(88)90115-1.
- Bronswijk, J. J. B. (1991). Relation between vertical soil movements and water-content changes in cracking clays. *Soil Science Society of America Journal* **55**, No. 5, 1220–1226, doi:10.2136/sssaj1991.03615995005500050004x.
- Bronswijk, J. J. B. & Evers-Vermeer, J. J. (1990). Shrinkage of dutch clay soil aggregates. *Netherlands Journal of Agricultural Science* **38**, No. 2, 175–194.
- CIRIA (2013). *The International Levee Handbook*. London, UK: CIRIA (Construction Industry Research and Information Association), MEDE (Ministère de l'Ecologie du Développement durable et de l'Energie) and USACE (US Army Corps of Engineers).
- Colombo, R., Bellingeri, D., Fasolini, D. & Marino, C. M. (2003). Retrieval of leaf area index in different vegetation types using high resolution satellite data. *Remote Sensing of Environment* **86**, No. 1, 120–131, doi:10.1016/S0034-4257(03)00094-4.
- Cornelis, W., Corluy, J., Medina, H., Diaz, J., Hartmann, R., van Meirvenne, M. & Ruiz, M. (2006). Measuring and modelling the soil shrinkage characteristic curve. *Geoderma* **137**, No. 1, 179–191, doi:10.1016/j.geoderma.2006.08.022.
- Elia, G., Cotecchia, F., Pedone, G., Vaunat, J., Vardon, P. J., Pereira, C., Springman, S. M., Rouainia, M., Van Esch, J., Koda, E., Josifovski, J., Nocilla, A., Askarinejad, A., Stirling, R., Helm, P., Lollino, P. & Osinski, P. (2017). Numerical modelling of slope–vegetation–atmosphere interaction: an overview. *Quarterly Journal of Engineering Geology and Hydrogeology* **50**, No. 3, 249–270, doi:10.1144/qjgegh2016-079.
- Ferretti, A., Prati, C. & Rocca, F. (2001). Permanent scatterers in SAR interferometry. *IEEE Transactions on Geoscience and Remote Sensing* **39**, No. 1, 8–20, doi:10.1109/36.898661.
- Gui, Y., Zhao, Z., Kodikara, J., Bui, H. H. & Yang, S. (2016). Numerical modelling of laboratory soil desiccation cracking using UDEC with a mix-mode cohesive fracture model. *Engineering Geology* **202**, 14–23, doi:10.1016/j.enggeo.2015.12.028.
- Hanssen, R. F. (2001). *Radar interferometry: data interpretation and error analysis*, vol. 2. Springer Science & Business Media, doi:10.1007/0-306-47633-9.
- Hasan, K., Aanstoos, J. V. & Mahrooghy, M. (2013). Stressed vegetation identification by SAR time series as an indicator of slope instability in Mississippi river levee segments. In *Applied Imagery Pattern Recognition Workshop (AIPR): Sensing for Control and Augmentation*, IEEE, pp. 1–4, doi:10.1109/AIPR.2013.6749307.
- Hendriks, R. F. A. (2004). An analytical equation for describing the shrinkage characteristics of peat soils. In *12th International Peat Congress*, International Peat Society, pp. 1343–1348.

- Jamalinia, E., Vardon, P. J. & Steele-Dunne, S. C. (2019). The effect of soil-vegetation-atmosphere interaction on slope stability: a numerical study. *Environmental Geotechnics*, **Ahead of print**, doi:10.1680/jenge.18.00201.
- Jamalinia, E., Vardon, P. J. & Steele-Dunne, S. C. (2020). The impact of evaporation induced cracks and precipitation on temporal slope stability. *Computers and Geotechnics* **122**, 103506, doi:10.1016/j.compgeo.2020.103506.
- Kim, D. J., Vereecken, H., Feyen, J., Boels, D. & Bronswijk, J. J. B. (1992). On the characterization of properties of an unripe marine clay soil: I. shrinkage processes of an unripe marine clay soil in relation to physical ripening. *Soil Science* **153**, No. 6, 471–481, doi:00010694-199206000-00006.
- Kroes, J. G., van Dam, J. C., Bartholomeus, R. P., Groenendijk, P., Heinen, M., Hendriks, R. F. A., Mulder, H. M., Supit, I. & van Walsum, P. E. V. (2017). *SWAP version 4, Theory description and user manual*. Wageningen Environmental Research, ESG Report 2780.
- Li, J. L., Lu, Z., Guo, L. & Zhang, L. (2017). Experimental study on soil-water characteristic curve for silty clay with desiccation cracks. *Engineering Geology* **218**, doi:10.1016/j.enggeo.2017.01.004.
- Péron, H., Delenne, J.-Y., Laloui, L. & El Yousoufi, M. S. (2009). Discrete element modelling of drying shrinkage and cracking of soils. *Computers and Geotechnics* **36**, No. 1-2, 61–69, doi:10.1016/j.compgeo.2008.04.002.
- Plaxis BV (2018). PLAXIS Reference Manual 2018. *Technical report*, Delft, the Netherlands.
- Sánchez, M., Manzoli, O. L. & Guimarães, L. J. (2014). Modeling 3-D desiccation soil crack networks using a mesh fragmentation technique. *Computers and Geotechnics* **62**, 27–39, doi:10.1016/j.compgeo.2014.06.009.
- Schapendonk, A. H. C. M., Stol, W., van Kraalingen, D. W. G. & Bouman, B. A. M. (1998). LINGRA, a sink/source model to simulate grassland productivity in Europe. *European Journal of Agronomy* **9**, No. 2-3, 87–100, doi:10.1016/s1161-0301(98)00027-6.
- Sedighi, M., Hepburn, B. D. P., Thomas, H. R. & Vardon, P. J. (2018). Energy balance at the soil atmospheric interface. *Environmental Geotechnics* **5**, No. 3, 146–157, doi:10.1680/jenge.15.00054.
- Shen, Z.-J. (2006). Progress in binary medium modeling of geological materials. In *Modern Trends in Geomechanics* (Wu, W. & Yu, H.-S., eds.), Berlin, Heidelberg: Springer Berlin Heidelberg, pp. 77–99.
- Sima, J., Jiang, M. & Zhou, C. (2013). Modelling desiccation cracking in thin clay layer using three-dimensional discrete element method. *AIP Conference Proceedings* **1542**, No. 1, 245–248, doi:10.1063/1.4811913.
- Trabelsi, H., Jamei, M., Zenzri, H. & Olivella, S. (2012). Crack patterns in clayey soils: Experiments and modeling. *International Journal for Numerical and Analytical Methods in Geomechanics* **36**, No. 11, 1410–1433, doi:10.1002/nag.1060.

- van Dam, J. C. (2000). *Field-scale water flow and solute transport: Swap model concepts, parameter estimation and case studies*. Ph.D. thesis, Wageningen University, Wageningen, The Netherlands.
- Vardon, P. J. (2015). Climatic influence on geotechnical infrastructure: a review. *Environmental Geotechnics* **2**, No. 3, 166–174, doi:10.1680/envgeo.13.00055.
- Wang, Z. F., Li, J. H. & Zhang, L. (2011). Influence of cracks on the stability of a cracked soil slope. In *Proceedings of the 5th Asia-Pacific Conference on Unsaturated Soils (AP-UNSAT 2011)*, pp. 721–728.
- Zhang, X., Chu, J. & Bulut, R. (2014). *Soil behavior and geomechanics*. American Society of Civil Engineers, doi:10.1061/9780784413388.

# 4

## A DATA-DRIVEN SURROGATE APPROACH FOR THE TEMPORAL STABILITY FORECASTING OF VEGETATION COVERED DIKES

*A comprehensive numerical simulation is computationally too expensive to be used for near real-time analysis of a dike network under climate and vegetation conditions. Therefore, this chapter investigates a Random Forest (RF) regressor to build a data-driven surrogate for a numerical model to forecast the temporal macro-stability of dikes. To that end, daily inputs and outputs of a ten-year coupled numerical simulation of an idealised dike (2009-2019) are used to create a synthetic dataset, comprising features that can be observed from a dike surface, with the calculated Factor of Safety (FoS) as the target variable. The dataset before 2018 is split into training and testing sets to build and train the RF. The predicted FoS is strongly correlated with the numerical FoS for data that belongs to the test set (before 2018). However, the trained model shows lower performance for data in the evaluation set (after 2018) if further surface cracking occurs. This proof-of-concept shows that a data-driven surrogate can be used to determine dike stability for conditions similar to the training data, which could be used to identify vulnerable locations in a dike network for further examination.*



## 4.1. INTRODUCTION

**D**IKES and embankments are important geo-structures that provide protection against inundation or flooding (CIRIA, 2013). In the Netherlands, dikes form a large part of the existing flood defence systems, with a total length of about 18 000 km, of which 14 000 km are regional (secondary) dikes. Therefore, the continuous assessment of dikes is one of the main challenges that civil works managers and geotechnical engineers are dealing with in the Netherlands (de Vries, 2012; Cundill, 2016; Ozer, 2020). This is primarily due to the fact that the failure of these geo-structures, like other engineered and natural slopes, may have significant economic, social and environmental consequences (van Baars, 2005). Therefore, the timely analysis and prediction of stability of these slopes allow decision makers to adopt appropriate measures to minimise the risk of slope failure in hazard-prone areas.

Rainfall-induced slope failure typically happens due to the reduction of the matric suction near the slope surface and/or elevated ground water level that leads to an increase in pore water pressure (pwp) and a decrease in effective stress. Hence, the reduction of the shear resistance of the soil, and an increase in the weight of the slope, increase shear stress on the soil. Depending on the type of slope and the scale of the analysis, different methods are used for slope stability assessment.

In the context of natural slopes, where landslide forecasting is the main goal, these methods target both spatial and temporal forecasting. They range from data-driven approaches such as statistics-based methods which are typically used for regional to global slope stability analysis (Ada & San, 2018; Pourghasemi & Rahmati, 2018), to simplified physics-based methods often used on a local scale (e.g., infinite slope analysis Baum *et al.*, 2010; Conte & Troncone, 2011, 2012) and advanced numerical analysis methods such as the finite element method (FEM) at the site-specific scale (e.g., Conte *et al.*, 2018).

For engineered slopes, physics-based numerical and analytical methods prevail due to the higher accuracy of these approaches, and the typical high consequence of their failure. Physics-based models, however, require a broad range of geotechnical and hydrogeomechanical in-situ data for the accurate estimation of the state of individual slopes. Although in-situ data are typically available for the analysis of engineered slopes, practically speaking, it is impossible to have accurate slope data with very high spatial and temporal resolutions and coverage. This results in considerable uncertainty on the inputs and outputs of numerical models for analysing slope stability. Moreover, analysing the transient stability of slopes is usually computationally expensive, such that real-time simulations are virtually impossible, especially if incorporating climatic data or calibrated to observed data. Therefore, an efficient approach for slope stability prediction can provide a quick estimation of the slope condition and hence speed up the assessment process. Data-driven approaches, such as Machine Learning (ML), have the potential to fulfil this purpose. ML algorithms have been used at the regional scale to estimate slope stability. The majority of work on landslide susceptibility mapping uses variants of ML algorithms (e.g., Yilmaz, 2010; Mokarram & Zarei, 2018; Raja *et al.*, 2017; Chen *et al.*, 2017; Youssef *et al.*, 2016; Steger *et al.*, 2016; Reichenbach *et al.*, 2018; Pradhan, 2013; Pourghasemi *et al.*, 2018; Goetz *et al.*, 2015). In these studies, historical slope failures were linked with associated pre-disposing factors such as terrain features, landcover, and shallow lithology to derive a pattern (model) that link these factors to the occurrence of landslides.

In recent years, static susceptibility maps have been combined with dynamic data for forecasting rainfall-induced landslides (e.g., Rossi *et al.*, 2012; Kirschbaum *et al.*, 2015; Kirschbaum & Stanley, 2018; Hartke, 2019; Jia *et al.*, 2020). For instance, Segoni *et al.* (2015) used a susceptibility model, constructed using Random Forest (RF) classification, rainfall measurements and empirical rainfall thresholds to predict potential rainfall-induced landslides in northern Italy. A similar approach has been used for landslide ‘now-casting’ at the global level (Kirschbaum & Stanley, 2018).

Recently, several studies have employed data-driven methods for evaluating the stability of slopes (Tien Bui *et al.*, 2016). Wei *et al.* (2021) used historical rainfall records and pwp measurements from a slope in Hong Kong to train ML-based prediction models. Chakraborty & Goswami (2017) estimated the factor of safety (FoS) of 110 slopes with various geometric and shear strength parameters using ML. They compared the obtained results with a finite element (FE) model, and an acceptable rate of accuracy was observed for the predicted FoS. Pei *et al.* (2019) used RF and regression tree predictive models in soil-landscape modeling for predicting the depth of the failure plane on a regional basis. They developed a classification for detecting the safe and hazardous slopes by aid of FoS calculations. Qi & Tang (2018) used different ML classification algorithms including RF (with the highest accuracy among all models) to forecast the slope stability for 148 slopes, using geometric characteristics (slope angle and height) and soil parameters (cohesion, internal friction angle and unit weight). While these studies were successful in identifying vulnerable slopes, temporal changes in the FoS were not identified. Among the different algorithms used in predicting slope stability conditions, ensemble tree-based methods such as RF classifiers and regressors proved to be promising (Pourghasemi & Rahmati, 2018; Ada & San, 2018; Lin *et al.*, 2018; Qi & Tang, 2018). These methods are known to be robust against over-fitting, in which case the model performs well on training data, but performs poorly on the test set. Moreover, as the number of trees increases, the generalisation error (a measure for the algorithm accuracy in predicting target values/class for previously unseen data) converges to a limit (Breiman, 2001).

While static slope parameters (e.g., layering, cohesion, internal friction angle and unit weight) can be measured, a high degree of accuracy at the regional scale is challenging, and temporal changes (e.g., degree of saturation, suction, bulk density) are generally neither known nor feasible to measure at the regional scale, without cost-prohibitive extensive monitoring. Continuous analysis and prediction of dike stability (and any other slope stability), however, is not possible without proper physical inspection and monitoring. This is because the slope failure is a time-dependent process that causes the deterioration or damage of slope components and ultimately leads to failure (Cundill, 2016). Periodic inspections are often used to assess the overall condition of dike systems, and detect vulnerable areas, which generally use surface conditions, e.g., cracks and vegetation, to imply the dike condition. Dike inspection procedures, regulations and processes (e.g., frequency and criteria) vary between countries (CIRIA, 2013). There are in-situ monitoring systems, such as electrical resistivity tomography, by which the dike condition can be assessed through, for instance, crack openings and water infiltration (Hojat *et al.*, 2020). In the Netherlands, the current monitoring methods of dikes usually consist of infrequent ground-based visual inspections (typically twice per year for regional dikes (Chapter 2)), which rely highly on expert judgement. Thanks to (low cost or free)

satellite images that have become available in recent years, there is a potential to use large (global) data sets to inspect slopes from space. For instance, vegetation indices (VIs) are accessible through both optical and radar remote sensing, and surface displacement can be measured with the interferometric synthetic aperture radar (InSAR) techniques (Hanssen, 2001; Ferretti *et al.*, 2001). InSAR deformation/displacement analysis techniques provide surface deformation with high spatial and temporal resolution, e.g., 5 m by 20 m at every 6 day repeat cycle for the Sentinel-1 satellite (ESA, 2020). In Chapter 5 this topic is discussed in more detail. InSAR techniques have been shown to be able to quantify the movements of unstable slopes, and it has been shown to be highly effective in mapping slow landslides (Carlà *et al.*, 2019).

In the previous chapters it is showed that transient surface displacement and vegetation condition have strong correlations with the slope FoS, due to their correlation with the moisture content of the slope. In Chapters 2 and 3, the meteorological data combined with soil parameters were used as input for the numerical model to estimate the change in FoS and the non-linear hydro-mechanical behaviour of a dike under various weather and vegetation conditions. The results of numerical study are qualitatively validated using in-situ data from an instrumented dike of the Veenderij project (de Vries, 2012) in this chapter. The same temporal signature and strong correlation in key parameters have been observed in the real dike. As both the transient surface displacement and vegetation condition are observable features, they can be used for dike inspection, and for calculating the FoS to predict the macro stability of dikes.

In this chapter, we present a proof-of-concept that a data-driven approach can be used to emulate expensive numerical simulations, to calculate the factor of safety of dikes utilising only Earth observation (EO) data. First, the slope surface parameters most closely related to the FoS are identified. These parameters, together with results from a detailed numerical model, are then used to train an RF regression model to predict the slope stability state. Results of the prediction models are validated with the calculated FoS from the numerical simulations to evaluate the performance of the data-driven method. The factor of safety (or other measures of safety) are not measurable quantities, and even dike failure would also be a single data point, i.e., the factor of safety would be known to be below 1. Therefore, the step towards validation of the method with field data has not been made. However, numerical models have been substantially validated (e.g., de Gast *et al.*, 2020); therefore, such a model is used here to trial our proof-of-concept model. This chapter aims to investigate if data-driven methods can be applied to assess a dike condition using EO data, which is not currently used in monitoring vegetation covered dikes. To the author's knowledge, this is the first time that data-driven methods have been applied to dike stability calculations, only considering parameters which can be obtained from EO and the first time in which vegetation and climatic conditions have been considered. Therefore, one illustrative case study is utilised to show the application of this methodology, highlighting its potential strengths and limitations.

## 4.2. METHOD

The integrated crop-geotechnical model that proposed in previous chapters for the numerical simulation of dikes under hydro-meteorological conditions and the influence of vegetation, provide detailed hydro-geomechanical and safety analysis of an idealised

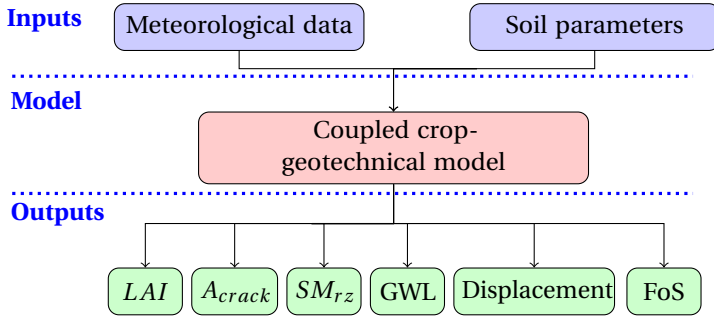


Figure 4.1: Flow chart of numerical modelling procedure.

dike in order to create a 10-year-long time series of synthetic data of the dike behaviour. These results are analysed to identify the observable features of the model that have the strongest influence on FoS. As the intention here is to estimate the transient FoS from the dike surface, only superficial transient features are investigated. The features are used to train an RF algorithm to predict the stability/safety of the dike.

#### 4.2.1. INTEGRATED CROP-GEOTECHNICAL MODEL

Commonly used geotechnical models (e.g., PLAXIS (Plaxis BV, 2018)) do not simulate the dynamic effects of vegetation on water flux (evaporation and influx) and therefore do not consider the influence that vegetation may have on soil–atmosphere interactions and slope stability. Crop models, however, have been used to simulate the interaction of vegetation and the upper soil layers (e.g., LINGRA (Bouman *et al.*, 1996)). In Chapter 2, the two models (LINGRA and PLAXIS) were coupled together to assess the effect of variable climatic and vegetation conditions on dike stability. As evaporation-induced cracks alter the water balance in a dike by increasing flow through the cracks and at the same time reducing the shear strength of the root zone, the model was further modified to include the effect of surface cracks in Chapter 3. Here, it is assumed that the cracks do not seal (close) in the wet periods, but only expand during unprecedented dry conditions. For example, if a crack is developed when root zone soil moisture ( $SM_{rz}$ ) is 0.2 (cm<sup>3</sup> water cm<sup>-3</sup> soil), it will expand when  $SM$  drops below 0.2. However, the crack area does not change if  $SM$  reverts above 0.2. The key inputs and outputs of the model are shown in Fig. 4.1. The outputs are explained further in Section 4.3.1, and the outputs of the integrated crop-geotechnical model used to provide synthetic data in the current chapter.

#### 4.2.2. MACHINE LEARNING METHOD

The synthetic data set, from the integrated crop-geotechnical model, is used to build and train an RF algorithm to predict the safety/stability condition (i.e., FoS) of the vegetated dike. The main idea here is to estimate the stability of the dike, without repeating expensive numerical simulations, using data that can be potentially observed without physical contact measurements. The general procedure for the ML model in this research is shown in Fig. 4.2. The input features of the RF model include rain and temperature values obtained from the meteorological data, as well as  $LAI$  and displacement, which

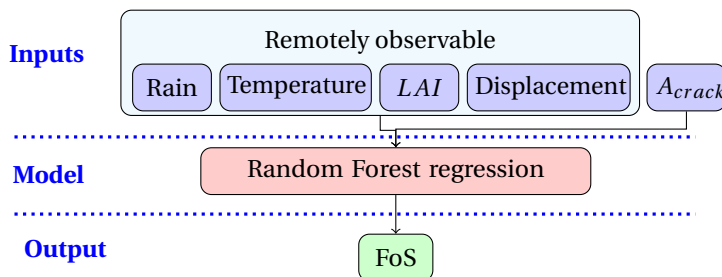


Figure 4.2: Flow chart of machine learning (ML) procedure.

4

are readily observable using remote sensing. The chosen parameters are also those with the highest impact on the target value, i.e., the FoS. For instance, rain and air temperature have a higher influence on FoS rather than other meteorological parameters used in the numerical study. In addition, the importance of  $A_{crack}$  as an input feature is investigated, as it is in theory observable from the dike surface, but there are no methods to do so remotely yet available. The target (output) variables of the RF model are the FoS values predicted by the numerical model. The temporal resolution is 1 day for all of the features;  $LAI$ ,  $diff[LAI]$  and  $A_{crack}$  are averaged over the surface. Displacement is retrieved for one location (one point) on the surface. The target value, FoS, is considered for the whole dike geometry.

#### RANDOM FOREST ALGORITHM

The random forest (RF) method, which was introduced by Breiman (2001), is an ensemble learning method used for classification and regression. The RF algorithm is based on an ensemble of decision trees (DT) for classification or regression trees (RT) for regression. In this study, we use RTs, since the target outputs are quantities (not classes) that need to be predicted. The Python library ‘Scikit-learn’ (Pedregosa et al., 2011) has been used here for the RF regression analysis.

The RF is a series of tree-like graphs, as shown schematically in Fig. 4.3. A decision/regression tree (DT/RT) is a set of decision boundaries (yes/no questions or thresholds) regarding every feature in the training data that eventually leads to a predicted class or value for classification or regression, respectively. For regression, this threshold is obtained by scanning through all the values of that feature in the training data and finding the threshold (called the optimal threshold here) that results in the minimum sum of square of the difference between the predicted target value and the actual target value. A root node is the entry node on top of the RT, where a first decision boundary is set by asking if the first selected feature (can be any feature in the context of random forest) is less than or greater than an optimal threshold. This action divides the data into smaller subsets, where the action is repeated for other features (intermediate nodes) and the tree is expanded until the decision is made about the target value in the last node (leaf node). More information on DTs can be found in Breiman et al. (1984).

For regression, RF builds a number of regression trees ( $N$ ) and the final predicted values are obtained by the aggregation of the results of all individual trees. The random forests regression predictor is described by the following equation (Zhou et al., 2019):

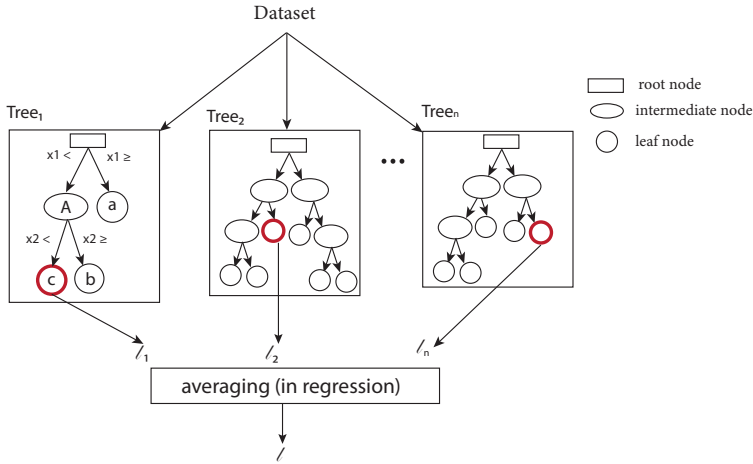


Figure 4.3: Basic structure of RF regressor:  $x = \{x_1, x_2, \dots\}$  are features,  $n$  is the number of trees,  $l$  is the target value (after Verikas *et al.* (2016)).

$$l(x) = \frac{\sum_{n=1}^N l_n(x)}{N} \quad (4.1)$$

where  $l$  is the output, in this case the FoS,  $x$  is the input vectors for the RF model,  $n$  denotes the tree number and  $N$  is the number of regression trees in the forest.

Compared to other tree-based algorithms, e.g., those constructed based on boosting (e.g., XGboost), RF is less affected by noise and can generalise better. This improves the stability and accuracy of the model, reduces variance and helps to avoid over-fitting. In addition, RF has fewer parameters (known as hyper-parameters (HPs)) to tune, and it is easier to visualise and understand. Hastie *et al.* (2009) show that RFs do remarkably well, with very little tuning required compared to other tree-based models. One of the limitations of RF regressors, similar to many other ML algorithms, is that they are not able to extrapolate. In other words, the range of predictions an RF can make is bound by the highest and lowest target and feature values in the training set.

#### BUILDING AND TRAINING THE RF MODEL

The data set, including features and corresponding target values, is divided into training and test sets. During training, each tree in the RF 'sees' the answers, and can learn how to predict the target from the features. The RF model learns the relationship between features and the target in training. When testing, the RF is asked to make predictions based on features in a test set. Finally, the model performance is evaluated by comparing the predicted target values and actual values in the test set.

The RF building and learning algorithm has several HPs that have to be defined by the user. For example, the number of observations drawn randomly for each tree, the number of features drawn randomly for each split (branch), the splitting rule, the minimum number of samples that a node should have, and the number of trees must be defined.

The basic steps for forming a RF algorithm are (after Hastie *et al.*, 2009):

- A section of training data (with replacement) is selected. This is made up of a number of samples (the full set of observable features associated with each time point).
- For each selection, a regression tree is constructed, constrained by the user-defined hyper-parameters. At each node, a threshold is determined for a single (randomly selected) feature. The data are then partitioned until a best estimate of the output is calculated.
- The target value from every decision tree is predicted.
- Voting of predicted results is conducted to achieve the terminal predicted results. In a regression RF, voting means using the mean value of results.

In ML, tuning refers to the task of finding the optimal HPs from candidate hyper-parameters for a considered data set (Probst *et al.*, 2019), that results in the best performance. Here, k-fold cross validation (Stone, 1974) is used, as it is one of the most common methods of hyper-parameter tuning. The data in the training set are randomly divided into  $K$  roughly equal-sized groups. For the  $k$ th group, the model is then trained over the remaining  $K - 1$  groups. Then, the prediction error of the fitted model on the  $k$ th group is calculated. This iteration is repeated  $K$  times and the prediction errors are averaged. This cross-validation procedure gives more reliable results as the variance of the estimation is reduced (Hastie *et al.*, 2009).

#### FEATURE IMPORTANCE

It is useful to know the relative importance or relevance of each feature (input variable) to the predicted response (target variable). This helps the user to understand the important drivers for RF to reach its prediction.

In each tree from an RF model, every node implements a condition on a single feature. In other words, that feature is used to make a decision on how to divide the data set into two separate sets (e.g., feature  $x_1$  in Fig. 4.3) which have similar responses. The features for nodes in regression trees are selected based on variance reduction in ‘impurity’. Impurity is a measure of how badly the target data (here FoS) at a given node fits the built model. During the training of a regression tree, it can be computed how much each feature decreases the impurity by variance reduction in a tree. For a forest, the ‘impurity’ decrease from each feature can be averaged across the forest and the features are ranked according to this measure. In this study, the RF regressor calculates variance reduction using the mean squared error (MSE) to measure the quality of a split (selecting the optimal value) in intermediate nodes (Pedregosa *et al.*, 2011).

#### 4.2.3. CASE STUDY

##### NUMERICAL MODEL

The same example dike used in the previous chapters is also used for this data driven study (Fig. 4.4). The points that data will be showed later in Section 4.3.1 are presented in Fig. 4.4. The data from the adopted version of the integrated crop-geotechnical model that introduced in Chapter 3, for 10 years of climate data for cracked soil is used in this chapter.

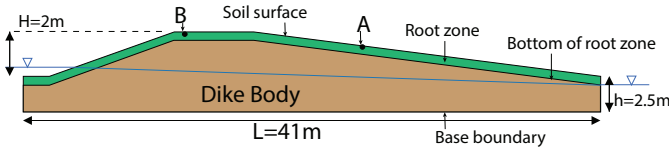


Figure 4.4: Example dike simulation geometry.

### RF MODEL

The RFs are built and trained on the synthetic data set generated using the integrated crop-geotechnical model of the example dike for cracked condition. The data are presented in Chapter 3. The predictive performance of RF regression is investigated in two scenarios.

- Real-time assessment ( $RF_{rta}$ ): the dike safety (FoS) is assessed in real-time based on the observable data. The features are selected from the same day on which the FoS is estimated by the RF model.
- Short-term prediction ( $RF_{stp}$ ): the dike safety is calculated for some days in the future. This time lag gives dike managers enough time to take necessary actions before the occurrence of potential catastrophic events. All features except rainfall and temperature are for some days prior to the day that FoS is estimated. Rainfall and temperature correspond to the day on which FoS is calculated by the RF model.

In both scenarios, three data sets are formed from the 10-year synthetic data. The data before 2018 will be used for training and testing the RF models: 80% of data are randomly selected as a training set and the remaining 20% as a test set. The data after 2018 are used for independent evaluation of the trained and tested model to check the performance of the trained model on data that it has never ‘experienced’. This set is called the evaluation set, and is useful to explore the generalisation of the model.

### RF MODEL HYPER-PARAMETERS TUNING

To choose the best HPs for the two RF regressors, a 10-fold cross validation (10-CV) was performed on the corresponding training data. The impact of three different values of  $K$  (5, 10 and 15) was tested for the  $RF_{rta}$  model. As the influence of the  $K$  within this range was found to be negligible, 10-CV was selected for all RF models. The HPs tuned here are as follows: (i) The number of trees in the forest (n-estimator); (ii) The maximum depth of the trees, which is the maximum number of splits until the leaf node; (iii) The min-samples-split which represents the minimum number of samples (observations) in a node which undergoes splitting, this can vary between one sample to all of the samples at each node. When this parameter is increased, each tree in the forest is increasingly constrained; (iv) The min-samples-leaf parameter specifies the minimum number of samples required to be at a leaf node. The considered candidates for each hyper-parameter are listed in Table 4.1; the chosen candidates are within the reasonable range that usually are used in RF models.



Table 4.1: List of candidate values for hyper-parameter for all RF models

Parameter	Tested value
n-estimator	[10, 50, 100, 200, 300, 500, 700, 1000, 1500, 2000]
max tree-depth	[10, 30, 50, 70, 100, 150, 200]
min-samples-split	[2, 3, 4, 5, 8, 10]
min-samples-leaf	[1, 2, 3, 4, 5]

### 4.3. RESULTS AND DISCUSSION

#### 4.3.1. INTEGRATED CROP-GEOTECHNICAL MODEL SIMULATIONS

The outputs of the numerical simulations using the integrated crop-geotechnical model are shown in Fig. 4.5. The temporal variation in the crack area is shown in Fig. 4.5(a). As mentioned in Section 4.2.1, it is assumed that cracks do not seal, and that crack formation is therefore irreversible. Most cracking occurs in the first year (2009) after the analysis starts. During wet periods in 2009 (May–August), the crack size remains constant until the next drier period in June 2009. Then, again in the summer of the next two years, the soil experiences the next drier condition, and as a result, cracks expand. The time between cracking events gets longer as the crack expands, only in conditions drier than the previously experienced ones. After 6 years, there is almost no additional cracking until summer 2018, when the driest conditions occurred and  $A_{crack}$  reached the maximum value in the studied period. Temporal variations of  $LAI$  are shown in Fig. 4.5(b). The sudden decrease in  $LAI$  on mid-June and mid-August every year is due to mowing events, indicated by vertical dashed lines. These were introduced into the crop model based on the mowing schedule of regional dikes in the Netherlands (Chapter 2). In Fig. 4.5(c), the change of vegetation growth ( $diff[LAI]$ ) in a time window of 15 days is plotted.

The presence of cracks is seen to decrease the change of vegetation growth after mowing (demonstrated by the  $diff[LAI]$ ), because less water is available in the root zone. Vegetation can re-grow between mowing events when a substantial amount of rainfall happens in this period (e.g., summer 2014); however,  $diff[LAI]$  is almost zero when there is a dry period between mowing events (e.g., summer 2018).

The ground water level ( $GWL$ ) measured relative to the base boundary at point A (see Fig. 2.1), is shown in Fig. 4.5(e). During wet periods, the water level in the example dike increases, when the soil moisture in the root zone  $SM_{rz}$  reaches the field capacity. As the spring starts and  $SM_{rz}$  reduces, the  $GWL_A$  typically decreases and reaches the minimum value in July 2018 when  $SM_{rz}$  has the lowest value during the studied period. Fig. 4.5(f) shows the magnitude of the surface displacement at point A ( $|U_A|$ ), which follows a pattern similar to  $GWL_A$  in Fig. 4.5(e). The seasonal cycle in  $|U_A|$  is caused by variations in  $SM_{rz}$  and  $GWL_A$ ; in the winter period, the magnitude of displacement increases, while in the summer, it reduces. A slight accumulation of  $|U_A|$  over time is seen due to plastic displacement and growing cracks due to shrinkage behaviour in the root zone. Finally, the temporal variation of FoS is shown in Fig. 4.5(g), which is the result of the combined effect of rainfall, change in  $LAI$  and crack area variation from 2009–2019. The maximum crack area, and therefore the minimum shear strength parameter (cohesion and friction angle), lead to a minimum FoS in August 2018 when there is a heavy rainfall

event and very low *LAI* (almost bare soil), due to an extremely dry summer. The results show that the vegetation and dike condition are responsive to the climate condition and there is a similar temporal signature in all the plotted results.

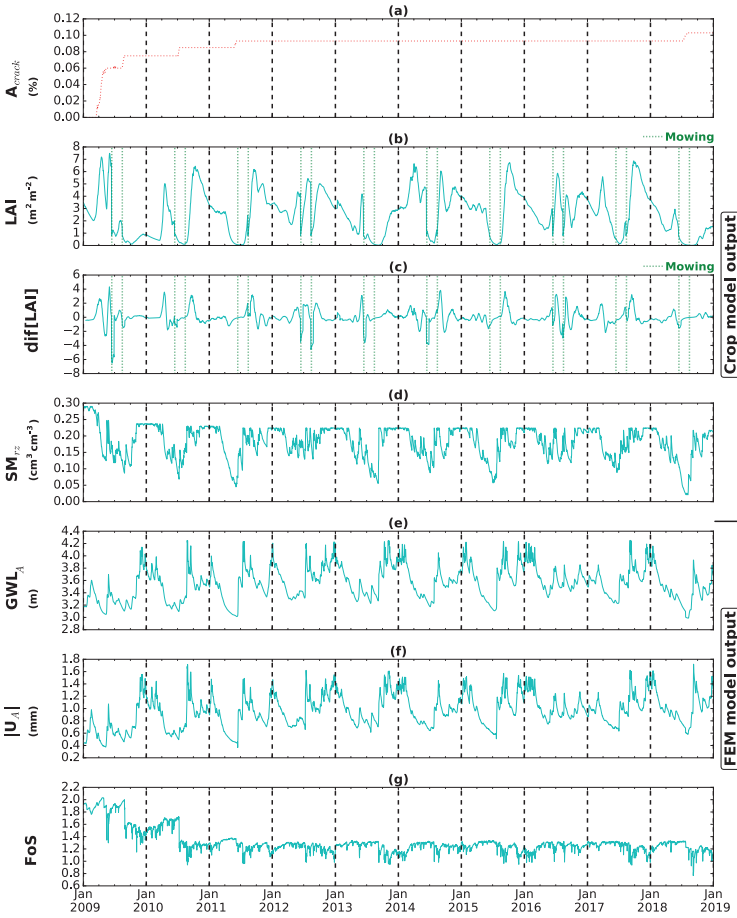


Figure 4.5: Time series outputs from the coupled model for 10 years; (a) crack area percentage ( $A_{crack}$ ); (b) Leaf Area Index (*LAI*); (c) rate of *LAI* change over 15 days ( $diff[LAI]$ ); (d) average soil moisture in the root zone ( $SM_{rz}$ ); (e) ground water level at point A ( $GWL_A$ ); (f) magnitude of total displacement at point A ( $|U_A|$ ); (g) Factor of Safety (FoS).

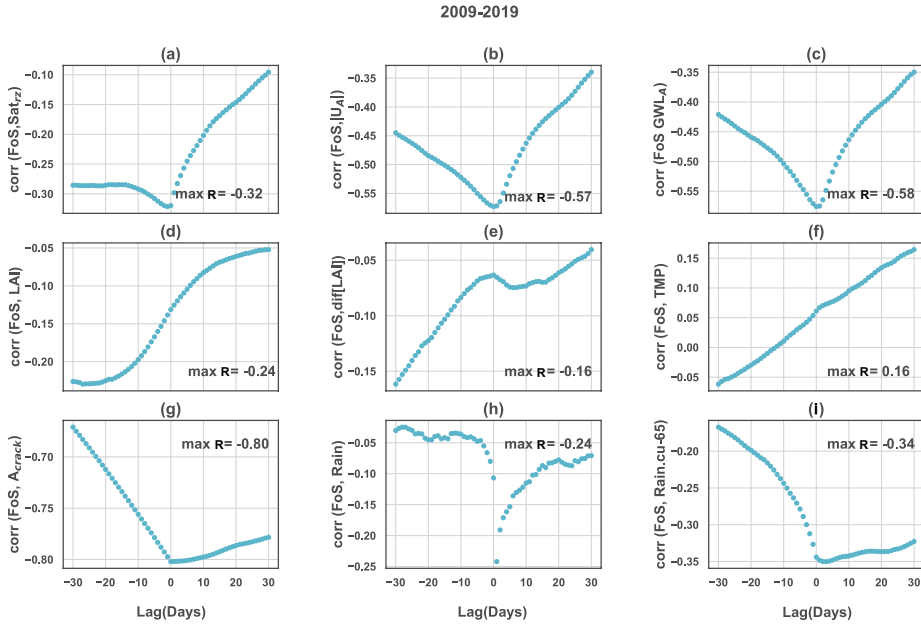


Figure 4.6: Lag correlation between FoS and (a) root zone saturation ( $Sat_{rz}$ ); (b) magnitude of total displacement ( $|U_A|$ ); (c) ground water level at point A ( $GWL_A$ ); (d) LAI; (e) rate of LAI change over 15 days ( $diff[LAI]$ ); (f) temperature ( $TMP$ ); (g) crack area ( $A_{crack}$ ), (h) rain; (i) cumulative rainfall during the last 65 days.

### 4.3.2. CORRELATION BETWEEN POTENTIAL FEATURES AND THE FACTOR OF SAFETY

Fig. 4.6 shows the correlation between pairs of FoS and selected features considering a time lag for the simulation data. A positive time lag means that the selected parameter leads the FoS (either positive or negative correlation).

As shown in Fig. 4.6(a), the root zone saturation  $Sat_{rz}$  is negatively correlated with the FoS, with the highest correlation at the same day that FoS is calculated. A higher amount of water in the root zone causes a higher pwp, thereby lowering the effective stress and then lowering the stability of the whole dike. This correlation is not strong, since if the root zone experiences very dry conditions, the cracks expand (explained in Section 4.3.1), which decreases FoS. Although  $Sat_{rz}$  is a good potential indicator for variation of FoS in time, it is not easily observable. Root zone soil moisture could be inferred from surface soil moisture, but cannot be monitored from space unless very long wavelengths are used, which will not be available in the near future (Entekhabi *et al.*, 2014).

There is a negative correlation between FoS and  $|U_A|$  and  $GWL_A$  represented in Fig. 4.6(b)-(c), respectively. This trend can be seen from the temporal variations in Fig. 4.5(e),(g). The temporal variation of surface displacement is linked to the variation of water level in the dike. Shrinkage/swelling behaviour of the soil is due to the available water in the soil or ground water level variations, which both affect the dike safety by altering effective stress. To validate this relation, the in-situ data from a regional dike in Amsterdam, the Netherlands, that was studied in the Veenderij project (de Vries, 2012),

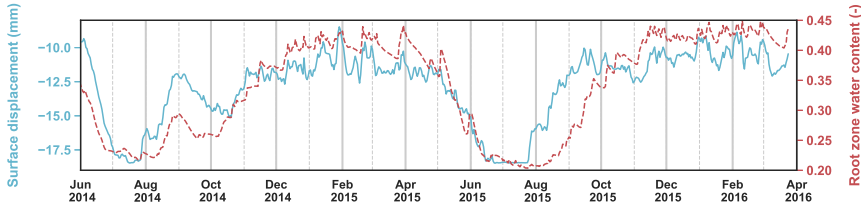


Figure 4.7: Time series of surface displacement and water content in the root zone (June 2014- April 2016).

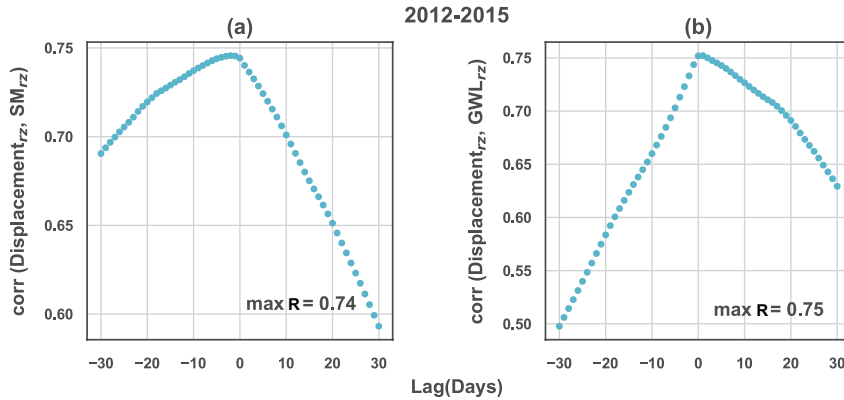


Figure 4.8: Correlation coefficient (R) between: (a) displacement and  $SM_{rz}$ , (b) displacement and  $GWL_{rz}$  in the root zone with time lags as much as 30 day during 4 years at Veenderij dike.

are analysed to confirm the simulated behaviour. Fig. 4.7 shows the temporal variation of root zone water content and displacement for a nearly two-year period (June 2014- April 2016). The shallow displacement and root zone water content have the same temporal variations. Strong positive correlations between the  $SM$  and displacement, and between  $GWL$  and displacement in the root zone for four years (January 2012-January 2016) are shown in Figs. 4.8 (a)-(b). Displacement is observable remotely; however,  $GWL$  is not, and due to the existing link between these two parameters, monitored displacement can be best used as a feature. Displacement can be measured with InSAR techniques, currently with a resolution that it cannot be assigned to a specific location on a dike. However, the displacement of the entire dike is highly correlated, as demonstrated by comparing the displacement of two points (point A and point B) in Fig. 4.9. Therefore, having the displacement of any point on a slope is useful.

There is a weak lagged correlation between  $FoS$  and  $LAI$  or rate of  $LAI$  change over 15 days ( $diff[LAI]$ ), shown in Fig. 4.6(d),(e). The overall correlation is low because vegetation growth is affected by multiple factors including  $Sat_{rz}$ , available energy, and mowing. The presence of vegetation influences stability through water balance. When rainfall occurs, vegetation reduces the amount of water that reaches the dike body; the lower pwp (higher suction) causes higher  $FoS$ . On the other hand, as cracks expand, vegetation growth is lower compared to uncracked areas. In rainfall events, preferential flows reach the soil

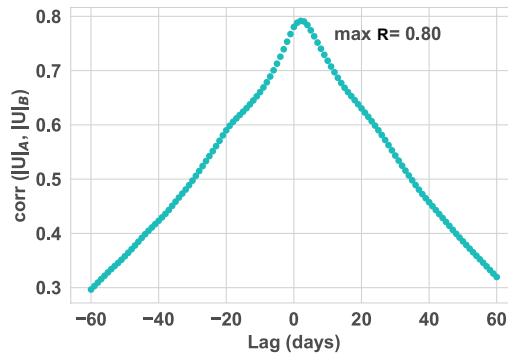


Figure 4.9: Lag correlation between magnitude of surface displacement at points A and B.

body (more pwp) and shear strength reduces. These factors together lead to a reduction in FoS.

It was also shown that crack presence affected the  $dif[LAI]$ . Evapotranspiration from the root zone increases due to the crack growth and less water is available for the grass to grow, thereby  $dif[LAI]$  is reduced as crack area increases.  $LAI$  can easily be monitored using space-borne instruments.

Temperature has a weak correlation with FoS (Fig. 4.6(f)) due to the indirect relation it has on dike stability. In the growing seasons, air temperature is high and vegetation grows. Without rainfall, this causes soil drying, which results in soil cracking and reduction of the  $LAI$ . In addition, the air temperature influences the evapotranspiration demand, which influences the  $Sat_{rz}$  variations, already discussed above. The temperature is most strongly correlated with FoS at the maximum time lag considered (30 days) before the FoS. Temperature is measured via existing weather stations, and does not have significant local variations. Therefore, temperature can be used as a feature for an indirect way of assessing the FoS.

The strong negative correlation between crack area and dike safety, shown in Fig. 4.6(g), is the consequence of reduction in the shear strength, and preferential flows through the cracks that cause an increase in pwp in the dike body, thereby lowering effective stress and FoS. While the maximum correlation is with a zero time lag, a positive time lag retains a high correlation. Although  $A_{crack}$  has a strong correlation with FoS, it is impractical with current methods to measure the crack area remotely.

Rainfall has a negative correlation with FoS mostly with 1 day lag,  $\max R = -0.24$  (Fig. 4.6(h)), indicating that rain causes a change in FoS after one day, with a low correlation outside of a single day. To consider the effect of antecedent rainfall on dike stability, the correlation between cumulative rainfall with the different time windows and FoS was tested and a 65-day window ( $Rain_{cu-65}$ ) in Fig. 4.6(i) was found to have the strongest correlation with FoS.

Table 4.2: Tuned hyper-parameters for constructed RF models.

RF model	n-estimator	max tree-depth	min-samples-split	min-samples-leaf
RF <sub>rt<sub>a</sub></sub>	700	200	2	1
RF <sub>rt<sub>a</sub>,Rain-1d</sub>	700	70	2	1
RF <sub>rt<sub>a</sub>,Acr</sub>	2000	200	2	1
RF <sub>stp,15d</sub>	700	30	2	1
RF <sub>stp,15d,Acr</sub>	1500	30	2	1
RF <sub>stp,5d</sub>	1000	100	2	1

### 4.3.3. RF REGRESSION

The results from the previous section are used to build a predictive model. Firstly, an RF is built, tuned and tested using easily observable features available at the time where the output (FoS) is required, i.e., a real-time assessment (RF<sub>rt<sub>a</sub></sub> and RF<sub>rt<sub>a</sub>,Rain-1d</sub>). This analysis is then extended utilising crack area as an important feature, which is not, at this present time, considered observable (RF<sub>rt<sub>a</sub>,Acr</sub>). Secondly, an RF is built, tuned and tested using easily observable features available 15 days prior to when the FoS is required, i.e., a short-term assessment (RF<sub>stp,15d</sub>). This analysis is then extended in two ways, using the same additional feature (RF<sub>stp,15d,Acr</sub>) and reducing the time period of the short-term prediction to 5 days (RF<sub>stp,5d</sub>). For all the RF models that have been built and used in this study, the tuned values for HPs are listed in Table 4.2.

#### FEATURE SELECTION

The feature selection was based on the available EO data that have high spatial/temporal resolutions and relatively good precision, and a good correlation with the FoS. Soil moisture and ground water level influence dike safety strongly (Figs 4.6 and 4.8), but they are difficult to observe without ground-based monitoring. Therefore, the selected features for FoS prediction in this study are *LAI*, *diff[LAI]*, displacement, daily rainfall, cumulative rainfall and temperature. For the short-term predictions, data related to the slope for the days before the FoS is needed are selected and meteorological data (cumulative rainfall and temperature) are used on the event day, as reliable short term meteorological predictions are available.

To avoid a complex model and over-fitting, uncorrelated features should be used as inputs. Therefore, the selected features are tested to examine if they are highly correlated or not. In Fig. 4.10, the correlations between the selected features for all RF regressors are plotted. The features are not highly correlated and can therefore be used as candidate features to build the models for real-time assessment (Fig. 4.10(a)) and short-term prediction (Fig. 4.10(b),(c)).

#### REAL-TIME ASSESSMENT

The RF<sub>rt<sub>a</sub></sub> model is built and trained based on the selected hyper-parameters and features. The feature importance values constitute the relative predictive power of the features and are shown in Table 4.3, where surface displacement ( $|U_A|$ ) is seen to have the highest importance, 0.42. It is also shown in Section 4.3.2 that  $|U_A|$  has a strong correlation with FoS. Cumulative rainfall during the last 65 days (*Rain.cu-65*) has the second highest

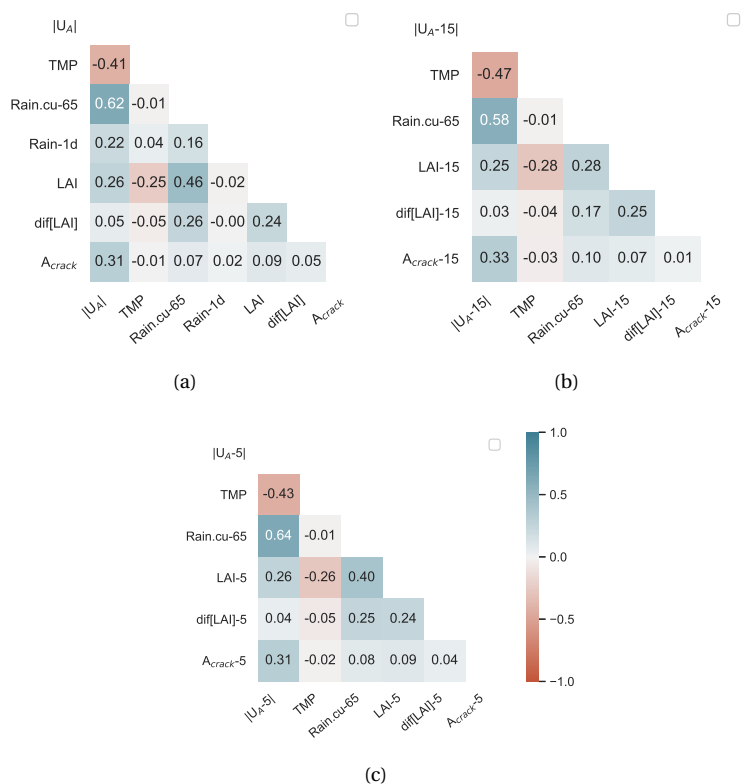


Figure 4.10: Correlation between features for (a) real-time assessment, (b,c) short-term prediction RF models with 15 days and 5 days lag, respectively.

importance, with a feature importance of 0.22, and  $LAI$  at the event day has a lower importance of 0.17. The feature importance of both vegetation growth over the past 15 days ( $dif[LAI]$ ) and temperature ( $TMP$ ) are low, 0.1 and 0.07 respectively. The displacement is the most direct proxy for the water effect within the dike, whereas the rainfall amount and amount of vegetation and temperature influence the water flux, therefore it is logical that they have a lower importance. The rate of vegetation growth is influenced by various climatic variables, and was seen previously in chapter 3, Fig. 3.10, to have a different response at different times of the year, therefore it is reasonable for it to have the lowest importance.

Figs. 4.11(a),(b) show the predicted FoS versus the numerically calculated FoS for the test set and the evaluation set, respectively. The points in these two plots are coloured based on  $A_{crack}$ . The coefficient of correlation (R) between the predicted and calculated FoS in the test data set is 0.94 and RMSE = 0.05. It is clear that the model performs well on the unseen data (test set) that is within its training sample space (Fig. 4.11(a)). However, when it comes to the evaluation set, the model performance deteriorates (Fig. 4.11(b));

Table 4.3: Feature importance for real-time assessment RF models.

RF model	$A_{crack}$	$ U_A $	$Rain.cu-65$	$LAI$	$dif[LAI]$	$TMP$	$Rain-1d$
$RF_{rta}$	-	0.42	0.22	0.17	0.1	0.07	-
$RF_{rta,Rain-1d}$	-	0.40	0.21	0.16	0.09	0.06	0.06
$RF_{rta,Acr}$	0.47	0.25	0.11	0.07	0.04	0.03	-

$R = 0.31$  and  $RMSE = 0.1$ . The latter value is considered a high error, since the range of calculated FoS in 2018 is from (almost) 0.8 to 1.4 (although both the  $R$  and  $RMSE$  are affected by the lower range of values). The variation of predicted and calculated FoS in 2018 is shown by the left-hand side y-axis and the dashed and dotted lines, and precipitation in the same period is shown by the right-hand side y-axis and starts in Fig. 4.11(c). The low performance of the  $RF_{rta}$  on the evaluation set can be explained based on the latter figure; until further crack growth takes place, the predicted FoS is very close to the calculated FoS (before 22 July 2018) ( $R = 0.82$ ;  $RMSE = 0.04$ ). This is also reflected on Fig. 4.11(b) by orange markers close to the diagonal line. Once cracks start growing after 22 July 2018, the predicted FoS deviates from the calculated FoS (red markers on Fig. 4.11(b)). This is particularly clear on the day with the heaviest precipitation in September 2018 (see Fig. 4.11(c)), which causes a large drop in calculated FoS. The (red) markers with the highest distance from the diagonal line correspond to rainy days after crack growth in July 2018. The  $RF_{rta}$  cannot capture the response to the heavy rainfall which occurs in this period.

As explained in Section 4.3.1, when cracks grow, the calculated FoS is affected by  $A_{crack}$  and precipitation events (drop in FoS in August 2018). This shows that the model could not generalise (extrapolate) well on the training data before 2018. Since, the RF model is not trained over the data with 10% crack area. This is mainly attributed to the combination of rainfall intensity and unprecedented crack area. In order to investigate the effect of rainfall intensity on the same day that FoS is calculated, this parameter was also included as a feature in building the next predictive model,  $RF_{rta,Rain-1d}$ . The feature importance of this model is similar to  $RF_{rta}$  (Table 4.3), except that the added feature ( $Rain-1d$ ) has a very low impact on generally predicting FoS. Since the general results of these two models are almost the same, only the time series plot is shown in Fig. 4.11(d). The  $R$  value between the predicted and calculated FoS in the test data set is 0.96 and  $RMSE = 0.05$  for  $RF_{rta,Rain-1d}$ , and in the evaluation data set,  $R = 0.32$  and  $RMSE = 0.10$ . Using  $Rain-1d$ , the performance of the predictive models improves on days with heavy rainfall, e.g., in April and October 2018, where example results are emphasised with the blue box around them. In these periods, the predicted FoS using  $RF_{rta,Rain-1d}$  is responsive to significant rainfall events, where the predicted FoS drops, following the trends in the calculated results, which is significant for predicting unsafe situations.

In an attempt to improve RF performance, a new model ( $RF_{rta,Acr}$ ) is built using  $A_{crack}$  as a feature, along with other features. The feature importance is shown in Table 4.3.  $A_{crack}$  has the highest importance among the other features (0.47).  $|U_A|$  has the second highest feature importance (0.25) and then it is followed by other features. The importance order of the observable features follows  $RF_{rta}$ .



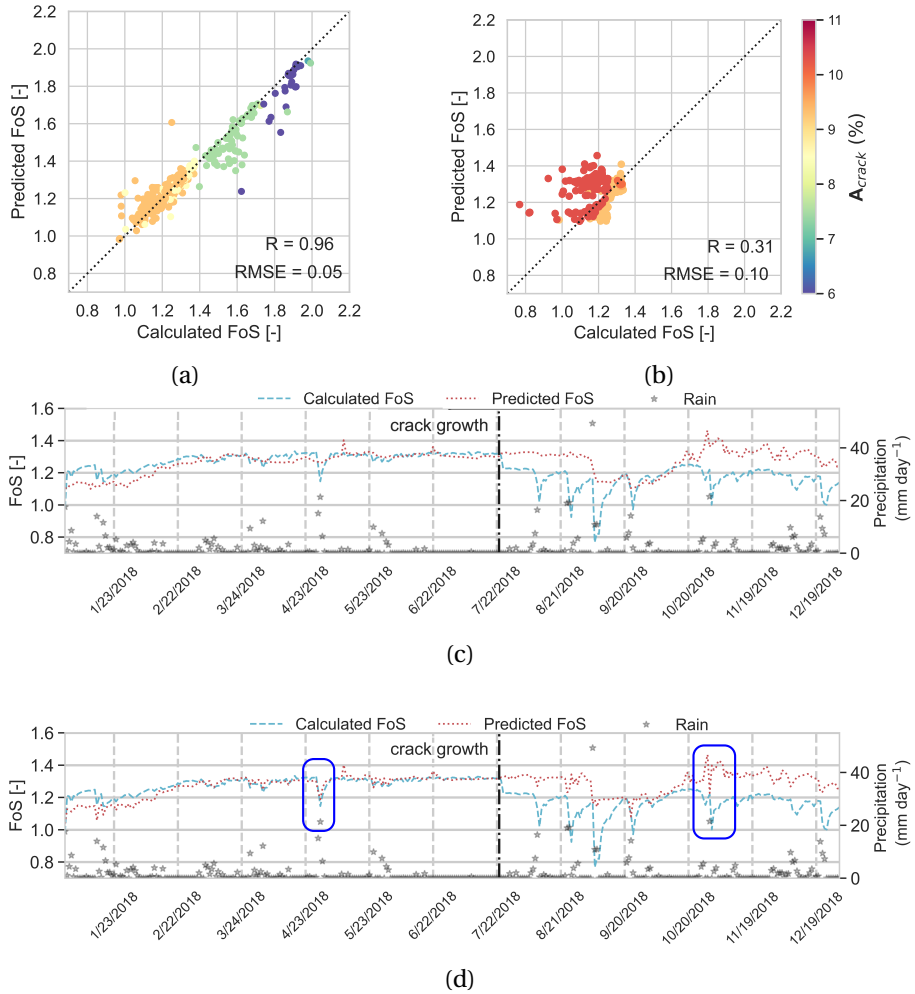


Figure 4.11:  $RF_{rta}$  model performance, over (a) testing data set and (b) evaluation data set, and (c) time series of calculated and predicted FoS in the evaluation data set; (d) time series of calculated and predicted FoS in the evaluation data set using  $RF_{rta,Rain-1d}$ .

In Fig. 4.12(a),(b), the predicted FoS from the testing and evaluation data set using the  $RF_{rta,Acr}$  model is plotted against the calculated FoS in the corresponding data set, respectively. The R value between the predicted and calculated FoS in the test data set increased to 0.98 and the RMSE decreased to 0.03 (in respect to  $R = 0.96$  and  $RMSE = 0.05$  for  $RF_{rta}$ ). For the evaluation data set,  $R = 0.56$  and the  $RMSE = 0.07$ , an improvement compared to the  $RF_{rta}$  model performance over the evaluation data set (year 2018). According to the time series plot (Fig. 4.12(c)), the overall performance of  $RF_{rta,Acr}$  is improved compared to  $RF_{rta}$ . Yet, the predicted values over-estimate the FoS after the crack expands on 22 July

2018, mostly due to the unprecedented low values, as explained before. In addition, the  $RF_{rta,Acr}$  model has a significantly smaller response to the heavy rainfall events in August–September 2018 than observed. According to Table 4.3,  $Rain_{cu-65}$  has relatively low influence (feature importance = 0.11) on the FoS prediction. This causes a deviation in the predicted FoS for results after crack growth from the calculated FoS (red points in Fig. 4.12c). However, when there is no heavy rainfall, e.g., in October 2018,  $RF_{rta,Acr}$  performs well.

In total, when including the crack area as an input feature, in addition to those in the previous model, the model performance improves. It remains a difficult feature to observe, but warrants further investigation given its importance.

Results of this section show that the built RF models have low accuracy after the new trend takes place after growing cracks in summer 2018, because the RF model is not trained for the maximum crack area period. If an RF algorithm was trained over more diverse data of different cases, the RF models may have better performance.

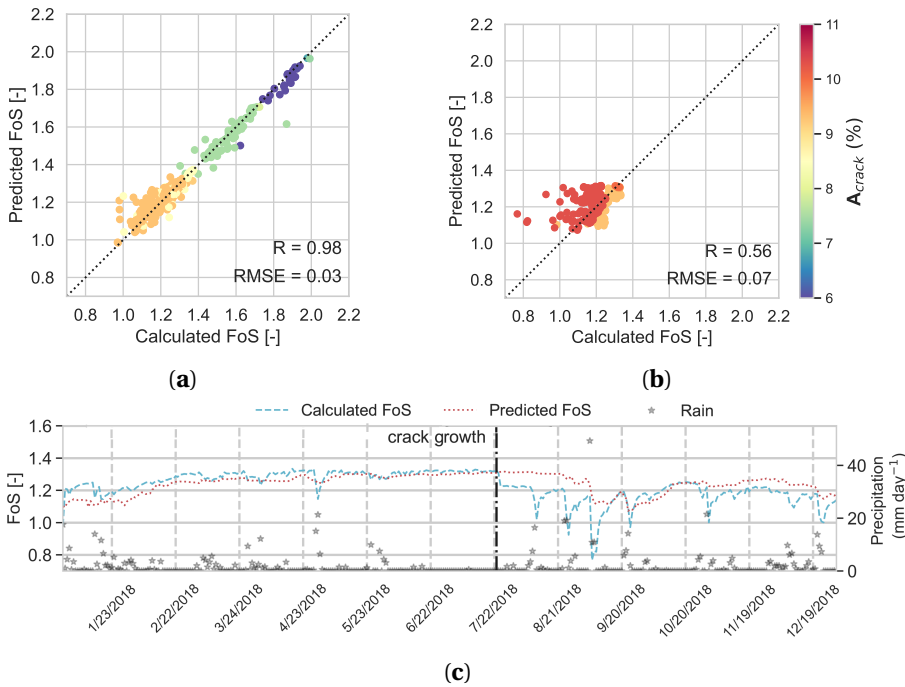


Figure 4.12:  $RF_{rta,Acr}$  model performance, over (a) the testing data set and (b) the evaluation data set; and (c) time series of predicted and calculated FoS in the evaluation data set (year 2018).

### SHORT TERM PREDICTION

In this section, it is investigated whether an RF algorithm can give a short-term forecast for the dike safety. The used features are the same as before but for an earlier time.  $LAI$ ,  $diff[LAI]$  and  $|U_A|$  are selected 15 days before the event day. It is known that these have a

Table 4.4: Feature importance for short term prediction RF models

Features	$A_{crack}$ -15/5d	$ U_A $ -15/5d	$Rain.cu$ -65	$LAI$ -15/5d	$diff[LAI]$ -15/5d	$TMP$
$RF_{stp,15d}$	-	0.32	0.23	0.22	0.10	0.08
$RF_{stp,15d,Acr}$	0.48	0.17	0.13	0.11	0.05	0.05
$RF_{stp,5d}$	-	0.36	0.23	0.19	0.12	0.08

lower correlation (see Fig. 4.6), however this gives sufficient time to undertake further inspection and take action. To enhance RF performance, the meteorological data are used based on the event day, assuming that the climate data are predicted from different climate models which are quite reliable. The time of 15 days is selected as a period, where both the meteorological predictions may be reasonably accurate and which gives the dike managers enough time to take emergency inspection and remedial actions.

In Table 4.4, the feature importance for short-term prediction (15d) is shown. Like the previous analysis of  $RF_{rta}$ ,  $|U_A|$ , 15 days before the event day (i.e.,  $|U_A-15|$ ), it has the maximum effect on FoS prediction, with the feature importance of 0.32. This is because, even with a 15-day lag, the correlation between displacement and FoS is relatively strong,  $-0.44$  (Fig. 4.6(f)).  $Rain.cu$ -65 places in the second rank with the feature importance of 0.23, which does not have the 15 days lag, and the data up to the event day are used, considering the earlier assumption of meteorological data for the next 15 days.  $LAI$ -15 has the feature importance of 0.22. The feature importance of  $diff[LAI-15]$  and  $TMP$  have the least impact on the FoS prediction, like the previous analysis in Section 4.3.3, since these two features have a very low correlation with FoS (Fig. 4.6(e),(f)).

The results in Fig. 4.13(a), which are coloured by  $A_{crack}$ , show that for  $RF_{stp,15d}$ ,  $R = 0.94$  and  $RMSE = 0.06$ . The results for the evaluation data set (Fig. 4.13(b)) show poor performance, i.e.,  $R = 0.06$  and  $RMSE = 0.14$ . As discussed before for  $RF_{rta}$ , in the evaluation data set, after cracks grow, the red markers diverge from the diagonal line, showing the deviation of predicted FoS from calculated FoS after 22 July 2018. The markers that have the highest error in prediction correspond to heavy rainfall after crack expansion and cause reductions in calculated FoS, while  $RF_{stp,15d}$  cannot predict these values. In Fig. 4.13(b),(c), the predicted FoS over 2018 is plotted against the calculated FoS in the independent data set. As before, it is seen that after the crack growth, the  $RF_{stp,15d}$  model cannot predict FoS accurately.

In an attempt to improve the results, two other analyses are tested. Firstly, as in the real-time assessment, the crack area is also considered as one of the features ( $RF_{stp,15d,Acr}$ ); secondly, the period of the short term prediction decreased to 5 days ( $RF_{stp,5d}$ ). For the former option,  $A_{crack}$  is selected from 15 days before the event day, and the other features remain as in the  $RF_{stp,15d}$  model.

As expected from previous analyses,  $A_{crack}$  has the highest impact on the RF performance (0.48); this is followed by  $|U_A-15|$  with a feature importance of 0.17. Again, the order of the feature importance for the rest of the features is the same as in the previous analysis.  $Rain.cu$ -65 has the relative importance of 0.13, then followed by  $LAI$ -15 with the relative importance of 0.11. The lowest relative importance is again for  $diff[LAI-15]$  and  $TMP$ .

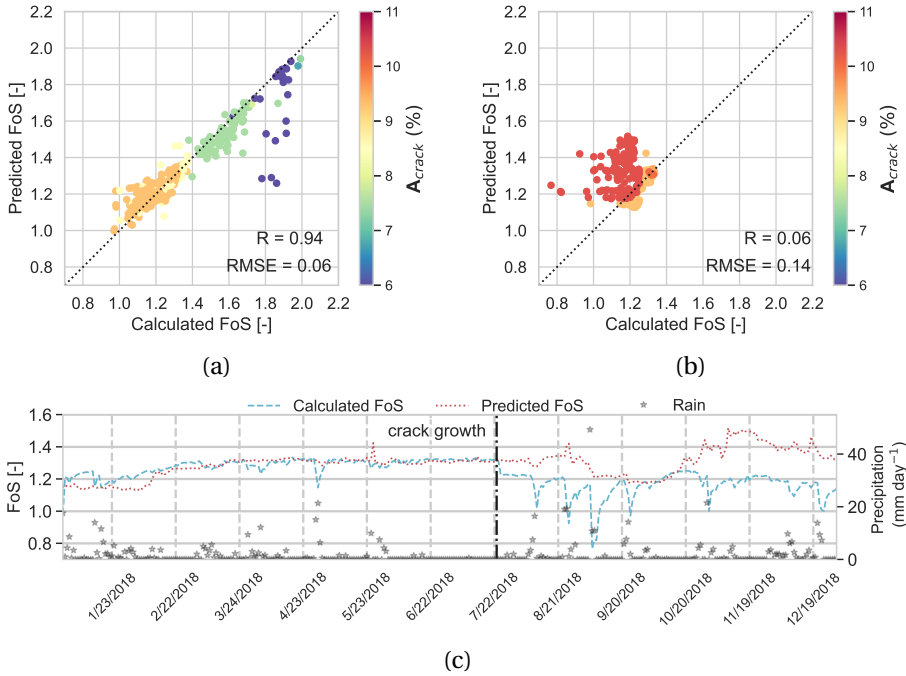


Figure 4.13: RF<sub>stp,15d</sub> model performance, over (a) the testing data set and (b) the evaluation data set, and (c) time series of predicted and calculated FoS in the evaluation data set (year 2018).

The results of RF<sub>stp,15d,Acr</sub> are shown in Fig. 4.14. The performance of the RF<sub>stp,15d,Acr</sub> model is increased compared to RF<sub>stp,15d</sub> over both testing and evaluation data sets. Adding  $A_{crack}$  leads to a higher correlation between predicted and calculated FoS in the testing data set; R increased in order of 0.04 ( $R = 0.98$ ) and RMSE is reduced by 0.02 ( $RMSE = 0.04$ ) for the evaluation data set. Again, it can be inferred that after additional crack growth, the model cannot extrapolate FoS values for the heavy rainfall events, since the relative power of antecedent rainfall in predicting FoS is relatively low (feature importance  $Rain_{cu-65} = 0.13$ ).

In another attempt to improve the short term prediction models, the lag is reduced to 5 days, which means that  $|U_A|$ ,  $LAI$  and  $dif[LAI]$  are selected from 5 days before the event day, while  $Rain_{cu-65}$  and  $TMP$  are selected from the same day that FoS is predicted;  $A_{crack}$  is no longer considered. This period can be considered as sufficient to take emergency actions before a dike fails, e.g., evacuating a residential area.

The feature importance of RF<sub>stp,5d</sub> model is shown in Table 4.4. Like the previous models,  $|U_A - 5|$  has the highest importance among other features, 0.36; this is between feature importance for  $|U_A|$  in real-time assessment and  $|U_A - 15|$  for short-term prediction (15 days). The reason can be also concluded from Fig. 4.6(b): as the time lag increases, the correlation between FoS and  $|U_A|$  decreases. The ranking order for other features for the RF<sub>stp,5d</sub> is the same as short-term prediction with 15 days lag. However, the correlation between predicted and calculated FoS is increased in RF<sub>stp,5d</sub>,  $R = 0.24$  and  $RMSE = 0.12$ ,

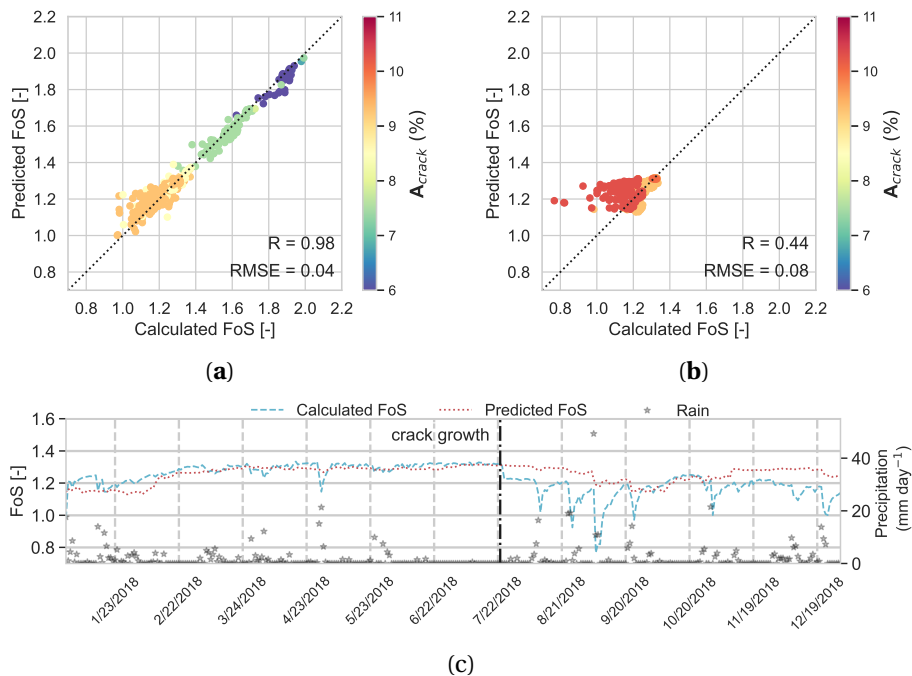


Figure 4.14:  $RF_{stp,15d,Acr}$  model performance, over (a) the testing data set and (b) the independent data set, and (c) time series of predicted and calculated FoS in the evaluation data set (year 2018).

compared to  $RF_{stp,15d}$ . As the lag decreases, the correlation between FoS and  $|U_A|$  and  $Rain_{cu-65}$  increases, which leads to an increase in the power of the features in predicting the FoS. The time series plot for 5 days' prediction is shown in Fig. 4.15(c) (again like the previous analysis), the predicted FoS after crack growth in July 2018, which deviates from the calculated FoS. Although in  $RF_{stp,5d}$ , the deviation is less from the actual FoS compared to the results of  $RF_{stp,15d}$ , it still performed poorer than  $RF_{15d,Acr}$ .

A summary of the build RF regressor ability to predict the FoS is given in Table 4.5, for the training data set, testing data set (which are randomly selected over the years 2009–2017) and the evaluation data set (year 2018). In both scenarios (real-time assessment and short-term prediction), if the crack area is used as one of the features, the model performance improves both in the testing data set and in the evaluation data set. In short-term prediction, when the time window is shortened from 15 days to 5 days, the RF model performance improves, since there is a higher correlation between the features that have the highest impact ( $A_{crack}$ ,  $|U_A|$  and  $Rain_{cu-65}$ ) and FoS at the shorter lag. Currently, it is not feasible to measure the crack area, but there are ongoing studies to simulate the crack volume, e.g., Li & Zhang (2010).

As shown in the results, using a RF regressor, the predicted values are never outside the range of training set values for the target variable (FoS). One of the RF regressor limitations is that it cannot extrapolate, because in the test set, it predicts an average of the values seen previously in the training. Therefore, the predicted FoS is bound to the

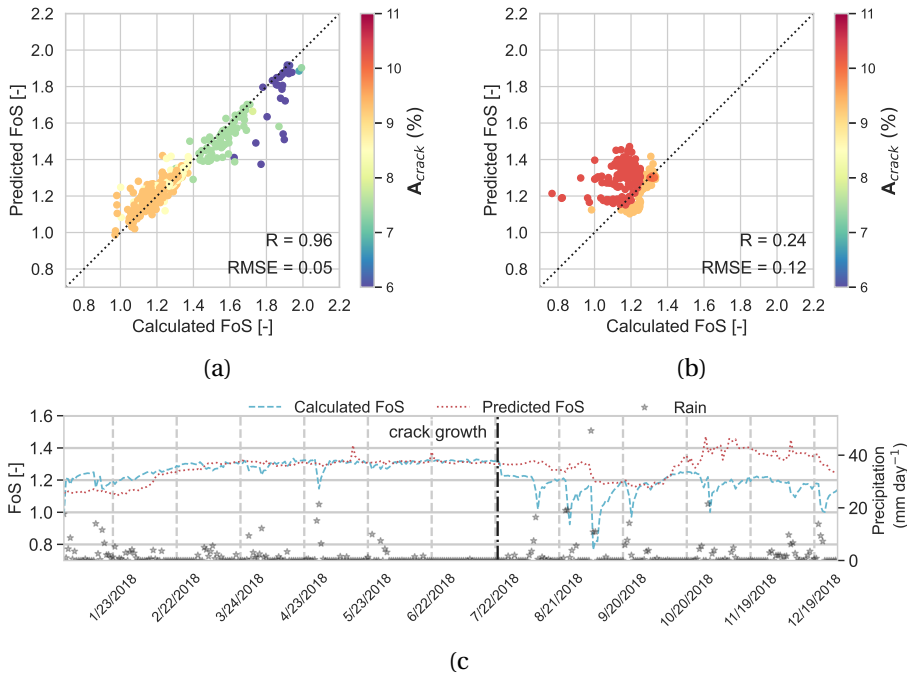


Figure 4.15: RF<sub>stp,5d</sub> model performance, over (a) the testing data set and (b) the independent data set, and (c) time series of predicted and calculated FoS in the independent data set (year 2018).

Table 4.5: Summary of RF models performance on all datasets

Scenarios		training		testing		evaluation	
		R	RMSE	R	RMSE	R	RMSE
Real-time assessment	observable features (5 features)	0.99	0.01	0.96	0.05	0.31	0.1
	observable features (6 features)	0.99	0.01	0.98	0.05	0.32	0.1
	observable and crack area as features	1	0.01	0.98	0.03	0.56	0.07
Short-term prediction	observable features (15 days lag)	0.99	0.01	0.94	0.06	0.06	0.14
	observable and crack area as features (15 days lag)	0.99	0.01	0.98	0.04	0.44	0.08
	observable features (5 days lag)	0.99	0.01	0.96	0.05	0.24	0.12

minimum and maximum values of the build RF models seen in the training set. In the evaluation data set RF cannot, therefore, predict the minimum FoS values of the whole

timeseries (2009–2018) that occurred after the training data set where the maximum  $A_{crack}$  occurs. To overcome this limitation, other algorithms can be used, e.g., deep learning, or combining predictors using stacking (Pedregosa *et al.*, 2011). An alternative could be to undertake more numerical simulations of potential future scenarios to allow the RF regressor to ‘see’ potential future results. This research introduces that using a combination of EO data and predictive models can have a significant potential in the context of dike monitoring. This helps dike managers to be able to undertake real-time assessment and short-term predictions.

#### 4.4. CONCLUSION

This proof-of-concept study investigates the potential use of observable data in predicting temporal changes in slope stability due to climatic forcing and includes the impact of vegetation and surface cracking. This study focused on making an ML-based surrogate for an FEM model. The underlying assumption is that the FEM model can emulate reality. Therefore, the validation against the ground truth data should be first reflected in the FEM model evaluation. Using such an approach can provide experts with a monitoring tool where they can assess a significant length of dikes relatively easily. A random forest machine learning approach was adopted, with features used in the model (*LAI*, surface displacement, cumulative rainfall and temperature) selected based on correlations with the FoS and that were potentially observable using satellite earth observation. This has advantages over using other features which require on-site investigation or the installation of permanent sensors. The results from the predictive model used in this study show that displacement has the highest feature importance for both cases of real-time assessment and short term prediction. It is recognised that, for other situations, slightly different features may be required. The approach resulted in an accurate prediction of the temporal FoS before new cracking events for the example dike. Over the ‘unseen’ data and after a crack expansion, the model performance is weak, as an RF model cannot extrapolate results and estimation is bound to the range of data over which the model has been trained. The results of this study show the potential use of EO data for real-time assessment and short-term prediction of an example dike condition. This method shows the potential of predictive models to support the assessment of a dike condition (stability), but not to replace more in-depth geotechnical site investigation and analysis.

## REFERENCES

- Ada, M. & San, B. T. (2018). Comparison of machine-learning techniques for landslide susceptibility mapping using two-level random sampling (2LRS) in Alakir catchment area, Antalya, Turkey. *Natural Hazards* **90**, No. 1, 237–263, doi:10.1007/s11069-017-3043-8.
- Baum, R. L., Godt, J. W. & Savage, W. Z. (2010). Estimating the timing and location of shallow rainfall-induced landslides using a model for transient, unsaturated infiltration. *Journal of Geophysical Research: Earth Surface* **115**, F3013, doi:10.1029/2009JF001321.
- Bouman, B. A. M., Schapendonk, A. H. C. M., Stol, W. & van Kraalingen, D. W. G. (1996). Description of LINGRA, a model approach to evaluate potential productivities of grasslands in different European climate regions. *Quantitative Approaches in System Analysis* **7**, 11–58.
- Breiman, L. (2001). Random forests. *Machine Learning* **45**, No. 1, 5–32.
- Breiman, L., Friedman, J., Stone, C. J. & Olshen, R. A. (1984). *Classification and regression trees*. CRC Press.
- Carlà, T., Intrieri, E., Raspini, F., Bardi, F., Farina, P., Ferretti, A., Colombo, D., Novali, F. & Casagli, N. (2019). Perspectives on the prediction of catastrophic slope failures from satellite InSAR. *Scientific Reports* **9**, No. 1, 14137, doi:10.1038/s41598-019-50792-y.
- Chakraborty, A. & Goswami, D. D. (2017). Slope stability prediction using artificial neural network (ANN). *International Journal of Engineering and Computer Science* **6**, No. 6, doi:10.18535/ijecs/v6i6.49.
- Chen, W., Pourghasemi, H. R., Kornejady, A. & Zhang, N. (2017). Landslide spatial modeling: Introducing new ensembles of ANN, MaxEnt, and SVM machine learning techniques. *Geoderma* **305**, 314 – 327, doi:10.1016/j.geoderma.2017.06.020.
- CIRIA (2013). *The International Levee Handbook*. London, UK: CIRIA (Construction Industry Research and Information Association), MEDE (Ministère de l'Ecologie du Développement durable et de l'Energie) and USACE (US Army Corps of Engineers).
- Conte, E., Donato, A., Pugliese, L. & Troncone, A. (2018). Analysis of the maierato landslide (Calabria, Southern Italy). *Landslides* **15**, No. 10, 1935–1950, doi:10.1007/s10346-018-0997-x.
- Conte, E. & Troncone, A. (2011). Analytical method for predicting the mobility of slow-moving landslides owing to groundwater fluctuations. *Journal of geotechnical and geoenvironmental engineering* **137**, No. 8, 777–784, doi:10.1061/(ASCE)GT.1943-5606.0000486.
- Conte, E. & Troncone, A. (2012). Stability analysis of infinite clayey slopes subjected to pore pressure changes. *Géotechnique* **62**, No. 1, 87–91, doi:10.1680/geot.10.T.002.
- Cundill, S. (2016). *Investigation of remote sensing for dike inspection*. Ph.D. thesis, University of Twente, doi:10.3990/1.9789036540360.



- de Gast, T., Hicks, M. A., van den Eijnden, A. P. & Vardon, P. J. (2020). On the reliability assessment of a controlled dyke failure. *Géotechnique Ahead of Print*, 1–16, doi:10.1680/jgeot.19.SiP.003.
- de Vries, G. (2012). Monitoring droogteonderzoek veenkaden. *Technical report*, Deltares, Delft, the Netherlands (in Dutch).
- Entekhabi, D., Yueh, S., O'Neill, P. E., Kellogg, K. H., Allen, A., Bindlish, R., Brown, M., Chan, S., Colliander, A., Crow, W. T. *et al.* (2014). *SMAP handbook. Soil moisture active passive: Mapping soil moisture and freeze/thaw from space*. JPL Publication; Pasadena, CA., USA.
- ESA (2020). User Guid, Sentinel-1. URL <https://sentinel.esa.int/web/sentinel/user-guides/sentinel-1-sar/revisit-and-coverage>.
- Ferretti, A., Prati, C. & Rocca, F. (2001). Permanent scatterers in SAR interferometry. *IEEE Transactions on Geoscience and Remote Sensing* **39**, No. 1, 8–20, doi:10.1109/36.898661.
- Goetz, J. N., Brenning, A., Petschko, H. & Leopold, P. (2015). Evaluating machine learning and statistical prediction techniques for landslide susceptibility modeling. *Computers & Geosciences* **81**, 1–11, doi:10.1016/j.cageo.2015.04.007.
- Hanssen, R. F. (2001). *Radar interferometry: Data interpretation and error analysis*, vol. 2. Springer Science & Business Media, doi:10.1007/0-306-47633-9.
- Hartke, S. (2019). *Accounting for satellite precipitation uncertainty: The development of a probabilistic landslide hazard nowcasting system*. Master's thesis, University of Wisconsin-Madison.
- Hastie, T., Tibshirani, R. & Friedman, J. (2009). *The elements of statistical learning: data mining, inference, and prediction*. Springer Science & Business Media, doi:10.1007/b94608.
- Hojat, A., Arosio, D., Ivanov, V. I., Loke, M. H., Longoni, L., Papini, M., Tresoldi, G. & Zanzi, L. (2020). Quantifying seasonal 3D effects for a permanent electrical resistivity tomography monitoring system along the embankment of an irrigation canal. *Near Surface Geophysics* **18**, No. 4, 427–443, doi:10.1002/nsg.12110.
- Jamalinia, E., Tehrani, F. S., Steele-Dunne, S. C. & Vardon, P. J. (2020a). Predicting rainfall induced slope stability using ensemble machine learning. In *Understanding and Reducing Landslide Disaster Risk*, vol. 5, WLFO, pp. 223–229, doi:10.1007/978-3-030-60713-5\_24.
- Jamalinia, E., Tehrani, F. S., Steele-Dunne, S. C. & Vardon, P. J. (2021). A data-driven surrogate approach for the temporal stability forecasting of vegetation covered dikes. *Water* **13**, No. 1, 107, doi:10.3390/w13010107.
- Jamalinia, E., Vardon, P. & Steele-Dunne, S. (2020b). Use of displacement as a proxy for dike safety. In *Proceedings of the International Association of Hydrological Sciences (IAHS)*, vol. 382, pp. 481–485, doi:10.5194/piahs-382-481-2020.

- Jia, G., Tang, Q. & Xu, X. (2020). Evaluating the performances of satellite-based rainfall data for global rainfall-induced landslide warnings. *Landslides* **17**, 283 – 299, doi:10.1007/s10346-019-01277-6.
- Kirschbaum, D. & Stanley, T. (2018). Satellite-based assessment of rainfall-triggered landslide hazard for situational awareness. *Earth's Future* **6**, 505–523, doi:10.1002/2017EF000715.
- Kirschbaum, D. B., Stanley, T. & Simmons, J. (2015). A dynamic landslide hazard assessment system for Central America and Hispaniola. *Natural Hazards & Earth System Sciences* **15**, No. 10, doi:10.5194/nhess-15-2257-2015.
- Li, J. & Zhang, L. (2010). Geometric parameters and REV of a crack network in soil. *Computers and Geotechnics* **37**, No. 4, 466 – 475, doi:10.1016/j.compgeo.2010.01.006.
- Lin, Y., Zhou, K. & Li, J. (2018). Prediction of slope stability using four supervised learning methods. *IEEE Access* **6**, 31169–31179, doi:10.1109/ACCESS.2018.2843787.
- Mokarram, M. & Zarei, A. R. (2018). Landslide susceptibility mapping using Fuzzy-AHP. *Geotechnical and Geological Engineering* **36**, No. 6, 3931–3943, doi:10.1007/s10706-018-0583-y.
- Ozer, I. (2020). *Understanding levee failures from historical and satellite observations*. Ph.D. thesis, Delft University of Technology, doi:10.4233/uuid:98e1ef84-91d0-4ee0-b37b-d7ab794cb367.
- Pedregosa, F., Varoquaux, G., Gramfort, A., Michel, V., Thirion, B., Grisel, O., Blondel, M., Prettenhofer, P., Weiss, R., Dubourg, V., Vanderplas, J., Passos, A., Cournapeau, D., Brucher, M., Perrot, M. & Duchesnay, E. (2011). Scikit-learn: Machine learning in Python. *Journal of Machine Learning Research* **12**, 2825–2830, doi:10.5555/1953048.2078195.
- Pei, H., Zhang, S., Borana, L., Zhao, Y. & Yin, J. (2019). Slope stability analysis based on real-time displacement measurements. *Measurement* **131**, 686–693, doi:10.1016/j.measurement.2018.09.019.
- Plaxis BV (2018). PLAXIS Reference Manual 2018. *Technical report*, Delft, the Netherlands.
- Pourghasemi, H. R. & Rahmati, O. (2018). Prediction of the landslide susceptibility: Which algorithm, which precision? *Catena* **162**, 177–192, doi:10.1016/j.catena.2017.11.022.
- Pourghasemi, H. R., Yansari, Z. T., Panagos, P. & Pradhan, B. (2018). Analysis and evaluation of landslide susceptibility: a review on articles published during 2005–2016 (periods of 2005–2012 and 2013–2016). *Arabian Journal of Geosciences* **11**, No. 9, 193, doi:10.1007/s12517-018-3531-5.
- Pradhan, B. (2013). A comparative study on the predictive ability of the decision tree, support vector machine and neuro-fuzzy models in landslide susceptibility mapping using GIS. *Computers and Geosciences* **51**, 350 – 365, doi:10.1016/j.cageo.2012.08.023.

- Probst, P., Wright, M. N. & Boulesteix, A.-L. (2019). Hyperparameters and tuning strategies for random forest. *Wiley Interdisciplinary Reviews: Data Mining and Knowledge Discovery* **9**, No. 3, e1301, doi:10.1002/widm.1301.
- Qi, C. & Tang, X. (2018). Slope stability prediction using integrated metaheuristic and machine learning approaches: A comparative study. *Computers & Industrial Engineering* **118**, 112–122, doi:10.1016/j.cie.2018.02.028.
- Raja, N. B., Çiçek, I., Türkoğlu, N., Aydın, O. & Kawasaki, A. (2017). Landslide susceptibility mapping of the sera river basin using logistic regression model. *Natural Hazards* **85**, No. 3, 1323–1346, doi:10.1007/s11069-016-2591-7.
- Reichenbach, P., Rossi, M., Malamud, B. D., Mihir, M. & Guzzetti, F. (2018). A review of statistically-based landslide susceptibility models. *Earth-Science Reviews* **180**, 60–91, doi:10.1016/j.earscirev.2018.03.001.
- Rossi, M., Kirschbaum, D., Luciani, S., Mondini, A. C. & Guzzetti, F. (2012). TRMM satellite rainfall estimates for landslide early warning in Italy: preliminary results. In *Remote Sensing of the Atmosphere, Clouds, and Precipitation IV*, vol. 8523, International Society for Optics and Photonics, p. 85230D, doi:10.1117/12.979672.
- Segoni, S., Lagomarsino, D., Fanti, R., Moretti, S. & Casagli, N. (2015). Integration of rainfall thresholds and susceptibility maps in the Emilia Romagna (Italy) regional-scale landslide warning system. *Landslides* **12**, No. 4, 773–785, doi:10.1007/s10346-014-0502-0.
- Steger, S., Brenning, A., Bell, R., Petschko, H. & Glade, T. (2016). Exploring discrepancies between quantitative validation results and the geomorphic plausibility of statistical landslide susceptibility maps. *Geomorphology* **262**, 8–23, doi:10.1016/j.geomorph.2016.03.015.
- Stone, M. (1974). Cross-validatory choice and assessment of statistical predictions. *Journal of the Royal Statistical Society: Series B (Methodological)* **36**, No. 2, 111–133.
- Tien Bui, D., Tuan, T. A., Klempe, H., Pradhan, B. & Revhaug, I. (2016). Spatial prediction models for shallow landslide hazards: a comparative assessment of the efficacy of support vector machines, artificial neural networks, kernel logistic regression, and logistic model tree. *Landslides* **13**, No. 2, 361–378, doi:10.1007/s10346-015-0557-6.
- van Baars, S. (2005). The horizontal failure mechanism of the Wilnis peat dyke. *Géotechnique* **55**, No. 4, 319–323, doi:10.1680/geot.2005.55.4.319.
- Verikas, A., Vaiciukynas, E., Gelzinis, A., Parker, J. & Olsson, M. C. (2016). Electromyographic patterns during golf swing: Activation sequence profiling and prediction of shot effectiveness. *Sensors* **16**, No. 4, 592, doi:10.3390/s16040592.
- Wei, X., Zhang, L., Yang, H.-Q., Zhang, L. & Yao, Y.-P. (2021). Machine learning for pore-water pressure time-series prediction: Application of recurrent neural networks. *Geoscience Frontiers* **12**, 453–467, doi:10.1016/j.gsf.2020.04.011.

- Yilmaz, I. (2010). Comparison of landslide susceptibility mapping methodologies for koyulhisar, turkey: conditional probability, logistic regression, artificial neural networks, and support vector machine. *Environmental Earth Sciences* **61**, No. 4, 821–836, doi: 10.1007/s12665-009-0394-9.
- Youssef, A. M., Pourghasemi, H. R., Pourtaghi, Z. S. & Al-Katheeri, M. M. (2016). Landslide susceptibility mapping using random forest, boosted regression tree, classification and regression tree, and general linear models and comparison of their performance at Wadi Tayyah Basin, Asir Region, Saudi Arabia. *Landslides* **13**, No. 5, 839–856, doi: 10.1007/s10346-015-0614-1.
- Zhou, J., Li, E., Wei, H., Li, C., Qiao, Q. & Armaghani, D. J. (2019). Random forests and cubist algorithms for predicting shear strengths of rockfill materials. *Applied Sciences* **9**, No. 8, 1621, doi:10.3390/app9081621.



# 5

## POTENTIAL VALUE OF REMOTE SENSING FOR DIKE INSPECTION

*Assessing slope conditions and risk management is often hindered by lack of data. In the Netherlands, dike managers typically assess the condition of a dike by walking along a dike, which is costly and infrequent. Remote Sensing (RS) can provide experts with a frequent large-scale monitoring tool with high spatial resolution. This chapter discusses the possibility of using the available RS data to monitor condition of regional dikes in the Netherlands. Vegetation condition and surface displacement of an example regional dike are extracted from publicly available RS data. The time series of those data is shown to be suitable to aid dike managers to detect anomalies and weak spots along a dike, that can be used to inform further investigation.*

## 5.1. INTRODUCTION

THE integrity and reliability of earthen flood control infrastructure are essential to ensure safe residential, industrial and commercial activities. Structural health and cover quality monitoring and reliability-updating based on performance observations contribute to a better dike condition assessment (Jonkman *et al.*, 2018). In the Netherlands, the inspection methods rely largely on expert observers, who walk along a dike to record the condition, guided partially by static data, e.g. the material used to construct the dike. For example, the cover quality assessment was reported to be done twice a year for secondary dikes by a specific waterboard (Chapter 2). These time consuming observations are infrequent, subjective, qualitative and expensive which can be improved by Remote Sensing (RS) data. In Chapter 4 it is argued that remote monitoring of slopes could provide valuable information about their performance under various climate driving forces conditions. RS methods include active and passive sensors. Active sensors are LiDAR and Radar, while passive sensors includes optical RS that can be implemented using aerial photography (e.g. drones) and satellite imagery. In this work, the emphasis is on satellite imagery and in the following sections RS refers to monitoring dikes from space.

The availability of satellite data provides fine spatial resolution with high revisit times that enables real-time monitoring of earthen flood-control structures, such as dikes. Compared to manual observation, where data are collected at irregular time intervals (or even not at all), RS can allow for a more accurate and objective characterisation of slope status and behaviour. Manual collection of ground data provides information at infrequent intervals and at a limited number of locations, whereas remote sensing provides increased spatial and temporal coverage (Dunbar *et al.*, 2017).

Chapter 4 and recent studies (e.g. Hasan *et al.*, 2013), have highlighted the potential of using ‘Vegetation Indices’ (VIs) from RS data as a tool to assess the slope condition. The Copernicus program introduced by European Space Agency (ESA) provides a unified system of satellites named Sentinels through which vast amounts of open access RS data are provided to monitor the globe (Copernicus, 2021). For instance, displacements and cover quality of slopes prior or after a failure were monitored using Sentinel data in recent studies (Bonforte & Guglielmino, 2015; Intrieri *et al.*, 2018; Kim & Lee, 2020; F Gama *et al.*, 2020; Yang *et al.*, 2019b).

The Netherlands Space Office (NSO, 2020) also purchases commercial satellite imagery which cover the Netherlands until at least the end of 2023, and makes them publicly available (open access) to complement the range of open data available from the various space agencies. Collectively, these data provide a great opportunity for managers to monitor Dutch dikes.

The purpose of monitoring slopes is to measure changes in relevant parameters as indicators for slope failure, slope deterioration through time, and/or provide early warning capabilities, as well as providing valuable input data for regular assessments. In geotechnical applications, parameters of interest in monitoring typically include water table elevation, movement of water through soil, displacements, water pressures, temperature changes, or detection of voids and conduits within slopes (Dunbar *et al.*, 2017). In the previous chapters, results of numerical simulation showed that surface displacement and Leaf Area Index are highly correlated with the Factor of Safety (FoS) of an example dike

under climatic driving forces and that these parameters had the potential to be monitored by observing the dike surface.

This chapter provides an overview of the state-of-the-art in using RS for dikes monitoring, as a method of complementing or partially replacing existing monitoring approaches and assessment. The potential use of RS for slope monitoring, using the link between measurable parameters and FoS is discussed in the next sections. In particular, the potential of RS to provide data with sufficient spatial and temporal resolution is investigated. After a brief introduction to relevant remote sensing techniques, some examples of Sentinel imagery will be presented, and temporal data of Leaf Area Index (*LAI*) and displacement for an example regional dike will be shown and discussed.

## 5.2. VEGETATION MONITORING

Vegetation influences the water balance in the root zone, through rainfall, evapotranspiration and leaf interception, and thereby can highly influence the stability of slopes. Moreover, roots can mechanically reinforce soil and increase shear strength of soil compounded by increasing the matrix suction (CIRIA, 2013). In addition, vegetation responds to climatic conditions (as well as maintenance actions), and therefore, can provide a proxy sensor for (recent) past climatic conditions and the current dike (internal) conditions. In general, vegetation sparsity can be considered as an indicator of an increase in the susceptibility of slope instability (Chapter 3). In the Netherlands, vegetation is one of the factors that dike inspectors evaluate in their ground-based observation (Digigids, 2019). The vegetation quality for each location is assessed and classified as good, medium, poor or bad (Cundill, 2016). However, these definitions are neither well defined nor specific. Using RS can facilitate large-scale monitoring to map vegetation cover. Anomalies in RS data products could provide a more objective and quantitative indicator for experts to evaluate cover quality status. For example, it is shown in Chapter 3 that the variation of the grass *LAI* over cracked areas is lower in the growing season, specifically after mowing events, than in non-cracked areas. Hasan *et al.* (2013) used satellite data to show that grass growing over the cracked areas were stressed due to a lack of moisture compared to healthy areas. This argument was corroborated by the numerical results using the integrated crop-geotechnical model developed in Chapter 3. In cracked areas, more evaporation occurs from the exposed root zone which leads to the lower available water for vegetation to grow, causing water-stressed vegetation, and therefore lower *LAI*. In stressed vegetation, the ratio between area of leaves over area of ground decreases.

*LAI* is typically estimated using optical RS imagery. Satellite-derived *LAI* products provide observations of seasonal and inter-annual vegetation growth in response to climate forcing. The basic assumption behind the development and use of remotely-sensed VIs is that some algebraic combination of reflectance in different spectral bands can reveal valuable information of dynamic vegetation variations (Yengoh *et al.*, 2015). Vegetation cover is often monitored in terms of *LAI*, i.e., the area of the leaves over area of the ground. *LAI* was used in the numerical simulations and the results are shown in Chapters 2 and 3. However, remotely sensed *LAI* are empirically estimated from VIs like *NDVI* (Fan *et al.*, 2009; Punalekar *et al.*, 2018). The Normalized Difference Vegetation Index (*NDVI*) quantifies vegetation health/vitality by measuring the difference between near-infrared light (*NIR*), which is strongly reflected by vegetation, and red (visible) light



(*RED*), which is strongly absorbed by vegetation. *NDVI* is calculated per pixel of an image as a function of the red and near infrared bands:

$$NDVI = \frac{NIR - RED}{NIR + RED} \quad (5.1)$$

Healthy, active vegetation has low red light reflectance and high near infrared reflectance that produce high *NDVI* values. When the available water in the vegetation is low, the *NDVI* is lower (in bare soil *NDVI* is zero) (Choubin *et al.*, 2019).

The availability of the optical VI products varies in space and time as a result of how frequently satellites pass over the area, and spatial and seasonal variations in cloud cover. Regions with significant cloud cover, like the Netherlands, are often unable to acquire timely satellite imagery. Van der Wal *et al.* (2013) used 20 years of climate data from a Royal Netherlands Meteorological Institute (KNMI) weather station data at Eelde (the Netherlands) to show that satellite optical images have a 20% probability of producing an adequate image during the growing season. In Fig. 5.1, optical imagery for the same area is shown in a cloud-free condition and a cloudy day (5 days later). These optical images from Sentinel-2 illustrate that on cloudy days, it is impossible to retrieve optical VIs. Radar RS can also be used for vegetation monitoring without the limitation on weather condition, but it is beyond the scope of the current study.



(a)



(b)

Figure 5.1: Optical imagery from Sentinel-2 on (a) 15th July 2018, cloud free; (b) 20th July 2018, cloud covers the area.

A list of optical images that are available on the NSO portal (NSO, 2020) for the Netherlands, with some of their specifications, is shown in Table 5.1. According to this table, the highest spatial resolution is 2 m which is very promising for monitoring cover quality over dikes but the temporal availability of this fine resolution data is usually for every 6 weeks of the growing season. Coarse resolution optical data (10 m spatial resolution) are available every 5 days. However this availability is based on cloud free conditions. Obviously, on the cloudy days monitoring is not possible.

Table 5.1: Recent optical (multispectral) data on the Dutch satellite data portal (NSO, 2020).

<b>Project</b>	<b>Country</b>	<b>Highest Res.</b>	<b>Available period in NSO website</b>	<b>Swath width</b> <sup>a</sup>
SuperView	China (SpaceView)	2 m	2019 - now, every 6 weeks in the period Mar - Oct	12 km
TripletSat	China (21AT)	3.2 m	2017 - 2018, up to every 6 weeks in the period Mar - Oct	24 km
PlanetScope	USA (Planet)	3.1 m	2017 - 2018, every 2 weeks from Mar- mid Sep	24.6 km
RapidEye	USA (Planet)	5 m	2017, every 2 weeks during the growing season of 2017	77 km
SPOT-6&7	France (Airbus)	6 m	2014 - 2016, every month	60 km
Sentinel-2a&b	Europe (ESA)	10 m	2015 - now, every 5 days <sup>b</sup>	290 km

<sup>a</sup>The area on the Earth's surface that the mounted sensor on a satellite captures (sees).<sup>b</sup>Please note that the temporal resolution is for the cloud free condition.

## 5.3. DEFORMATION MONITORING

Swelling-shrinking phenomena in soils (in particular clays and peats) are associated with changes of moisture content which can be driven by climatic conditions. In particular, both a succession of dry periods and intense rainfall, can be responsible for dike failures (van Baars, 2005; Tohari *et al.*, 2007; Andrieux *et al.*, 2011; Wang *et al.*, 2018). Changes in moisture content lead to changes in pore water pressure, and subsequently changes in effective stresses leading to soil deformation and dike displacements. Wetting a soil in a dike, generally increases the pore water pressure, decreasing the effective stresses and therefore also decreasing the strength, making the dike less stable. In addition, increasing the water content increases the weight, which increases the shear stresses, also making the dike less stable.

Drying a soil in a dike, generally decreases the pore water pressure which increases effective stresses and strength, and decreases the weight and therefore the shear stresses. In cases when the strength is largely determined by friction, e.g. in peats, the shear strength can decrease. In shrinking soils, volume changes due to water content reduction can result in the appearance of shrinkage cracks and surface subsidence (Cornelis *et al.*, 2006; Vardon, 2015). The cause of soil drying is a thermodynamic imbalance between the soil moisture and its surroundings. This then causes evaporation and a consequential fluid movement within the soil (Driebergen, 2019). Cracks provide preferential flow, which significantly increases the hydraulic conductivity and, after rainfall, also pore water pressures in the soil (Zhang *et al.*, 2018). As a result, the shear strength of the soil decreases, thereby can induce slope instability. As discussed in Chapter 3, desiccation cracks on the soil surface can cause rapid rainfall infiltration, leading to increases in pore pressures within the dike body. Therefore, soil shrinkage behavior and desiccation cracking (followed by rainfall) can lead to more significant instabilities in dikes.

These displacements of a dike surface can be measured by in-situ measurements, e.g. extensimeters (de Vries, 2012), or by RS, which provides large scale information about a dike displacement. The Current Dutch Elevation (Actueel Hoogtebestand Nederland, AHN (AHN, 2020)) map is a digital elevation map of the whole of the Netherlands. This map is updated every few years. The latest version is AHN4 that was released in 2021. The AHN data are acquired by means of aerial LiDAR scanning, where laser pulses are sent from an aeroplane or helicopter, to measure the surface elevation (AHN, 2020). Although, the spatial resolution is suitable for dike monitoring, it is not possible to have a time series of data for a displacement over a dike, since it happens every few years. For instance AHN3 data were acquired during the period 2014-2018 for the whole country. Therefore, satellite monitoring using radar is very useful to measure the surface displacement, the method called InSAR which is discussed in the next section.

### 5.3.1. DEFORMATION MONITORING USING INSAR

Interferometric Synthetic Aperture Radar (InSAR) can be used to estimate the displacement on a dike surface (Hanssen, 2001). Synthetic Aperture Radar (SAR) is a microwave imaging technique, in which the motion of the platform (aircraft or satellite) is used to synthesise a large antenna. The radar system transmits multiple, successive pulses toward targeted objects on the earth and the returned signals are synthesised into a single image (Khorram *et al.*). Interferometric SAR (InSAR) is based on the interference of two

synthetic aperture radar (SAR) images, acquired from different positions or at different times (Esfahany, 2017). This technique has the potential to measure millimetre surface displacements along the radar Line-Of-Sight (LOS) direction (Ferretti *et al.*, 2006).

From 1992 to the present, SAR satellites have provided radar images for monitoring surface motion. ESA launched its first SAR instrument in 1991, on the ERS-1 (European Remote Sensing Satellite), which operated until 2000. In Table 5.2, some of the recent SAR satellites are listed. From this list, imagery from Sentinel-1 can be obtained through Copernicus. RadarSat-2 images are not generally free; however, NSO (2020) purchases some imagery over the Netherlands and distributes them via the Satellite Data Portal. Data from the Satellite Data Portal are expected to be available until at least March 2023.

Table 5.2: Recent space radar projects.

<b>Project</b>	<b>Type</b>	<b>Country</b>	<b>Band</b>	<b>Resolution (m)</b>	<b>Revisit</b>	<b>Launch Date</b>
TerraSAR	Public-Private	Germany (DLR)	X	3 × 3	11 days	2007
Sentinel-1	Government	Europe (ESA)	C	20 × 5	2-12 days	2014
Radarsat-2	Government	Canada	C	10 × 9	24 days	2018
ICEYE* <sup>a</sup>	Commercial	Finland	X	1 × 1	1 hour	2018
Capella*	Commercial	USA	X	0.5 × 0.5	1 hour	2020

<sup>a</sup>Satellites with \* are the ones that move above the desired area imagery is asked for.

### 5.3.2. INSAR TIME SERIES

Time series of displacement are very important for dike monitoring applications. Persistent Scatterer Interferometry (PSI) is an advanced InSAR method that use a temporal series of SAR images over the same area, and was first developed by [Ferretti \*et al.\* \(2001\)](#). Persistent Scatterers are pixels of SAR imagery that have objects with high reflectance to the satellite and are consistent in time, it means that the reflectance remains high in all SAR images for InSAR processing ([Pepe & Calò, 2017](#)). In fact, these objects reflect the most part of the signal received by SAR satellite from a pixel. PS points are commonly found on pixels containing structures like houses, bridges and roads. On the contrary, low reflectance over water or vegetation toward the satellite, means that there are no PS points in these pixels. Therefore, in case of dikes, on parts which covered with vegetation, no InSAR measurement can be obtained. This can be overcome by placing a metal corner reflectors in the study area to create persistent scatterers ([Yang \*et al.\*, 2019a](#)). For instance [Fig. 5.2](#) shows an InSAR map over an urban area next to agricultural fields. It can be seen that there are no InSAR points present on vegetated lands. Although there are studies about exploiting deformation data over vegetated fields ([Morishita & Hanssen, 2015](#)), currently there is no comprehensive method for generate it in all vegetated fields.

The rectangular box in [Fig. 5.2](#) shows the location of the Veenderij dike, where the geometry and weather station of KNMI near its location used in the previous chapters for numerical analysis. It can be seen that by using InSAR, no data can be obtained for the dike itself. This is most likely due to the coherence of scatters being very low due to vegetation. This grass-covered dike is located in an area where persistent scatterers cannot be found and therefore does not exhibit high radar coherence. However, artificial reflectors, e.g. corner reflectors, can be placed in areas where the coherence are weak, to generate persistent scatterers.

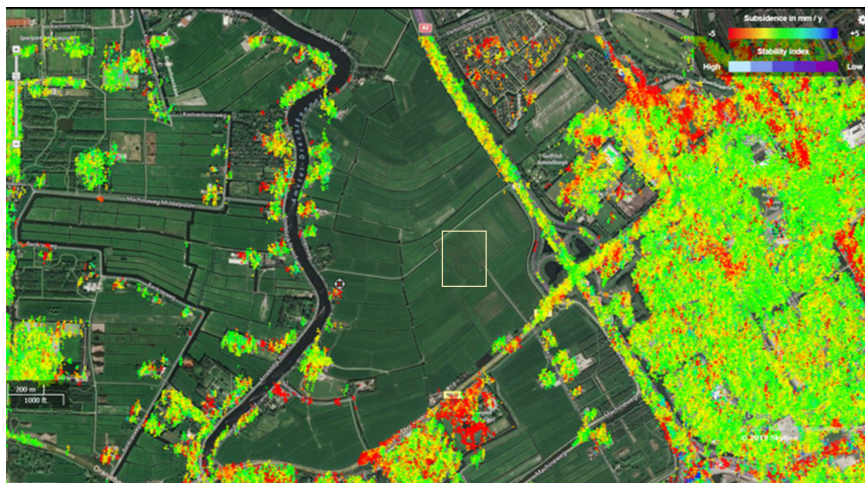


Figure 5.2: Available InSAR data for points from the Bodemdalingskaart ([Open surface and object motion map v2, 2020](#)) for an example area containing the Veenderij project.

PSI data processing and analysis procedures are required to separate the displacement

phase from the other phase components in SAR images. The data processing steps are: (i) first the Persistence Scatters candidate selected, these are points in a resolution cell that yields coherent reflectors. There are different methods to select the PSI candidate (for detailed information see [Ferretti et al., 2001](#); [Bovenga et al., 2002](#); [Humme, 2007](#)); (ii) Then, their interferometric phase is used to estimate the deformation phase; (iii) Finally the results obtained from PSI can be validated by GNSS (Global Navigation Satellite System) or field measurements ([Yalvac, 2020](#); [Aobpaet et al., 2013](#)). A detailed description of the processing approach of several PSI techniques can be found in [Ferretti et al. \(2001\)](#), [Kampes et al. \(2003\)](#), [Costantini et al. \(2009\)](#), [Ketelaar \(2009\)](#), [Van Leijen \(2014\)](#), and [Esfahany \(2017\)](#).

## 5.4. CASE STUDY

To illustrate the value of remote sensing data, some data have been extracted for a regional dike near Delft (Latitude: 51.97, Longitude: 4.38) that is located along a river canal, [Fig. 5.3](#). This dike was also studied in [Özer \(2020\)](#), and is used here as an example to show the application of RS data for monitoring dikes subject to climatic conditions. The considered dike, including the points at which displacement was determined, are shown on [Fig. 5.3](#) by the red line and three points, respectively. In this chapter, only data from Sentinel satellites are included because they are publicly available and are widely used.



Figure 5.3: An image of the case study regional dike segment near Delft. The figure is generated using Google Earth pro. A red line drawn along the area shows where vegetation is monitored; and points A, B and C represents the locations where displacements are measured.



### 5.4.1. VEGETATION CONDITION

*LAI* has been used in the numerical study in the previous chapters and the impact of vegetation status and *LAI* on the dike condition is discussed in Chapters 2 and 3. For *LAI* retrieval from the Sentinel-2 satellite (publicly free available data source), a rectangular polygon with the size of 3 km by 0.034 km over the dike has been selected. The selected length is long enough to include 3 InSAR points over the area. *NDVI* and *LAI* data retrieved from optical images that are acquired from a platform developed by VITO (Terrascope, 2020) on which Sentinel images are processed and time series data are ready to use interactively. Here, only optical images with cloud cover less than 10 % are included.

*NDVI* is calculated using the algorithm from TerraScope and plotted in Fig. 5.4(a). The Sentinel-2a & b satellites were launched in June 2015 and March 2017, respectively. Therefore, data acquisition starts from summer 2015, and the revisit time increases after spring 2017, which results in more frequent data from spring 2017 onwards. The seasonal cycle can be detected from this figure. Mostly in the growing seasons the *NDVI* increases and during the winter it decreases. To see how *NDVI* is shown from the satellite images, two images at two different days are selected from the Terrascope (2020) website on 25th June 2018 and 15th July 2018. The geometry that *NDVI* value for the dike is averaged over a black polygon shown by in Figs. 5.4(b) and (c). The area of the polygon is almost  $0.1 \text{ km}^2$ . For the shown polygon on Figs. 5.4(b) and (c) the color of the map changes from green (higher *NDVI*) on 25th June to yellow (lower *NDVI*) on 15th July. Please note that *NDVI* values over the area of the canal has negative values.

*LAI* is also calculated for the same region and the time series of *LAI* is plotted in Fig. 5.5. The data are available from Sentinel-2 at the same days that *NDVI* is calculated. As mentioned in Chapters 2 and 3, *LAI* has an annual cycle, it generally reduces in the autumn and stays at low values during winter periods and increases in spring and summer seasons as the grass grows. This pattern can be seen in Fig. 5.5(a). The mowing schedule for the secondary dike, once at mid-June and again in mid-August, also affects the *LAI* values. This leads to an abrupt decrease in *LAI* in mid-June and mid-August.

In Figs. 5.5(b) and (c), the maps of *LAI* for 25th June and 15th July 2018 are shown. There is a decrease shown in *LAI* from 25th June to 15th July 2018, this can be seen from the changing color in the drawn polygon from more green and yellow color to brownish color at the later period. According to the legend, *LAI* decreases as the color changes from the green to brown.

From Figs. 5.4(a) and 5.5(a), it can be seen that generally *NDVI* and *LAI* is lower in summer 2018 than other years. The summer of 2018 was very dry in the Netherlands and the impact of this dryness is apparent in the vegetation condition over the dike. In addition, comparing two dates in Figs. 5.4(b)-(c) and 5.5(b)-(c), it is shown that vegetation coverage is lower (consistent with being a bit drier) on 15th July compared to 25th June. However, be aware that most of the dike is a mixture of grass and road, so the reflectances from the surface are mixtures of a response from road path and vegetation. The information is still useful, as the difference in values between two dates at the same location is significant if the road condition remains constant.

According to Table 5.1, the resolution of the Sentinel-2 images are 10 m which could be sufficient to assess the average cover quality over a large area of a dike. However, this spatial resolution is not suitable to find small patches or cracks on a dike. Finer resolution

data could be obtained by flying a drone fitted with an optical sensor over the dikes, which would also circumvent the limitations posed by cloud cover.

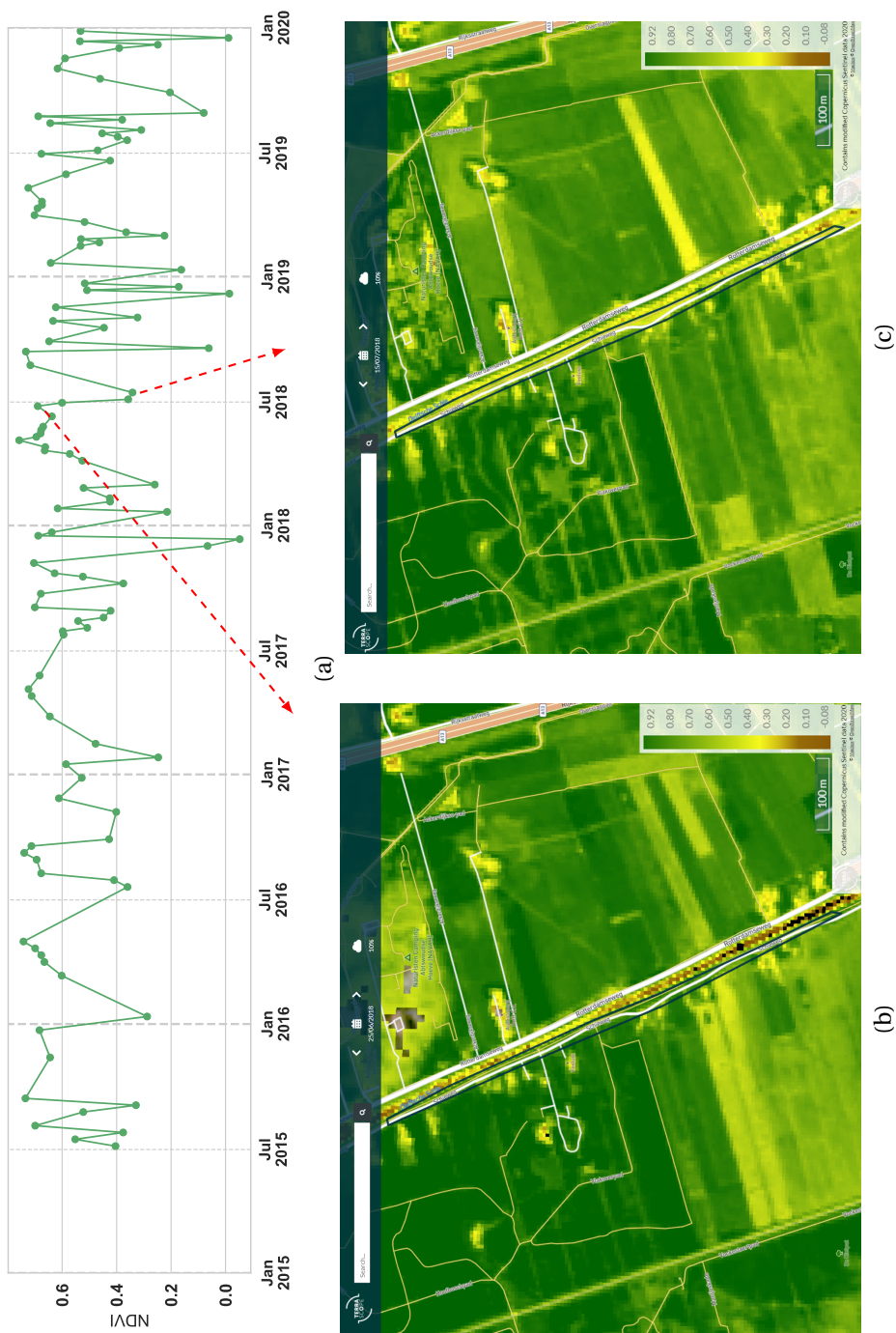


Figure 5.4: For the case study, data retrieved from Sentinel-2, (a) NDVI time series, NDVI map for two different days (b) 25th June 2018, (c) 15th July 2018.

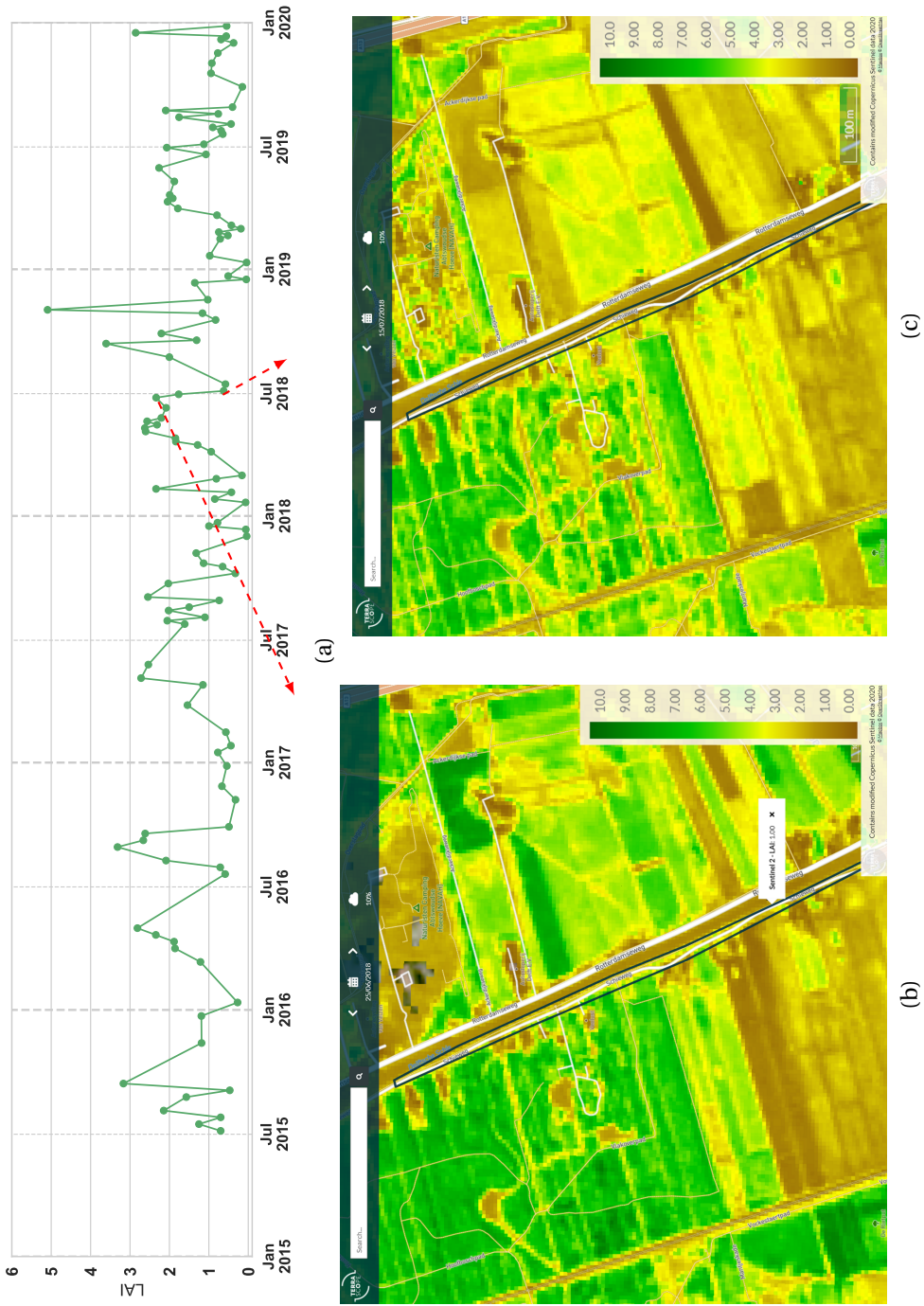


Figure 5.5: For the case study, data retrieved from Sentinel-2, (a) LAI time series, LAI map for two different days (b) 25th June 2018, (c) 15th July 2018.

### 5.4.2. DEFORMATION DATA FROM INSAR PROCESSING

The Netherlands Center for Geodesy and Geo-informatics (NCG, 2020), provides the [Open surface and object motion map v2 \(2020\)](#) that shows the displacement of more than 40 billion measurement points across the whole Netherlands. The deformation data for this map are obtained from InSAR method using Sentinel-1 images. In this section the data from this publicly available map will be used, where the point measurements are processed and can be used interactively.

The deformation data for three points over the dike in Delft was obtained from [Open surface and object motion map v2 \(2020\)](#), where displacement data are available for coherent points on the selected dike. These data are plotted in Fig. 5.7, for points A (Lat: 51.975, Lon: 4.383), B (Lat: 51.974, Lon: 4.384) and C (Lat: 51.970, Lon: 4.386) on Fig. 5.3. Fig. 5.6, shows these three points on the image of [Open surface and object motion map v2 \(2020\)](#), where by clicking on every points (here point B), the time series data (blue markers) and more information will be shown. The red line is the linear fit to the data which yields the rate of displacement per year. Again, it can be seen that over vegetated area there are no coherent points to retrieve the displacement. These data are obtained from Sentinel-1 a&b. It can be seen that the temporal resolution increased after spring 2016, after Sentinel-1b was launched. The rate of settlement is different along the dike, Point A settles with the velocity of 1 mm/year, the rate of settlement at Point B is 8.3 mm/year and at Point C it is 3.3 mm/year. These values are calculated based on a linear fit applied to the data, further details can be found in [Open surface and object motion map v2 \(2020\)](#). The difference in displacement velocity depends on various conditions including soil type, ground water level, etc. According to Özer (2020), the soil type of the dike at Point A and B is mostly clay and for point C is sand and clay. The shrinkage/swelling behaviour of soil can be seen in the three points. In summer, the soil settles and in the following winter it swells. The overall trend is a downwards displacement at all three points. This may be due to settlement of the whole dike, but all the parameters including the underlying geology should be considered before drawing a general conclusion.

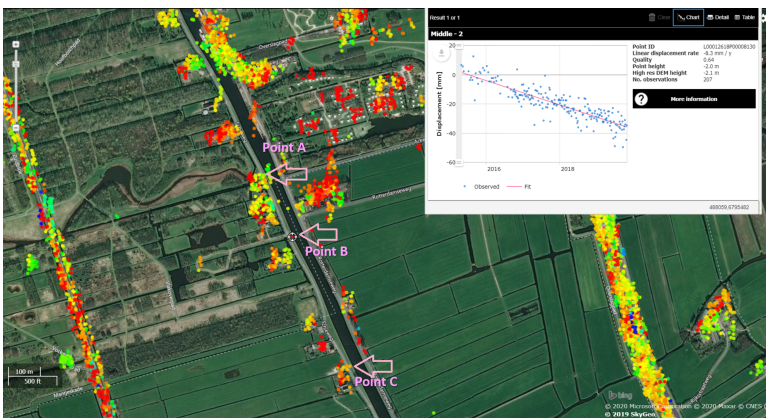


Figure 5.6: A screenshot from [Open surface and object motion map v2 \(2020\)](#), shows available InSAR data on the case study. The InSAR time series of points A, B and C are shown in Fig. 5.7.

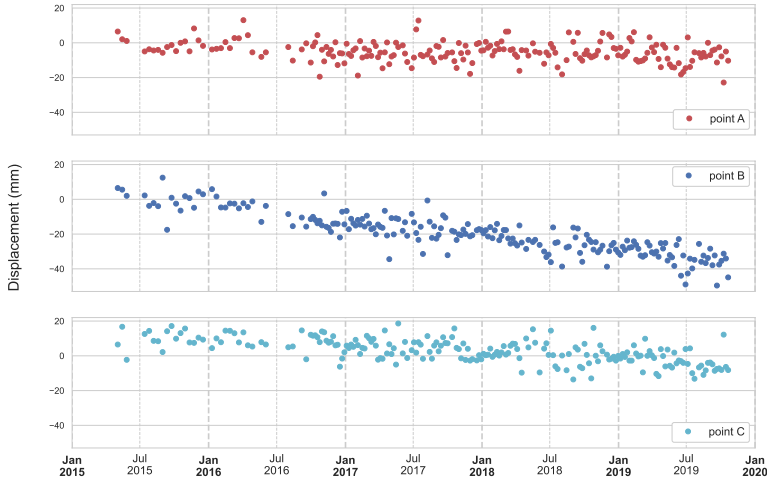


Figure 5.7: Deformation time series for three points on an example dike, data from [Open surface and object motion map v2 \(2020\)](#).

The measurements from [Open surface and object motion map v2 \(2020\)](#) can be a useful free source of data for PS points on a dike. However, it is important to note that data are not available for vegetated areas unless there is a persistent scatter such as a bike path/road or other object on the dike. Alternatively, Persistent Scatterers (e.g. corner reflectors) can be introduced at locations of interest.

Visual inspection of dike inspections is done in the Netherlands usually by walking along the dike. Observable components of the dike can assist to find weakness and damage. Remote sensing will provide dike observers with a promising tool to monitor vegetation cover quality and displacement of dikes. This chapter introduces RS as a tool that could increase efficiency, coverage and objectivity of dike inspections to find anomaly over the dike. In practice, *LAI* can be monitored and use as an input for the crop model, then the water balance in the root zone will be simulated based on the real *LAI* values. Having displacement measurements from RS also can be feed into stability models to estimate the safety of dikes. Besides, as mentioned in Chapter 4 RS data can be used in data-driven models to estimate the dike condition without the need to repeat numerical analysis.

## 5.5. CONCLUSION

Continuous dike monitoring is crucial to avoid flood defence failures. Traditionally, dikes are monitored by in-situ instruments, or by visual inspection (walking along the dikes) to detect weak or at-risk locations. These methods are expensive, difficult, localised, and only possible at certain times. However, remote sensing can be used to provide continuous useful information on vegetation condition and displacement on dikes at a large scale. This can be used to inform dike managers of locations that may warrant additional visual inspection. In this chapter, it has been argued that *LAI* and *NDVI* can

provide information on grass cover over an example dike. On cloudy days, optical data are not available. This limitation can be circumvented by mounting optical sensors on drones for occasional flights at key times, or by using data sources from techniques that are not limited by cloud cover e.g. SAR. The other important parameter that can be observed remotely is surface displacement over a dike. InSAR is a promising tool to measure deformation of PSI points on a dike with a mm level precision (Ferretti *et al.*, 2007). However, it is not possible to retrieve many PSI points over vegetated dikes. To solve this issue, fixed objects can be placed on the dike of interest, e.g. corner reflector. Monitoring dikes using remote sensing data will help dike managers with real-time assessment of dikes in the Netherlands, where some commercial satellites images are bought by the governments and are free to access.

## REFERENCES

- AHN (2020). Het actueel hoogtebestand Nederland (AHN). URL <https://www.ahn.nl/>.
- Andrieux, C., Chrétien, M., Denis, A., Fabre, R. & Lataste, J.-F. (2011). Shrinkage and swelling of clay soil: Comparison between laboratory and in situ measurements. *European journal of environmental and civil engineering* **15**, No. 5, 819–838, doi: 10.1080/19648189.2011.9693367.
- Aobpaet, A., Cuenca, M. C., Hooper, A. & Trisirisatayawong, I. (2013). InSAR time-series analysis of land subsidence in Bangkok, Thailand. *International Journal of Remote Sensing* **34**, No. 8, 2969–2982, doi:10.1080/01431161.2012.756596.
- Bonforte, A. & Guglielmino, F. (2015). Very shallow dyke intrusion and potential slope failure imaged by ground deformation: The 28 December 2014 eruption on Mount Etna. *Geophysical Research Letters* **42**, No. 8, 2727–2733, doi:10.1002/2015GL063462.
- Bovenga, F., Refice, A., Nutricato, R., Pasquariello, G. & De Carolis, G. (2002). Automated calibration of multi-temporal ERS SAR data. In *IEEE International Geoscience and Remote Sensing Symposium*, vol. 6, IEEE, pp. 3655–3657, doi:10.1109/IGARSS.2002.1027281.
- Choubin, B., Soleimani, F., Pirnia, A., Sajedi-Hosseini, F., Alilou, H., Rahmati, O., Melesse, A. M., Singh, V. P. & Shahabi, H. (2019). Chapter 17 - effects of drought on vegetative cover changes: Investigating spatiotemporal patterns. In *Extreme Hydrology and Climate Variability* (Melesse, A. M., Abtew, W. & Senay, G., eds.), Elsevier, pp. 213–222, doi:10.1016/B978-0-12-815998-9.00017-8.
- CIRIA (2013). *The International Levee Handbook*. London, UK: CIRIA (Construction Industry Research and Information Association), MEDE (Ministère de l'Ecologie du Développement durable et de l'Energie) and USACE (US Army Corps of Engineers).
- Copernicus (2021). Copernicus Open Access Hub. URL <https://scihub.copernicus.eu/>.
- Cornelis, W. M., Corluy, J., Medina, H., Díaz, J., Hartmann, R., Van Meirvenne, M. & Ruiz, M. E. (2006). Measuring and modelling the soil shrinkage characteristic curve. *Geoderma* **137**, No. 1-2, 179–191, doi:10.1016/j.geoderma.2006.08.022.
- Costantini, M., Falco, S., Malvarosa, F., Minati, F. & Trillo, F. (2009). Method of persistent scatterer pairs (PSP) and high resolution SAR interferometry. In *2009 IEEE International Geoscience and Remote Sensing Symposium*, vol. 3, IEEE, pp. III–904, doi:10.1109/IGARSS.2009.5417918.
- Cundill, S. (2016). *Investigation of remote sensing for dike inspection*. Ph.D. thesis, University of Twente, doi:10.3990/1.9789036540360.
- de Vries, G. (2012). Monitoring droogteonderzoek veenkaden. *Technical report*, Deltares, Delft, the Netherlands (in Dutch).



- Digigids (2019). Grasbekledingen. URL <http://digigids.hetwaterschapshuis.nl/index.php?album=Grasbekledingen-2019-/gras/bedekkingsgraad>.
- Driebergen, J. (2019). *The detection of deformation on vegetated dikes using InSAR*. Master's thesis, Delft University of Technology.
- Dunbar, J. B., Galan-Comas, G., Walshire, L. A., Wahl, R. E., Yule, D. E., Corcoran, M. K., Bufkin, A. L. & Llopis, J. M. L. (2017). Remote sensing and monitoring of earthen flood-control structures. *Technical report*, United States. Army. Corps of Engineers Engineer Research and Development Center (U.S.) Geotechnical and Structures Laboratory (U.S.), doi:10.21079/11681/22804.
- Esfahany, S. S. (2017). *Exploitation of distributed scatterers in synthetic aperture radar interferometry*. Ph.D. thesis, Delft University of Technology, doi:10.4233/uuid:22d46f1e-9061-46b0-9726-760c41404b6f.
- F. Gama, F. Mura, J. C., R. Paradella, W. & G. de Oliveira, C. (2020). Deformations prior to the Brumadinho dam collapse revealed by Sentinel-1 InSAR data using SBAS and PSI techniques. *Remote Sensing* **12**, No. 21, doi:10.3390/rs12213664.
- Fan, L., Gao, Y., Brück, H. & Bernhofer, Ch. (2009). Investigating the relationship between NDVI and LAI in semi-arid grassland in Inner Mongolia using in-situ measurements. *Theoretical and Applied Climatology* **95**, No. 1, 151–156, doi:10.1007/s00704-007-0369-2.
- Ferretti, A., Prati, C. & Rocca, F. (2001). Permanent scatterers in SAR interferometry. *IEEE Transactions on Geoscience and Remote Sensing* **39**, No. 1, 8–20, doi:10.1109/36.898661.
- Ferretti, A., Prati, C., Rocca, F. & Wasowski, J. (2006). Satellite interferometry for monitoring ground deformations in the urban environment. In *Proceedings 10th IAEG Congress*, pp. 100–110.
- Ferretti, A., Savio, G., Barzaghi, R., Borghi, A., Musazzi, S., Novali, F., Prati, C. & Rocca, F. (2007). Submillimeter accuracy of insar time series: Experimental validation. *IEEE Transactions on Geoscience and Remote Sensing* **45**, No. 5, 1142–1153, doi:10.1109/TGRS.2007.894440.
- Hanssen, R. F. (2001). *Radar interferometry: data interpretation and error analysis*, vol. 2. Springer Science & Business Media, doi:10.1007/0-306-47633-9.
- Hasan, K., Aanstoos, J. V. & Mahrooghy, M. (2013). Stressed vegetation identification by SAR time series as an indicator of slope instability in Mississippi river levee segments. In *Applied Imagery Pattern Recognition Workshop (AIPR): Sensing for Control and Augmentation*, IEEE, pp. 1–4, doi:10.1109/AIPR.2013.6749307.
- Humme, A. J. M. (2007). *Point density optimization for SAR interferometry: a study tested on salt mine areas*. Master's thesis, Delft University of Technology.

- Intrieri, E., Raspini, F., Fumagalli, A., Lu, P., Del Conte, S., Farina, P., Allievi, J., Ferretti, A. & Casagli, N. (2018). The Maoxian landslide as seen from space: detecting precursors of failure with Sentinel-1 data. *Landslides* **15**, No. 1, 123–133, doi: 10.1007/s10346-017-0915-7.
- Jonkman, S. N., Voortman, H. G., Klerk, W. J. & van Vuren, S. (2018). Developments in the management of flood defences and hydraulic infrastructure in the netherlands. *Structure and Infrastructure Engineering* **14**, No. 7, 895–910, doi:10.1080/15732479.2018.1441317.
- Kampes, B. M., Hanssen, R. F. & Perski, Z. (2003). Radar interferometry with public domain tools. In *Proceedings of FRINGE*, vol. 3, p. 2004ESASP:550E..10K.
- Ketelaar, V. B. H. G. (2009). *Satellite radar interferometry: Subsidence monitoring techniques*, vol. 14. Springer Science & Business Media, doi:10.1007/978-1-4020-9428-6.
- Khorram, S., Koch, F. H., van der Wiele, C. F. & Nelson, S. A. C. (????). *Remote Sensing*. Springer-Verlag New York, doi:10.1007/978-1-4614-3103-9.
- Kim, Y. & Lee, M.-J. (2020). Rapid change detection of flood affected area after collapse of the Laos Xe-Pian Xe-Namnoy Dam using Sentinel-1 GRD data. *Remote Sensing* **12**, No. 12, doi:10.3390/rs12121978.
- Morishita, Y. & Hanssen, R. F. (2015). Deformation parameter estimation in low coherence areas using a multisatellite InSAR approach. *IEEE Transactions on Geoscience and Remote Sensing* **53**, No. 8, 4275–4283.
- NCG (2020). Nederlands Centrum voor Geodesies en Geo-Informatica. URL <https://ncgeo.nl/index.php/en/>.
- NSO (2020). Netherlands Space Office- Satellietdataportaal. URL <https://satellietdataportaal.nl/>, Accessed: June 2020.
- Open surface and object motion map v2 (2020). Open surface and object motion map v2. URL <https://bodemdalingskaart.portal.skygeo.com/portal/bodemdalingskaart/u1/viewers/basic/>.
- Özer, I. E. (2020). *Understanding levee failures from historical and satellite observations*. Ph.D. thesis, Delft University of Technology, doi:10.4233/uuid:98e1ef84-91d0-4ee0-b37b-d7ab794cb367.
- Pepe, A. & Calò, F. (2017). A review of interferometric synthetic aperture RADAR (InSAR) multi-track approaches for the retrieval of Earth's surface displacements. *Applied Sciences* **7**, No. 12, 1264, doi:10.3390/app7121264.
- Punalekar, S., Verhoef, A., Quaife, T., Humphries, D., Bermingham, L. & Reynolds, C. (2018). Application of Sentinel-2A data for pasture biomass monitoring using a physically based radiative transfer model. *Remote Sensing of Environment* **218**, 207–220, doi: 10.1016/j.rse.2018.09.028.

- Terrascope (2020). URL <https://terrascope.be/nl>.
- Tohari, A., Nishigaki, M. & Komatsu, M. (2007). Laboratory rainfall-induced slope failure with moisture content measurement. *Journal of Geotechnical and Geoenvironmental Engineering* **133**, No. 5, 575–587, doi:10.1061/(ASCE)1090-0241(2007)133:5(575).
- van Baars, S. (2005). The horizontal failure mechanism of the Wilnis peat dyke. *Géotechnique* **55**, No. 4, 319–323, doi:10.1680/geot.2005.55.4.319.
- Van der Wal, T., Abma, B., Viguria, A., Prévinaire, E., Zarco-Tejada, P., Serruys, P., van Valkengoed, E. & van der Voet, P. (2013). Fieldcopter: unmanned aerial systems for crop monitoring services. In *Precision agriculture'13*, Springer, pp. 169–175, doi:10.3920/978-90-8686-778-3\_19.
- Van Leijen, F. J. (2014). *Persistent scatterer interferometry based on geodetic estimation theory*. Ph.D. thesis, Delft University of Technology, doi:10.4233/uuid:5dba48d7-ee26-4449-b674-caa8df93e71e.
- Vardon, P. J. (2015). Climatic influence on geotechnical infrastructure: a review. *Environmental Geotechnics* **2**, No. 3, 166–174, doi:10.1680/envgeo.13.00055.
- Wang, B., Vardon, P. J. & Hicks, M. A. (2018). Rainfall-induced slope collapse with coupled material point method. *Engineering Geology* **239**, 1–12, doi:10.1016/j.enggeo.2018.02.007.
- Yalvac, S. (2020). Validating InSAR-SBAS results by means of different GNSS analysis techniques in medium-and high-grade deformation areas. *Environmental Monitoring and Assessment* **192**, No. 2, 1–12.
- Yang, M., López-Dekker, P., Dheenathayalan, P., Liao, M. & Hanssen, R. F. (2019a). On the value of corner reflectors and surface models in InSAR precise point positioning. *ISPRS Journal of Photogrammetry and Remote Sensing* **158**, 113–122, doi:10.1016/j.isprsjprs.2019.10.006.
- Yang, W., Wang, Y., Sun, S., Wang, Y. & Ma, C. (2019b). Using Sentinel-2 time series to detect slope movement before the Jinsha River landslide. *Landslides* **16**, No. 7, 1313–1324, doi:10.1007/s10346-019-01178-8.
- Yengoh, G. T., Dent, D., Olsson, L., Tengberg, A. E. & Tucker III, C. J. (2015). *Use of the Normalized Difference Vegetation Index (NDVI) to Assess Land Degradation at Multiple Scales: current status, future trends, and practical considerations*. doi: 10.1007/978-3-319-24112-8.
- Zhang, L., Li, J., Li, X., Zhang, J. & Zhu, H. (2018). *Rainfall-Induced Soil Slope Failure*. CRC Press, doi:10.1201/b20116.

# 6

## CONCLUSION AND DISCUSSION

## 6.1. CONCLUSION

THE overall idea of this research is to contribute towards improving the current monitoring and assessment of dikes in the Netherlands, by first understanding the behaviour and stability of regional dikes under various climate and vegetation condition and secondly, using technology and methods which can enable real-time monitoring and assessment. An integrated crop-geotechnical model is introduced in this thesis to overcome one of the limitation of the existing numerical models to simulate vegetated dikes, since most of the numerical models for slope stability do not tackle the impact of vegetation in their boundary conditions analysis. Then this integrated crop-geotechnical model is adopted to consider the effect of cracking of the upper soil layer in dikes. Furthermore, a data driven approach is used to investigate the potential use of Machine Learning (ML) in dike assessment having the remotely sensed data which provides frequent monitoring over larger scale.

In this chapter the conclusion are discussed for each research question that mentioned in Chapter 1 forms each chapter of this thesis.

### **Research question 1: How the climate and vegetation condition affect a regional dike temporal (in)stability?**

The integrated model framework composed of a crop model (LINGRA) and a geotechnical model (PLAXIS 2D) was used to demonstrate the sensitivity of the factor of safety to root zone soil moisture and vegetation condition in an idealised regional dike. It is demonstrated that Soil-Vegetation-Atmosphere (SVA) interaction influences the macro stability of a slope by altering the water balance in the root zone. It is showed that the condition of vegetation (grass in our study) governs dike's hygroscopic condition and therefore controls the temporal dike stability. Lower *LAI* within the same time with the same weather condition leads to the lower FoS for the example dike. Safety of the example dike is mainly dependent on the water content in both the root zone and the dike body, which is affected by the vegetation. It is also mentioned that the precipitation history and water content memory have an impact on both the FoS and the vegetation. Therefore, in Chapter 2 it is proposed that vegetation and root zone water content could be used as proxies to detect vulnerable dikes at an early stage.

### **Research question 2: What is the effect of shrinkage behaviour on the temporal stability of a dike?**

Cracking causes preferential flows from the soil surface into the dike body which cause a quick transfer of precipitation in to the dike body.

In Chapter 3 the integrated model was modified to account for the formation of cracks. The simulation of Chapter 2 is then extended to consider the impact of cracking. Considering the preferential flow into the dike that cause by cracks in the root zone, enables the numerical model to simulate drought in dikes, for instance during the drought in the summer of 2018. This represents a further step towards reality of dike safety calculations, including conditions that the typically modelling approaches ignore. To the author's knowledge so far, neither comprehensive field or laboratory data are available to validate this numerical research and it is suggested to be undertaken in future studies.

It is shown that due to cracking, vegetation dries out in the summer and lower *LAI* is

expected over the cracked area rather than a non-cracked area of a dike. The history of the precipitation, root zone water content and *LAI* have an impact on crack propagation. Therefore, vegetation condition can be used in remote monitoring of dikes to estimate cracked area in larger scale instead of walking along dikes for visually inspection. The results of Chapter 3 suggest that monitoring in the spring or autumn may provide the most reliable and useful results.

**Research question 3: Can data-driven models facilitate the expensive numerical simulations to estimate real-time or short-term prediction of (in)stability?**

Numerical analysis are expensive and time consuming for large scale assessments. In Chapter 4 a supervised ML model is used for the proof-of-concept study to investigate the potential use of RS data in estimating temporal changes in a dike's stability under the impact of climate, vegetation and cracking. This approach can enable experts to assess a significant length of dikes relatively easily and quickly by benefiting from real-time monitoring. A random forest ML approach was adopted, with features that can be measured by satellite remote sensing and do not require visual inspection and in-situ instruments, i.e. *LAI*, surface displacement, cumulative rainfall and temperature.

Based on the results of the predictive model for real-time monitoring and short-term prediction (5 and 15 days before the safety assessed), surface displacement has the highest impact on FoS of the example dike. Including crack area as a feature, improves the model performance in predicting stability of the dike; however, this parameter is not easy to observe. However in the Netherlands, for example, Waterboard Delfland provides a database of cracks observations in the dry seasons (Chotkan, 2021). Having drought induced cracks included in the model will boost the predictive performance to estimate a dike's stability.

**Research question 4: How can Earth observation be deployed as a monitoring tool for the assessment of dikes?** In Chapter 5 the application of dikes monitoring is discussed considering a regional dike near Delft. Free (open source) satellite data is used to monitor vegetation cover and settlements of the example dike for a period of almost 4 years (2015-2020). Vegetation is monitored using two different vegetation indices *LAI* and *NDVI*. The seasonal trend can be easily seen in the results of this optical sensing; however, for cloudy days results cannot be retrieved as optical RS is used. This limitation can be overcome using other methods, for example flying drones over a dike to monitor VIs or using satellite radar. The former option is practical for small scale monitoring, i.e. over tens of km of dikes; while the latter option can provide large scale geospatial data, i.e. hundreds of km of dikes. In Tables 5.1 and 5.2 a compilation of satellite images that are available publicly for users in the Netherlands is provided.

Remote sensing data, in particular from satellite imaging, is ready to be used for continuous dikes monitoring, for instance using InSAR technology surface displacements can be monitored every few days with mm-level precision in all weather conditions, day and night. Having the historical deformation data (from 1992 to today), can be helpful to study trends in dikes behaviour and get a deeper insight into failure mechanisms. Vegetation cover layer on a dike's surface also can be monitored frequently to detect vulnerable areas along a dikes. It has been shown in this study that lower *LAI* or *NDVI* in the growing

seasons can be due to the crack presence which affect the stability. Moreover, in data driven analysis the importance of vegetation and displacement monitoring is investigated to have a real-time estimate of a dike condition. Currently, satellite monitoring has moved towards becoming an operational slope monitoring system, with increased efficiency and quality, in terms of spatial and temporal resolution.

## 6.2. CONTRIBUTIONS

The main contributions of this research are outlined as follows.

- A numerical workflow is developed to include the effect of vegetation on the safety analysis of dikes. A 1D crop model called LINGRA is integrated (one way coupled) to a 2D FEM model, called PLAXIS2D, using Python (Chapter 2).
- The integrated crop-geotechnical model is adopted to tackle drought conditions when evaporation induced cracks generated on the soil surface to the root zone depth. The new approach enables more realistic simulation for slope analysis (Chapter 3).
- Analysing the dike example for a 10 years period, using the real, dynamic climate data, shows that dike stability responds to effective precipitation as well as vegetation condition. The results showed that a lower *LAI* over a dike causes lower stability under the same weather condition. Having VIs, make dike managers aware of vulnerable areas, so that they can take appropriate action (Chapter 3).
- From the same results, it has been shown that vegetation (grass in our case) dies over cracked areas, while over the non-cracked areas the vegetation are healthy. This helps dike managers to identify potentially cracked areas. Since, measuring soil moisture with fine resolution and observing cracks are not practical, VIs can be used as indicators to find such areas (Chapter 3). [Hanssen \(2001\)](#) and [Chotkan \(2021\)](#) suggest that during winter and spring time the vegetation over cracks are stressed compared to vegetation over non-cracked area.
- A data-driven model is developed to estimate a dike (in)stability using remotely observable data. The built Random Forest model was trained and then tested over the synthetic data generated from the numerical model. Machine Learning is introduced as a tool for real-time or short-term prediction of the dike condition, which can avoid repeating numerical simulation for the same dike (Chapter 4).
- Displacement has been shown to have a major impact on the estimation of the condition of a dike. It is therefore advised to monitor surface displacement frequently, which can provide a promising tool as an early warning system (Chapter 4).
- It is shown that the history of precipitation and soil moisture memory affect the performance of the ML model. To investigate the condition of a dike at a certain day, it is always important to consider the history of events before the 'event' day. For example for the dike in our simulation, cumulative precipitation 65 days before the day that safety is estimated to have the most influence on the built ML model.

The lag correlation needs to be considered in analysis of the relation between parameters (Chapters 2, 4).

- It is proposed to improve the current dike visual inspection in the Netherlands, by using satellite RS, that provides high spatial and temporal resolution data. The practice is shown as a proof of concept on a dike example, where the combination of ML and RS method could enable experts to have an early stage warning system of a dike's condition (Chapter 5).

### 6.3. RECOMMENDATIONS FOR FUTURE STUDIES

To further improved the concepts developed in this work, and move towards implementation in practice further research is needed, including the following.

- **Validation of the modelling methods and results:** The following aspects could be investigated: (i) cracking of a vegetated embankment surface, (ii) the consequential additional inflow, (iii) impact on the bulk shear strength, and (iv) the overall influence on the stability. A number of these aspects are scale dependent and are therefore difficult to observe in laboratory experiments; for example, the cracking is influenced by the vegetation rooting depth, the soil grain size and the root zone properties, which themselves are governed by the atmospheric conditions. The bulk reduction in shear strength properties, while convenient for numerical analysis, is difficult to validate as it relies on knowing the failure surface size, orientation and interaction with individual cracks. The influence on the overall stability of cracks could be validated via either scale model tests in the laboratory, or via full scale failure tests (e.g. [de Gast, 2020](#)). The qualitative behaviour is well supported by, albeit limited, literature. One important field test was the BIONICS research embankment ([Hughes et al., 2009](#)) which provided a full scale test where the hydro-mechanical behaviour was monitored, although it was not brought to failure. The additional inflow into cracked vegetated embankments by the use of Electrical Resistivity Tomography was investigated by [Stirling et al. \(2018\)](#), and for the same embankment fractures were shown to be limited approximately to <400 mm ([Eminue, 2018](#)), almost the same depth as the root zone ([Stirling et al., 2018](#)). It is clear that further experimental validation is needed.
- **Implement the integrated numerical workflow for more cases:** Flood defense in the Netherlands are mainly constructed from peat and clay. This research focused on one example dike as a proof of concept for introducing a numerical approach that is able to simulate the effect of vegetation as well as atmospheric interaction. Therefore, it is advised to expand this numerical approach for various dikes with other materials and geometries. In the current study, cracks are considered not to close in wet periods and extend in the next drier condition, in order to tackle the worst case scenario. Further investigation is needed to establish whether this assumption is valid. Besides, cracks considered to only grow vertically, 3D simulation of cracking is advised for future studies. Moreover, current study focused on macro-stability analysis, it is suggested to study the impact of vegetation condition on other failure mode, e.g. overtopping.



- **Automate dike condition assessment:** A single example dike was used as a case study to demonstrate the potential value of machine learning in general to circumvent the computational burden of modeling and taking an important first step towards large-scale monitoring of dike stability with RS data. It is suggested for future studies to include various real case studies to investigate the effectiveness of different ML algorithms for assessing a slope condition. The current research focuses on the using satellite remote sensing for monitoring dikes; however, other available options can provide dike inspectors a finer spatial resolution. Drones can overcome the limitation of optical RS in cloudy days for vegetation monitoring. Radar images can be obtained by putting a radar antenna on the airborne equipment (e.g. airplane) to capture the radar images that can be processed for settlements measurements. Currently there are airborne data collection in the Netherlands for digital elevation measurements, called AHN (Actueel Hoogtebestand Nederland) (AHN, 2020), and these flights could be used to measure more dike settlements more frequently.

As mentioned in Chapter 5, InSAR cannot measure deformation over the grass covered regional dikes, since growing vegetation and mowing hampered having the persistence points over time. It is suggested for future studies on the stability and deformation monitoring of the regional dikes, artificial ground control points, e.g. corner reflectors, are installed (temporally or permanently) over the dike (Yang *et al.*, 2019), then coherent measurements can be derived for a point (where the corner reflector is) on the dike.

## REFERENCES

- AHN (2020). Het actueel hoogtebestand Nederland (AHN). URL <https://www.ahn.nl/>.
- Chotkan, S. A. (2021). *Predicting drought-induced cracks in dikes with artificial intelligence*. Master's thesis, Delft University of Technology.
- de Gast, T. (2020). *Dykes and embankments: A geostatistical analysis of soft terrain*. Ph.D. thesis, Delft University of Technology, the Netherlands, doi:10.4233/uuid:4ce3b4ec-0a6a-4886-9a82-5945a1f9ea50.
- Eminue, O. O. (2018). *Environmental and material controls on desiccation cracking in engineered clay embankments*. Ph.D. thesis, Newcastle University, UK.
- Hanssen, R. F. (2001). *Radar interferometry: data interpretation and error analysis*, vol. 2. Springer Science & Business Media, doi:10.1007/0-306-47633-9.
- Hughes, P. N., Glendinning, S., Mendes, J., Parkin, G., Toll, D. G., Gallipoli, D. & Miller, P. E. (2009). Full-scale testing to assess climate effects on embankments. *Proceedings of the Institution of Civil Engineers - Engineering Sustainability* **162**, No. 2, 67–79, doi: 10.1680/ensu.2009.162.2.67.
- Stirling, R., Glendinning, S., Davie, C., Hen-Jones, R. & Hughes, P. (2018). The behaviour and influence of desiccation cracking on a full-scale, vegetated infrastructure embankment. In *7th International Conference on Unsaturated Soils (UNSAT2018)*, pp. 1–6.
- Yang, M., López-Dekker, P., Dheenathayalan, P., Liao, M. & Hanssen, R. F. (2019). On the value of corner reflectors and surface models in InSAR precise point positioning. *ISPRS Journal of Photogrammetry and Remote Sensing* **158**, 113–122, doi:10.1016/j.isprsjprs.2019.10.006.



# ACKNOWLEDGEMENTS

I would like to thank my promoters, Dr. Phil Vardon and Prof. dr. Susan C. Steele-Dunne, for constant encouragement, generous support, insightful critique, sound advice, swift and thorough revisions, and illuminating discussion through past years. Their expertise, patience, generosity, support, and encouragement were instrumental, not only in helping me to refine my ideas, but also in making this learning process enjoyable and ultimately leads this project to completion.

I also would like to thank Dr. Vahid Galavi from Deltares and Dr. Brinkgreve from TU Delft who invested considerable time and provided invaluable help in the early stages of this project with understanding PLAXIS software. I would like to extend my heartfelt acknowledgements and deepest gratitude to Dr. Faraz S. Tehrani for his valuable advice in Machine Learning analysis. I would like to express my appreciation to Dr. Amin Askarinejad for his great intellectual discussions and motivations about my project, his office door was always open to me.

I would also like to thank the members of my dissertation committee, Prof. dr. M.A. Hicks, Prof. dr. S.N. Jonkman, Dr. J.P. Aguilar Lopez, Ir. H. van Hemert and Dr. K. Tsiamposi for their acceptance to serve in my thesis committee and for the insightful comments, suggestions, encouragement, guidance and feedback on my research.

A special thanks to my present and past colleagues at Geo Engineering section, Arash, Ali, Divya, Zheng, Yuen, Ivo, Weiyuan, Kevin, Hilmi, Stefano, Bram, Tom, Marco, Leon, Luke, Guido and Florian, who made the lunch and coffee time more enjoyable with open, free discussion on various topics. I want to thank my friends Bahare, Aydin, Sara, Faraz, Mahyar, Golshan, Hadi, Anna, Amin, Hoda, Bijan, Sepideh, Saeed, Mahkameh, Vahid, Masoud, Leila, Amin, Ali and Javad for friendship and support that make my life easier and happier in the Netherlands.

Last but not the least; I would like to give my heartfelt appreciation to my parents, Zohreh and Ali, to the love of my life and my best friend, Mehrdad, for always being with me and constantly supporting me in bright and gloomy days.

Elahe Jamalnia  
Delft, June 2021



# CURRICULUM VITÆ

## Elahe JAMALINIA

12-11-1988 Born in Shiraz, Iran

### EDUCATION

- 2006–2011 B.Sc. in Civil Engineering  
Faculty of Civil Engineering  
University of Isfahan, Isfahan, Iran
- 2012–2015 M.Sc. in Civil-Environmental Engineering  
Faculty of Civil Engineering  
University of Tehran, Tehran, Iran
- 2016–2021 Ph.D. in Geo Engineering  
Faculty of Civil Engineering and Geoscience  
Delft University of Technology, Delft, the Netherlands

### WORK

- 2021–current Earth Observation Scientist  
SRON Netherlands Institute for Space Research, Leiden, the Netherlands
- 2020–2021 Geotechnical (Python) Developer  
Waternet, Amsterdam, the Netherlands
- 2015–2016 Junior advisor  
Port and Maritime Organization (PMO) of Iran, Tehran, Iran

### PERSONAL PAGES





# LIST OF PUBLICATIONS

## JOURNAL ARTICLES

6. **E. Jamalnia**, F.S. Tehrani, S.C. Steele-Dunne, P.J. Vardon, *A Data-Driven Surrogate Approach for the Temporal Stability Forecasting of Vegetation Covered Dikes*, *Water* **13**(1), 107 (2021).
5. **E. Jamalnia**, P.J. Vardon, S.C. Steele-Dunne, *The impact of evaporation induced cracks and precipitation on temporal slope stability*, *Computers and Geotechnics* **122**, 103506 (2020).
4. **E. Jamalnia**, P.J. Vardon, S.C. Steele-Dunne, *The effect of soil–vegetation–atmosphere interaction on slope stability: a numerical study*, *Environmental Geotechnics Ahead of print* (2019).

## CONFERENCE PROCEEDINGS

3. **E. Jamalnia**, F.S. Tehrani, S.C. Steele-Dunne, P.J. Vardon, *Predicting Rainfall Induced Slope Stability Using Random Forest Regression and Synthetic Data*, In Proceedings of Understanding and Reducing Landslide Disaster Risk: 5th Land Slide Forum, Nov 2020, Tokyo, Japan, **17**, 132 (2020).
2. **E. Jamalnia**, P.J. Vardon, S.C. Steele-Dunne, *Use of displacement as a proxy for dike safety*, In Proceedings of the International Association of Hydrological Sciences: 10th International Symposium on Land Subsidence (TISOLS), Apr 2020, Delft, The Netherlands, **382**, (2020).
1. **E. Jamalnia**, P.J. Vardon, S.C. Steele-Dunne, *Can vegetation indices predict slope (stability) conditions?*, In Proceedings of Geophysical Research Abstracts: European Geoscience Union (EGU), Apr 2019, Wien, Austria, **21**, (2019).